

UNIVERSITY OF HELSINKI  
&  
UNIVERSITY OF GRONINGEN

MASTER'S THESIS IN EXPERIMENTAL PHYSICS

---

**The use of optical cavities in  
cold molecule trapping,  
laser cooling and  
acetylene spectroscopy**

---

*Author:*  
Janko NAUTA

*Supervisors:*  
Dr. Markus METSÄLÄ  
Dr. Steven HOEKSTRA

*2nd reader:*  
Dr. ir. Hans BEIJERS

December 4, 2014



## Abstract

The use of optical cavities as an experimental tool is investigated in three different projects within the field of molecular physics.

Acetylene is a widely studied molecule to learn about molecular structure, dynamics and interactions. In the physical chemistry group in Helsinki, measurements of higher overtones are carried out to reach a previously unexplored part of the acetylene spectrum. In the first part of this thesis, a new double photon excitation method was implemented by first pumping the molecules to a metastable vibrational stretching state and subsequently performing cavity ring-down spectroscopy. The new method was proven to work and the overtone transition  $0010^00 \rightarrow 2010^00$  was measured at  $6392.403 \pm 0.003 \text{ cm}^{-1}$ .

The cold molecules group in Groningen aims to measure parity violation by using ultra-cold molecules as a sensitive probe. In the second part of this thesis, a new dipole trap for SrF molecules is investigated, in which parity violation measurements can be performed. Trap parameters were calculated: an enhancement cavity can provide 4 kW total trapping power at 1064 nm, leading to an optical lattice with a 200  $\mu\text{m}$  waist and a depth of 4 mK for SrF. An experimental design was made based on two separated beams, one for stabilizing the cavity using a PDH lock and the other creating the lattice, while intensity stabilized by an AOM feedback loop. In a literature study methods for improved loading of the dipole trap were investigated, leading to a new single photon transition scheme in which molecules accumulate in dipole trapped high field seeking states. The first part of the designed setup was built and the enhancement cavity, with a measured FSR of 1300 and incoupling efficiency of 80%, was successfully stabilized by a PDH lock.

A transfer cavity lock and control system was built to lock a cooling laser for SrF to a HeNe laser. The long term stability of the lock was measured to be 2.9 MHz/30 min for a 663.3 nm diode laser.

# Contents

<b>1</b>	<b>Introduction</b>	<b>3</b>
1.1	Acetylene spectroscopy . . . . .	3
1.2	Dipole trapping of cold molecules . . . . .	4
1.3	Transfer cavity lock . . . . .	5
1.4	Thesis outline . . . . .	7
<b>2</b>	<b>Theory</b>	<b>8</b>
2.1	A short history of molecules . . . . .	8
2.2	Molecules . . . . .	9
2.2.1	Rotation . . . . .	11
2.2.2	Vibration . . . . .	12
2.2.3	Optical transitions . . . . .	15
2.3	Optical resonators . . . . .	16
2.3.1	Fabry-Perot resonator . . . . .	16
2.3.2	Losses . . . . .	17
2.3.3	Stability . . . . .	19
2.3.4	Gaussian beams . . . . .	20
2.3.5	Mode matching . . . . .	22
2.3.6	Power enhancement . . . . .	24
2.4	Optical dipole trap . . . . .	25
2.4.1	Dipole force . . . . .	25
2.4.2	Stark Shift . . . . .	25
2.4.3	Optical lattice . . . . .	26
2.5	Cavity ring-down spectroscopy . . . . .	27
<b>3</b>	<b>Acetylene spectroscopy</b>	<b>30</b>
3.1	Experimental overview . . . . .	30
3.1.1	The laser system . . . . .	30
3.1.2	The sample cell . . . . .	32
3.1.3	Data acquisition . . . . .	33
3.1.4	ECDL setup . . . . .	33
3.2	Performing the experiments . . . . .	34
3.2.1	Measurements on heavy water . . . . .	35
3.2.2	Measurements on acetylene . . . . .	37
3.3	Results . . . . .	38
3.4	Conclusion . . . . .	44

<b>4</b>	<b>Dipole trapping of cold molecules</b>	<b>45</b>
4.1	Trap requirements . . . . .	46
4.2	Design of an optical dipole trap . . . . .	47
4.2.1	Enhancement cavity design . . . . .	49
4.2.2	Laser requirements . . . . .	50
4.3	Experimental setup . . . . .	51
4.3.1	Trapping region . . . . .	51
4.3.2	Dipole trap stability . . . . .	51
4.3.3	Pound-Drever-Hall lock . . . . .	53
4.3.4	Intensity stabilization . . . . .	54
4.3.5	Separating the beams . . . . .	54
4.3.6	Vacuum feed-through . . . . .	54
4.4	Improving dipole trap loading . . . . .	55
4.4.1	Gray molasses . . . . .	55
4.4.2	RF-knife . . . . .	57
4.4.3	Optical one-way barrier . . . . .	58
4.4.4	Continuous loading . . . . .	58
4.4.5	Loading with optical molasses . . . . .	59
4.4.6	Single photon transition scheme . . . . .	59
4.5	Test setup . . . . .	66
4.6	Conclusion . . . . .	71
<b>5</b>	<b>Transfer cavity lock</b>	<b>73</b>
5.1	Locking objectives . . . . .	73
5.2	Experimental setup . . . . .	74
5.2.1	Reference laser . . . . .	74
5.2.2	Transfer cavity . . . . .	75
5.2.3	Feedback system . . . . .	76
5.2.4	Laser controller . . . . .	77
5.3	Results . . . . .	78
5.4	Conclusion . . . . .	82
<b>6</b>	<b>Outlook</b>	<b>83</b>
<b>7</b>	<b>Acknowledgements</b>	<b>85</b>
	<b>Appendices</b>	<b>91</b>
<b>A</b>	<b>Details of the acetylene experimental setup</b>	<b>92</b>
<b>B</b>	<b>Additional data on acetylene</b>	<b>93</b>
<b>C</b>	<b>Details of the transfer cavity lock</b>	<b>96</b>
C.1	Gain of laser feedback signal . . . . .	96

# Chapter 1

## Introduction

The study of molecules has been an active field of research since their discovery roughly two centuries ago. Their complex structure and dynamics as well as their large variety of interactions with each other and with electromagnetic radiation have intrigued many generations of scientists. Given that these interactions occur between their constituent parts, atoms, and therefore also between fundamental particles as electrons, molecules can be used as a probe to physics at a fundamental level. Nowadays numerous techniques with ever increasing precision are available to carry out experiments on molecules. Most of these rely on the interaction of molecules with monochromatic coherent electromagnetic radiation, originating from a laser. The production, manipulation and detection of laser light has therefore become a very important part in the field of molecular physics. In this thesis, the use of an experimental tool for manipulation of laser light, the optical cavity, is investigated in three different projects within the field of molecular physics. First, a cavity is used to increase the measurement precision in molecular spectroscopy. This project was done at the University of Helsinki. Second a cavity is employed for trapping of molecular cloud in the cold molecule regime, and third, a cavity is used to stabilize a cooling laser for laser cooling of molecules. Both these projects were carried out at the University of Groningen.

### 1.1 Acetylene spectroscopy

Molecular spectroscopy is a widely used method to learn about the internal structure of molecules. Electromagnetic radiation is used to probe transitions between energy levels of the molecule. The data is then compared to a theoretical model and when combined they improve our understanding of the molecular structure, dynamics and interactions. In this part of the thesis I will report on the experimental work I did under supervision of Markus Metsälä in the field of gas-phase molecular spectroscopy in the Physical Chemistry group of prof. Halonen at the University of Helsinki. The group carries out both computational work on the internal structure of molecules as well as experimental work where cavity ring-down spectroscopy is used as a measurement tool for human breath analysis.

Acetylene,  $C_2H_2$ , is a linear molecule with a simple structure consisting of

just three bonds. Its optical spectra are however far more complicated and this is one of the reasons why the molecule has been studied extensively<sup>1;2</sup>. The studies have focussed mainly on the rotational-vibrational spectrum of acetylene, ranging from the far infrared to the ultraviolet and have led to a better understanding of intramolecular processes. However, there are still unsolved problems in modelling the internal dynamics of the molecule. One of them is about the symmetric vibrational states of acetylene with respect to the hydrogen nuclei permutation in the ground electronic state<sup>3</sup>. In traditional spectroscopy experiments these vibrational overtones cannot be measured because for one photon the transition from the symmetric ground state is forbidden. To be able to reach these states, Raman scattering could be used<sup>4</sup>, or one could start from asymmetric ground states populated by tails of the Boltzmann distribution. However, in both methods the overtone transitions will be very weak and extremely sensitive experimental techniques are required to measure them<sup>5</sup>. Other, more involved techniques, include stimulated emission probing (SEP)<sup>6</sup> where an electronically excited state is used as intermediate level, or laser-induced dispersive vibration-rotation fluorescence (LIF)<sup>7</sup>, where infrared vibrational emission transitions from a higher overtone, populated by a pump beam, are observed.

In the first part of this thesis, a new method of two photon excitation was used to reach the higher vibrational overtones of acetylene. First a CW pump beam from a mid-infrared parametrical oscillator brings the molecules from the symmetric vibrational ground state to a metastable anti-symmetric stretching vibrational state. Then the molecules are excited several vibrational quanta up by a CW probe beam in the visible or near infrared regime. The higher overtones are investigated using cavity ring-down spectroscopy (CRDS), offering the advantage of a high signal to noise ratio. Furthermore, the technique is Doppler-free because of the double excitation by the two parallel laser beams.

## 1.2 Dipole trapping of cold molecules

In fundamental particle physics, the Standard Model is a theory that can describe almost all measurements ever done in this field. The Standard Model contains three symmetries: Charge conjugation (C), Parity reversal (P) and Time reversal (T). It is known that for the weak nuclear force parity symmetry is broken. This is called parity violation, and has already been measured in atoms<sup>8</sup>. However, in diatomic molecules the effects of parity violation are enhanced by the ratio their constituent nuclear masses, which makes them a much more sensitive probe for parity violation than atoms. To carry out high precision measurements one needs the particle to be as cold as possible, allowing for a longer coherent interaction time during a measurement. For atoms the preparation of ultra-cold samples is nowadays easily achieved using standard cooling techniques as laser cooling, magneto-optical trapping and evaporative cooling. Due to their complex internal structure, the cooling and trapping of molecules has succeeded only in very few experiments so far, and performing high precision measurements on molecules is therefore much more challenging.

In the Fundamental Interactions and Symmetries division at the University of Groningen, the cold molecules group is working on an experimental setup to measure parity violation in Strontiummonofluoride (SrF). Its favourable branch-

ing ratios make this molecule, as one of the very few, suitable for laser cooling<sup>9</sup>. Furthermore, the large electric dipole moment of SrF causes a Stark shift which can be utilized for Stark deceleration<sup>10</sup>. Finally, the large mass of the Strontium atom makes the molecule a sensitive probe for parity violation. Combining these three advantages of SrF, the aim of the cold molecule group is to first decelerate, then cool and trap, and ultimately measure these molecules.

In Figure 1.1 the consecutive stages of the experiment are depicted. SrF molecules are produced by ablation from a pill with a pulsed Nd:YAG-laser. An adiabatically expanding Xenon gas pulse cools the initially hot molecules down to a few Kelvin and takes them to the beginning of a 4.5m long decelerator. The decelerator consists of a few thousand ring-shaped electrodes in a row, onto which a periodically changing high voltage is applied. Due to the Stark shift of SrF some states, the low field seeking states (lfs), are attracted to the electric field minima on the axis of the decelerator. By applying an AC voltage to the electrodes, the moving speed of the electric traps can be adjusted to the velocity of the molecules entering the decelerator. The frequency is then swept down to DC over the length of the decelerator, slowing down the speed of the electric traps and thus also slowing down the molecules. At the end of the decelerator the molecules are confined in a static electric trap. Here optical molasses further reduce the internal temperature of SrF by laser cooling. Once cold enough, the molecules are loaded into an optical dipole trap for tighter confinement and longer storage times on the order of 1 second. In this trap the final high precision measurements on the ultra-cold molecules can be carried out.

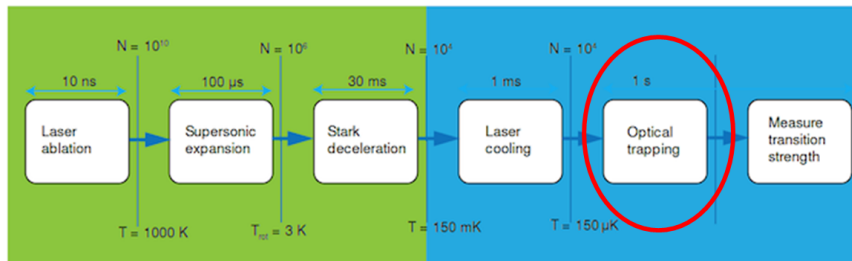


**Figure 1.1:** Overview of the consecutive stages of the experimental setup for cooling and trapping SrF molecules.

Recently, the first two meter of the decelerator has shown promising deceleration results<sup>11</sup>, and currently four meters of the decelerator are operational. The design of the laser cooling and trapping region has been made by Corine Meinema and is ready to be implemented at the end of the decelerator. The second part of this thesis reports on the design and first tests of the next experimental stage: the optical dipole trap.

### 1.3 Transfer cavity lock

As was mentioned in the previous section, one of the reasons to choose SrF as a probe molecule to measure parity violation in the cold molecule experiment is the favourable branching ratios in the molecule. Because molecules

possess many rovibrational states, usually an electronically excited state can decay into many different ground states, each with different rotational and vibrational quantum numbers. However for SrF, there are a few specific excited states which almost always decay back in the same rovibrational states within the electronic ground state. These are shown in Figure 1.2, where  $v$  and  $N$  represent the vibrational and rotational quantum number, respectively. The existence of an (almost) closed transition cycle is a crucial requirement for applying laser cooling, since this process relies on scattering many photons on the same molecule, each transferring a small momentum 'kick' to the molecule in the opposite direction of the molecular velocity, therefore lowering its kinetic energy and thus reducing the temperature. From the figure we see that when using the  $X^2\Sigma^+(v=0, N=1) \rightarrow A^2\Pi_{1/2}(v'=0, j=1/2)$  transition at 663.3 nm, 98 % of the molecules can be excited again by the same laser and only 2 % decays back into a  $v=1$  electronic ground state. When an extra repump laser at 686.0 nm is included, the losses to dark states are limited to  $\sim 10^{-4}$ , which is good enough for our experiment<sup>12</sup>.

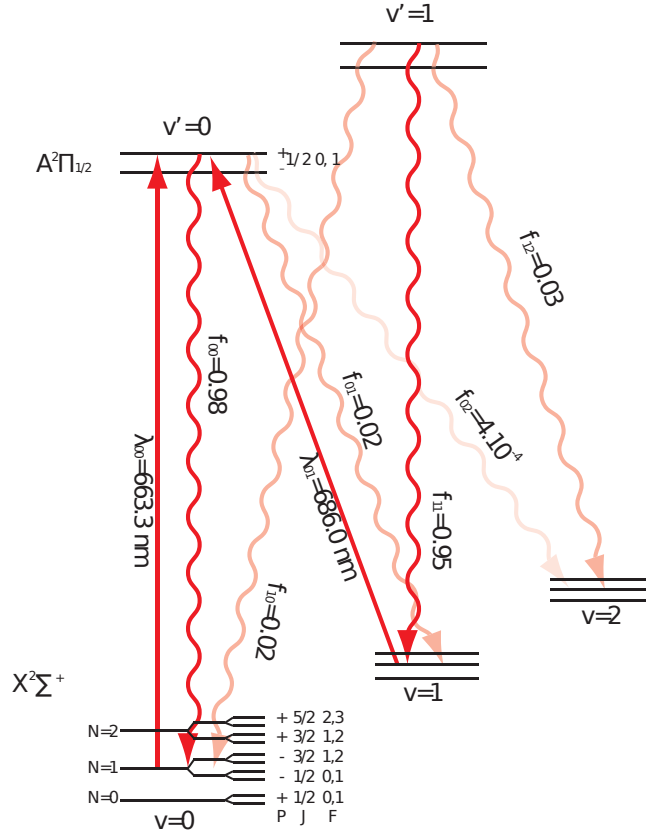


**Figure 1.2:** Schematic energy level diagram of states of SrF suitable for lasercooling. The straight lines indicate resonant laser excitation frequencies, while the wiggling lines represent possible decays back to the ground state, with the associated Franck-Condon factors (decay probabilities to the different vibrational states) given. (Figure from ref. 13)

The laser light for cooling the molecules is generated by homebuilt external cavity diode lasers (ECDL), which are tunable over a few tens of nanometers. To keep the laser at the right frequency, an I<sub>2</sub> vapour cell is used as a reference and using a Doppler-free saturation absorption spectroscopy setup the 663.3 nm SrF pump laser is locked to the a set of absorption peaks in the Iodine spectrum<sup>14</sup>. The 686.0 laser is already operational but no locking system has been developed for this laser. It would probably be possible to use the same Iodine cell to lock also the 686.0 laser, but since the optical setup would become complicated, and mainly because the Iodine lock is currently facing stability problems it was decided to develop a different locking system for the 686.0 nm laser: a transfer cavity lock. This type of locking uses an optical cavity to transfer the stability of a reference laser to the repump laser. In the third and last part of this thesis, the building and characterization of a transfer cavity lock for the SrF repump laser is described.

## 1.4 Thesis outline

This thesis will start with a theoretical chapter, providing a theoretical basis and explaining the main experimental techniques used in the rest of the thesis. The next three chapters form the main part of the thesis, each describing one of the experiments I did involving optical cavities. In Chapter 3 the acetylene spectroscopy project is introduced, an experimental overview is given and the measurement methods are described. Subsequently, the first measurement results are presented and discussed. Chapter 4 describes the design of an optical dipole trap for cold molecule trapping. First the trapping requirements are introduced, then the characteristics of the trap are explained, leading to a trap design. Next, a literature survey is carried out to investigate the improved loading of the dipole trap, and a new single photon transition system is proposed. The chapter ends with a description and analysis of the realized test setup. In Chapter 5 the implementation of a transfer cavity lock is described and the first stability results are presented and discussed. In the final Chapter 6 a general conclusion is drawn together with an outlook.

# Chapter 2

## Theory

In this chapter the theoretical background for this thesis is described. As molecules are the main system under observation throughout this thesis, the chapter starts with a brief description of main historical breakthroughs in the knowledge about molecules. Subsequently, a quantum-mechanical description of the molecule is given, providing a basic understanding of its electronic, vibrational and rotational energy states and the possibilities to transfer from one state to another. Then the most important properties of optical cavities, the main topic of this thesis, are described. After this general part of theory, more specific topics are discussed, each relevant to one of the three main experimental parts. First the optical dipole trap as an experimental technique to trap particles is addressed, which later on will be used for the trapping of SrF-molecules. Second, the working principle of cavity ring-down spectroscopy is explained, which is used in the experimental part on acetylene.

### 2.1 A short history of molecules

The concept of molecules was established for one of the first times by the British chemist Dalton in 1808<sup>15</sup>. He postulated that all substances consist of atoms and that a compound substance is formed by the combination of one or more atoms of one element with one or more atoms of another element, like in H<sub>2</sub>O, CO<sub>2</sub> etc. Different numbers of atoms can be combined to form different molecules, for instance NO, N<sub>2</sub>O, NO<sub>2</sub> with the atomic ratios N:O, 1:1, 2:1, 1:2, respectively.

In 1811 Avogadro came with the hypothesis that equal volumes of different gases at equal pressure and temperature contain the same number of elementary particles. Avogadro observed that one unit volume of hydrogen combined with one unit volume of chlorine produces two unit volumes of hydrogen chloride and deduced therefrom that elementary particles in chlorine and hydrogen are not atoms but diatomic molecules: H<sub>2</sub> and Cl<sub>2</sub>, so the reaction becomes H<sub>2</sub> + Cl<sub>2</sub> → 2HCl.

In the mid-19th century Clausius came up with the kinetic theory of gases. He found that the volume of all molecules in a gas has to be much smaller than the total volume of the gas at standard temperature and pressure. Evidence for his conclusion was that the density of a gas is about three orders of magnitude smaller than that of condensed matter, and that in a gas the duration of col-

lisions is small compared to the time between collisions, so the molecules can essentially move freely.

Towards the end of the 19th century Boltzmann, Maxwell and Rayleigh showed that the energy of a gas in thermal equilibrium is distributed evenly between all degrees of freedom of the particles, with an energy of  $kT/2$  per degree of freedom per particle. Herefrom it was clear that molecules must have more degrees of freedom than atoms, because molecular gasses possess a larger specific heat than atomic gasses. This idea opened the way for studies of the internal dynamics of molecules.

The technique of molecular spectroscopy originates from the beginning of the 19th century. In 1834 Brewster observed hundreds of absorption lines, extending throughout the complete visible spectrum, by spectral dispersion of sunlight, transmitted through a  $\text{NO}_2$  gas, with the aid of a prism. Brewster was astonished by the number of lines he saw and predicted that a complete explanation of this phenomenon would provide work for many generations of researchers, which turned out to be a correct prediction.

Only after Kirchoff and Bunsen developed the spectral analysis in 1859, the importance of a quantitative interpretation of spectra for the study of chemical compounds was recognized. When Rowland managed to produce optical diffraction gratings with sufficient precision in 1887 individual lines could be resolved with large grating spectrographs. This allowed for the identification of several simple molecules by their spectra.

A better understanding of molecular spectra was achieved after the quantum theory was developed in the 1920s and 1930s, when numerous theoreticians applied the mathematical formulation of the quantum theory by Schrödinger and Heisenberg to provide quantitative explanations of molecular spectra.

The introduction of narrow-band tunable lasers around 1960 opened the way for new techniques with spectral resolutions below the Doppler width of absorption lines.

## 2.2 Molecules

When an atom or molecule absorbs or emits radiation electromagnetic radiation in the form of a photon, the internal state of the particle changes from a state with energy  $E_1$  to a different state with energy  $E_2$ . Conservation of energy requires that

$$h\nu = E_1 - E_2, \quad (2.1)$$

where  $h$  is Planck's constant. In this thesis we are only interested in transitions with involving discrete states with well defined energies, where the transitions take place at a sharply defined frequency  $\nu$ . In a spectrum these transitions show up as lines with wavelengths  $\lambda = c/\nu$ , where  $c$  equals the speed of light, or alternatively wavenumbers can be used  $\bar{\nu} = 1/\lambda$ .

In the case of atoms, the possible energy states are determined by the configuration of the electron cloud, so all spectral lines of an atom correspond to an electronic transition. For molecules the situation is different, they have additional internal degrees of freedom so their spectra are not only determined by the electronic configuration, but also by the arrangement of the nuclei and their relative movements. Therefore, for each electronic state, multiple vibrational states exist due to vibration of the nuclei around their equilibrium position.

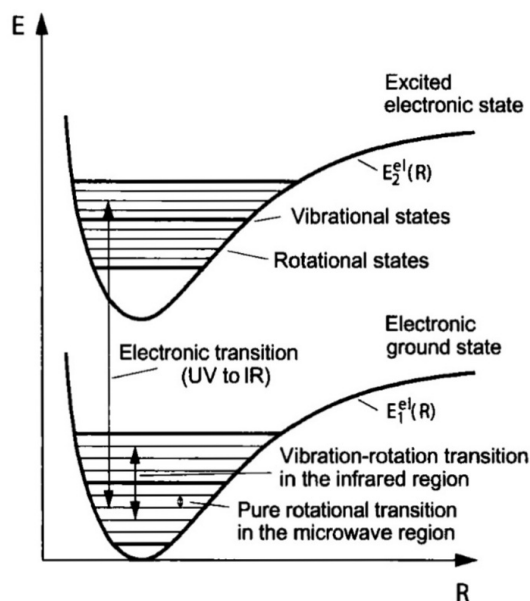


**Figure 2.1:** Schematic representation of the possible transitions in a diatomic molecule. (Figure from ref. 15)

Within these vibrational states a number of rotational states is present, caused by the rotation of the molecule as a whole around axes through its center of mass. For this reason molecular spectra are more complicated than atomic spectra.

The different transitions in a molecule are shown in Figure 2.1 and can be categorized as follows:

- Transitions between rotational levels within the same vibrational and electronic state have typical wavelengths in the microwave region:  $100\mu m \lesssim \lambda \lesssim 1m$
- Transitions between fundamental vibrational levels within the same electronic state have typical wavelengths in the mid-infrared region:  $2\mu m \lesssim \lambda \lesssim 20\mu m$
- Transitions between two different electronic states have wavelengths from the UV to the near infrared:  $0.1\mu m \lesssim \lambda \lesssim 2\mu m$

To calculate the rotational and vibrational molecular energy levels we start with the Schrödinger equation:

$$\hat{H}\Psi = \hat{T} + \hat{V} = -\frac{\hbar^2}{2m}\nabla^2\Psi + V\Psi = E\Psi \quad (2.2)$$

with the Hamiltonian ( $H$ ) consisting of a kinetic energy term  $T$  and a potential energy term  $V$ . The potential energy is due to the Coulomb interaction between mutual nuclei, mutual electrons and electrons and nuclei. The spin interactions between both nuclei and electrons are small compared to the kinetic

and potential energy, so they can be treated as perturbations of the Schrödinger equation.

Because the electron mass is much smaller than the nucleon mass, electrons move much faster than nuclei. Therefore the electrons adapt their configuration almost instantaneously to a change in the position of the nuclei, for instance caused by nuclear vibrations. For this reason one can neglect the coupling between the nuclear motion and electronic distribution. This is known as the Born-Oppenheimer approximation and separates the Schrödinger equation into two decoupled equations:

$$\hat{H}_0 \psi_n^{el} = E_n^0 \psi_n^{el} \quad (2.3)$$

$$(\hat{T}_{nuc} + E_n^0) \psi_{n,v}^{nuc} = E_{n,v} \psi_{n,v}^{nuc} \quad (2.4)$$

With  $E_n^0$  being the total energy of the molecule for electronic configuration  $n$ . For each electronic state  $\psi_n^{el}$ , there are multiple solutions  $\psi_{n,v}^{nuc}$ , describing different vibrational nuclear states labelled with  $v$ . Therefore it is possible to calculate the vibrational, and also rotational, states using a static electronic potential. For a diatomic molecule, we can make a coordinate transformation to the molecule's center-of-mass frame by introducing the reduced nuclear mass  $\mu = \frac{M_1 M_2}{M_1 + M_2}$ , equation (2.4) then becomes

$$\left( \frac{-\hbar^2}{2\mu} \nabla^2 + E_n^0 \right) \psi_{n,v}^{nuc} = E_{n,v} \psi_{n,v}^{nuc} \quad (2.5)$$

Now the potential energy  $E_n^0$  depends only on the inter-nuclear distance and is spherical symmetric. Therefore, in analogy to the hydrogen atom, it can be split into two independent parts: a radial and an angular part. The radial part describes the vibration of the two nuclei, in the direction of the inter-nuclear axis, while the angular part describes the rotation of the molecule around the inter-nuclear axis. Also for molecules consisting of more than two atoms the coupling between rotational and vibrational motion can often be neglected so both motions can be treated separately.

### 2.2.1 Rotation

The most simple model for a rotating molecule is that of a rigid rotor, where the bond lengths of the molecule remain constant. For any rigid body, the three components of the moment of inertia are given by<sup>16</sup>:

$$I_{xx} = \sum_i m_i (y_i^2 + z_i^2) \quad (2.6)$$

$$I_{yy} = \sum_i m_i (z_i^2 + x_i^2) \quad (2.7)$$

$$I_{zz} = \sum_i m_i (x_i^2 + y_i^2) \quad (2.8)$$

$$(2.9)$$

With  $m_i$  the mass of atom  $i$ . When the molecule-fixed reference frame is chosen with its axes pointing along the three principal moments of inertia, the products

of inertia vanish:  $I_{xy} = I_{zy} = I_{zx} = 0$ . Then the rotational energy of the molecule can be expressed as

$$T_{rot} = \frac{1}{2} \left( \frac{J_x^2}{I_{xx}} + \frac{J_y^2}{I_{yy}} + \frac{J_z^2}{I_{zz}} \right) \quad (2.10)$$

with the angular momentum  $J$  and moment of inertia  $I$  in Cartesian components in the molecule-fixed reference frame. The total angular momentum and its quantum mechanical operator are defined as

$$\mathbf{J} = \sum_j \mathbf{r}_j \times \mathbf{p}_j \rightarrow \hat{J} = \sum_j \hat{r}_j \times \frac{\hbar}{i} \nabla_j \quad (2.11)$$

where  $\mathbf{p}$  is the momentum and  $\mathbf{r}$  the position vector. In general, the solution of the Schrödinger equation with the Hamiltonian equal to (2.10) will involve three different quantum numbers, one for each moment of inertia. However, for linear molecules, like acetylene, the moment of inertia along the molecular axis is zero and both other moments are equal.

Using conservation of angular momentum ( $J = J_x^2 + J_y^2 + J_z^2 = \text{const}$ ), the eigenvalues of the molecule energy are calculated to be<sup>17</sup>

$$E(J) = \frac{\hbar^2 J(J+1)}{2I_{\perp}} \quad (2.12)$$

with total angular momentum quantum number  $J$  and  $I_{\perp}$  the moment of inertia perpendicular to the molecular axis. For this model of the molecule as a rigid rotor, we have assumed the bond lengths do not change. However, as discussed earlier, due to nuclear vibrations in reality the bond lengths do change.

A better model for the molecule is therefore that of a non-rigid rotator, where the masses are connected by massless springs instead of a massless rigid bar. In this model, the internuclear distance will increase when the rotation increases due to the centrifugal force. Therefore also the moment of inertia  $I_{\perp}$  increases and (2.12) changes to<sup>18</sup>

$$F(J) = \frac{E}{hc} = BJ(J+1) - DJ^2(J+1)^2 \quad (2.13)$$

where the rotational constants are given by

$$B = \frac{\hbar}{4\pi I_{\perp}} \quad (2.14)$$

$$D = \frac{4B^3}{\omega^2} \quad (2.15)$$

with  $\omega$  the vibrational frequency of the rotating system.

### 2.2.2 Vibration

Vibrations in the inter-nuclear distance can be modelled as a simple harmonic oscillator. For a diatomic molecule the Hamiltonian is then given by

$$H = -\frac{\hbar^2}{2\mu} \frac{\partial^2}{\partial r^2} + \frac{1}{2} kx^2 \quad (2.16)$$

with  $\mu$  the reduced mass of the two nuclei and  $k$  the force constant. The corresponding energy levels are

$$E(v) = \hbar \sqrt{\frac{k}{\mu}} \left( v + \frac{1}{2} \right) = \hbar \omega \left( v + \frac{1}{2} \right) \quad (2.17)$$

with  $v$  the vibrational quantum number. Using the harmonic potential model, transitions with  $\Delta v = \pm 1$  are allowed. For the acetylene however the aim is to measure overtone transitions, with  $\Delta v \geq 2$ . In that case, the vibrational potential energy can no longer be approximated by a harmonic potential because the vibrational potential energy does not go to infinity for large distances, but converges to the dissociation energy of the molecule. This is the bond energy between the two atoms minus the vibrational ground state energy  $E(0) = \frac{1}{2} \hbar \omega$ , as indicated in Figure 2.2.

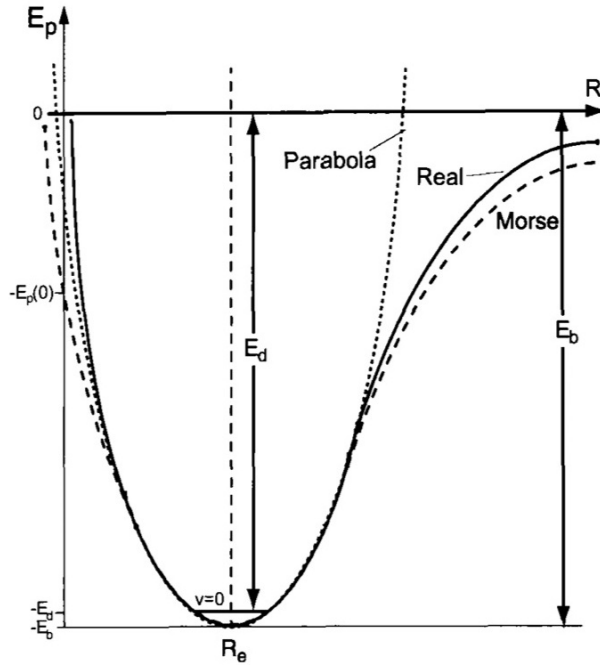


**Figure 2.2:** Vibrational potential energy in a diatomic molecule (solid line) compared to a harmonic potential model (dotted line) and a Morse potential (dashed line). (Figure from ref. 15)

Instead of a harmonic potential, one can use a Morse potential as a better approximation to the real vibrational potential:

$$V_{Morse}(r) = E_b \left[ 1 - e^{-a(r-r_e)} \right]^2, \quad a = \sqrt{\frac{k}{2E_b}} \quad (2.18)$$

With  $E_b$  the depth at  $r = r_a$  and  $a$  describing the steepness of the potential. Inserting the Morse potential in the Schrödinger equation yields the exact solution

for the vibrational levels:

$$G(v) = \omega_e \left( v + \frac{1}{2} \right) - \omega_e x_e \left( v + \frac{1}{2} \right) \quad (2.19)$$

$$\omega_e = \frac{\omega_0}{2\pi c}, \quad \omega_e x_e = \frac{a^2 \hbar}{4\pi c \mu} \quad (2.20)$$

With frequency  $\omega_0 = a\sqrt{2E_b/\mu}$ . The vibrational levels are no longer equally spaced as in the harmonic approximation but the energy spacing decreases linearly with  $v$ . Where diatomic molecules like SrF possess one vibrational mode, polyatomic molecules can have more modes depending on their number of atoms  $N$ . The vibrational potential energy of a polyatomic molecule depends on the coordinates of the nuclei in the molecule-fixed reference frame, and has therefore  $3N$  degrees of freedom. Rotation and translation of the whole system do not change the potential ( $3N - 6$ ), but for a linear molecule there is no rotation around the inter-nuclear axis possible, resulting in a total of  $3N - 5$  vibrational modes.

Acetylene has 5 different normal vibrational modes, as depicted in Figure 2.3. The modes are denoted as  $v_1 v_2 v_3 v_4^{l_4} v_5^{l_5}$  in normal mode notation, with  $l_4$  and  $l_5$  corresponding to the total vibrational angular momentum in the two doubly degenerate  $v_4$  (*cis*-bend) and  $v_5$  (*trans*-bend) mode, respectively<sup>19</sup>.

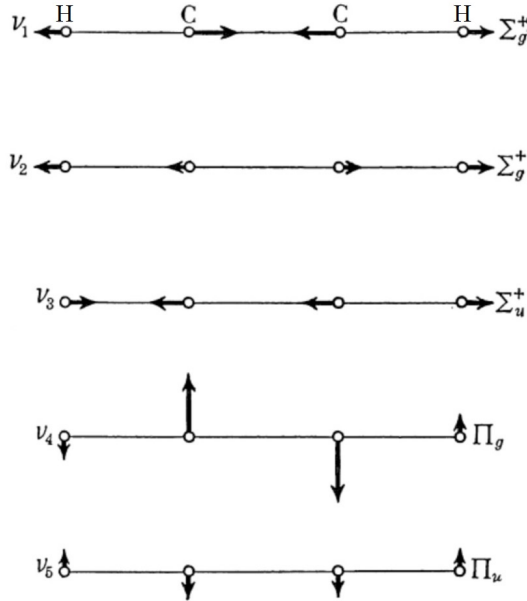


**Figure 2.3:** Normal vibrational modes in acetylene. (Figure from ref. 19)

The water molecule possesses three different modes, denoted as  $(v_1 v_2 v_3)$  in normal mode notation.  $v_1$  represents symmetric stretch and  $v_3$  asymmetric stretch while  $v_2$  refers to the bending fundamental. Another notation describing vibrational levels is the local mode notation, which has shown to be more suitable for describing higher excited vibrational levels<sup>20</sup>. Here vibrational energies are denoted as  $mn^\pm, v_2$ , with  $m$  and  $n$  representing quanta of local stretch in

symmetric, +, or anti-symmetric, -, combinations and  $v_2$  the number of bending quanta. When  $m = n$  the resulting combination is in general symmetric and the + is omitted.

So far the rotational and vibrational degrees of freedom inside the molecule have been treated quite separately. In this case, the total energy of the molecule would simply be given by the sum of vibrational energy levels (2.20) and the rotational energy levels (2.13). However, in reality these motions occur simultaneously and hence during a vibration the inter-nuclear distance changes, as well as the moment of inertia and rotational constant  $B$ . The vibrating rotator model takes these motions into account. Because the period of vibration is very small compared to the period of rotation, a mean  $B$ -value can be used as rotational constant within a single vibrational state<sup>18</sup>:

$$B_e = \frac{\hbar}{4\pi I_{\perp}} \overline{\left(\frac{1}{r^2}\right)} \quad (2.21)$$

With  $\overline{\left(\frac{1}{r^2}\right)}$  being the mean value of  $\frac{1}{r^2}$  during the vibration. To a first approximation, the rotational constant  $B_v$  for vibrational state  $v$  is given by

$$B_v = B_e - \alpha_e \left(v + \frac{1}{2}\right) + \dots \quad (2.22)$$

where  $\alpha$  is small compared to  $B_e$  because the change in inter-nuclear distance is small compared to the inter-nuclear distance itself. Analogous to  $B_v$ , also an averaged rotational constant  $D_v$  is used to include the centrifugal force:

$$D_v = D_e - \beta_e \left(v + \frac{1}{2}\right) + \dots \quad (2.23)$$

Also here  $\beta_e$  is small compared to  $D_e = \frac{4B_e}{\omega_e}$ . Now when including both vibration and rotation and their interaction we obtain for the total energy of the vibrating rotator:

$$T = G(v) + F_v(J) = \omega_e \left(v + \frac{1}{2}\right) - \omega_e x_e \left(v + \frac{1}{2}\right) + \dots + B_v J(J+1) - D_v J^2(J+1)^2 + \dots \quad (2.24)$$

### 2.2.3 Optical transitions

So far only static electronic, rotational and vibrational energy levels of a molecule have been considered. When a molecule interacts with a light field matching the energy difference of two molecular states,  $\Delta E = \hbar\omega$ , transitions between these states can occur. The first-order contribution in the interaction takes place between the electric part of the field and the dipole moment operator of the molecule<sup>17</sup>. The electric field and dipole moment can be written as:

$$\mathbf{E}(\mathbf{r}, t) = \mathbf{E}_0 \cos(\mathbf{k} \cdot \mathbf{r} - \omega t), \quad \boldsymbol{\mu} = \sum_i \mathbf{r}_i q_i \quad (2.25)$$

With  $\mathbf{E}_0$  the electric field vector,  $\mathbf{k}$  the propagation vector and  $\boldsymbol{\mu}$  the electric dipole moment, summing over all charges  $q_i$  at positions  $\mathbf{r}_i$ . The interaction

can be described by adding a time-dependent perturbation into the Schrödinger equation<sup>21</sup>:

$$\hat{H}'(t) = \mathbf{E}(\mathbf{r}, t) \cdot \boldsymbol{\mu}, \quad i\hbar \frac{\partial \Psi}{\partial t} = (\hat{H} + \hat{H}'(t)) \Psi \quad (2.26)$$

Solving the time-dependent Schrödinger equation leads to a transition rate  $R_{01}$  for a light field resonant with a molecular transition from state  $|n\rangle$  to  $|m\rangle$ :

$$R_{nm} = \frac{\pi}{2\hbar^2} E_0^2 \langle m | \boldsymbol{\mu} | n \rangle^2 = \frac{\pi}{2\hbar^2} E_0^2 \mu_{nm}^2 \quad (2.27)$$

Here  $\mu_{nm}$  appears, which is an element of the transition dipole moment matrix, a critical factor in determining if the transition is possible. If non-zero, a relatively strong molecular transition occurs. If  $\mu_{nm}$  is zero, no first-order transitions are possible, but higher order effects could still cause the transition to be observable although weaker by several orders of magnitude.

The intensity of the transitions is related to the matrix elements by the famous Einstein coefficients A, for spontaneous emission, and B, for stimulated absorption and stimulated emission. Neglecting the spontaneous emission rate, the intensity of absorption by an optical field, in  $W/cm^2$ , can be expressed as<sup>18</sup>

$$I_{abs}^{nm} = h\rho N_n B_{nm} v_{nm} \Delta l \quad (2.28)$$

Where  $\rho$  is the density of the optical field with frequency  $v_{nm}$ ,  $N_n$  the number of molecules in the initial (lower) state  $n$  and  $\Delta l$  the length of the sample. The Einstein absorption coefficient  $B_{nm}$  is given by

$$B_{nm} = \frac{8\pi^3}{3h^2c} \mu_{nm}^2. \quad (2.29)$$

## 2.3 Optical resonators

An optical resonator is an optical circuit in which light is confined<sup>22;23;24</sup>. The light circulates at certain resonance frequencies and the resonator can therefore be viewed as an optical feedback circuit. There are many possible configurations for the resonator but in this thesis we focus on the configurations using mirrors as reflectors, as shown in Figure 2.4.

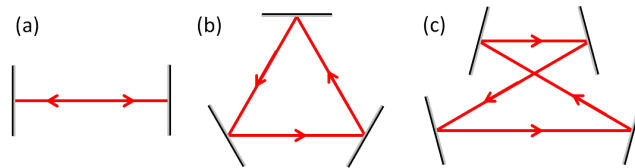


**Figure 2.4:** Three common-used configurations for an optical cavity: (a) Fabry-Perot, (b) ring, (c) bow-tie.

### 2.3.1 Fabry-Perot resonator

First we consider the simplest Fabry-Perot configuration, consisting of just two planar mirrors placed exactly opposite to each other, separated by distance  $d$ . A

monochromatic light wave with angular frequency  $\omega$  can be represented by the wave function

$$E(\mathbf{r}, t) = E(\mathbf{r}) \exp(i\omega t) \quad (2.30)$$

where  $E(\mathbf{r})$  represents the real part of the complex amplitude  $\tilde{E}$ , which satisfies the Helmholtz equation<sup>23</sup>. Solving the Helmholtz equation and imposing that the transverse components of the electric field vanish at the surface of both mirrors results in a set of standing waves inside the resonator:

$$E(\mathbf{r}) = A_q \sin(k_q z) \quad (2.31)$$

With  $A$  being a constant and  $k = \omega/c$  the wavenumber. The different values for  $k$  originate from the fact that only an integer number  $q$  of half-wavelengths can fit exactly inside the resonator. This is illustrated in Figure 2.5. The associated frequencies are therefore also restricted to discrete values and related to the mode number by

$$v_q = q \frac{c}{2d}. \quad (2.32)$$

These are the resonance frequencies of the cavity. The distance between two adjacent cavity modes is called the Free Spectral Range (FSR) of the resonator and is given by:

$$v_{FSR} = \frac{c}{2d}. \quad (2.33)$$

It is clear that for a longer cavity the mode spacing decreases so the resonance frequencies will be closer to each other. When changing the cavity length by exactly half a wavelength, the next cavity mode becomes resonant. Therefore these cavity modes are called longitudinal modes of the resonator.

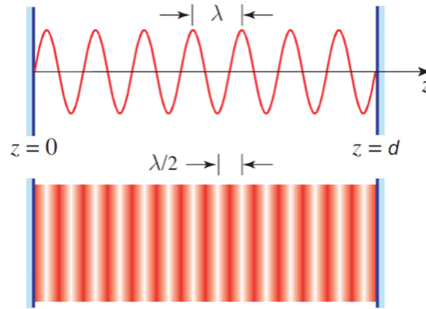


**Figure 2.5:** Transverse amplitude of a resonant light wave with wavelength  $\lambda$  inside a Fabry-Perot cavity with length  $d$ . (Figure from ref. 23)

### 2.3.2 Losses

When one wants to account for losses in the cavity it is easiest to view the light in the resonator as a succession of self-reproducing waves. Suppose we start with a monochromatic plane wave with complex amplitude  $U_0$  entering the cavity through the left mirror. After two reflections by both mirrors the light has made one round-trip and now has complex amplitude  $U_1$ , which after one

more round-trip turns into  $U_2$  etc. Each round-trip, the phase of  $U_n$  changes by  $\phi = 2kd$  and the amplitude is decreased by a factor  $r$  due to losses at the mirrors and absorption by the medium inside the cavity. Therefore, the successive waves are related by an amplitude attenuation factor  $h = re^{-i\phi}$  such that  $U_1 = hU_0$ . The resulting standing wave is a superposition of all round-trips:

$$U = U_0 + U_1 + U_2 + \dots = U_0 + hU_0 + h^2U_0 + \dots = U_0(1 + h + h^2 + \dots) = \frac{U_0}{1 - h} \quad (2.34)$$

The corresponding intensity is now given by

$$I = |U|^2 = \frac{U_0^2}{|1 - re^{-i\phi}|^2} = \frac{I_0}{1 + |r|^2 - 2r \cos(\phi)} \quad (2.35)$$

The phase shift  $\phi$  can be written as  $\phi = 2\pi v/v_{fsr}$  by using (2.33). Plugging this into (2.35) gives

$$I = \frac{I_{max}}{1 + (2\mathcal{F}/\pi)^2 \sin^2(\pi v/v_{fsr})} \quad (2.36)$$

$$\mathcal{F} = \frac{\pi\sqrt{r}}{1 - r}, \quad I_{max} = \frac{I_0}{(1 - r)^2} \quad (2.37)$$

The quantity  $\mathcal{F}$  is called the finesse and is a common used term to characterize a resonator. The higher the finesse, the lower the losses are, corresponding to a high number of roundtrips for each photon inside the cavity. The intensity as function of frequency is plotted in Figure 2.6. The intensity reaches its maximum value when the frequency matches the resonance frequency and the sine in the denominator becomes zero. The Finesse is defined as the ratio of the FSR over the Full Width Half Maximum (FWHM) of the intensity peaks and therefore the width of the resonator modes are given by

$$\Delta v = \frac{v_{FSR}}{\mathcal{F}}, \quad (2.38)$$

which is also known as the linewidth of the cavity. From this relation it is clear that a high finesse cavity has a narrow linewidth, allowing only a small range of frequencies inside the resonator.

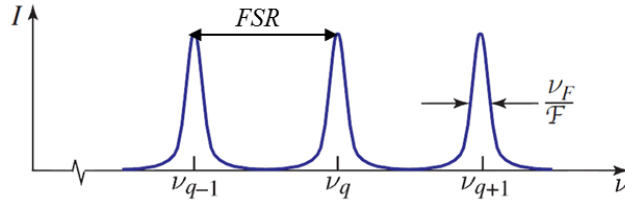


**Figure 2.6:** Light intensity inside an optical resonator as function of frequency, the sharpness of the resonance peaks is determined by the Finesse of the cavity. (Figure from ref. 23)

As mentioned earlier, losses inside a cavity can be attributed to two main sources: losses from the mirrors and losses from absorption by the medium. The

losses at the mirrors are caused by three main effects: first of all the mirrors are often designed to transmit a portion of the light  $T$ , otherwise no light could be inserted in the cavity and no light would come out. Second, despite major efforts by companies to minimize scattering at the surface by applying sophisticated polishing and substrate techniques, mirrors are never perfect and a small fraction of the light will be lost due to scattering from the surface. Third, due to the finite size of the mirrors a small part of the light will leak away when it goes beyond the edge of the mirror. When the mirror reflectivities for the first mirror and the second mirror are given by  $\mathcal{R}_1 = r_1^2$  and  $\mathcal{R}_2 = r_2^2$ , respectively, then the wave intensity decreases with a factor  $\mathcal{R}_1\mathcal{R}_2$  each round-trip. Absorption and scattering by the medium between the mirrors causes the intensity to drop by a constant factor in time, which can be modelled as  $\exp(-2\alpha_a d)$  for each round-trip. Taking both loss types into account, the total round-trip intensity attenuation is modelled as

$$r^2 = \mathcal{R}_1\mathcal{R}_2 \exp(-2\alpha_a d) = \exp(-2\alpha_r d) \quad (2.39)$$

$$\alpha_r = \alpha_a + \frac{1}{2d} \ln(1/\mathcal{R}_1\mathcal{R}_2) \quad (2.40)$$

where  $\alpha_r$  is the effective total attenuation, as a function of  $\alpha_a$  and  $\mathcal{R}_1\mathcal{R}_2$ . Now the finesse can be expressed in terms of  $\alpha_r$ :

$$\mathcal{F} = \frac{\pi \exp(-\alpha_r d)/2}{1 - \exp(-\alpha_r d)} \approx \frac{\pi}{\alpha_r d}, \quad (2.41)$$

where the approximation  $\alpha_r \ll 1$  was used. This relation confirms the earlier result that a high Finesse indicates low losses in the cavity. Because  $\alpha_r$  represents the losses per unit length,  $c\alpha_r$  equals the losses per time and we can define a characteristic decay time  $\tau = 1/(c\alpha_r)$  as the average time each photon stays inside the cavity. The mean path length traversed by the photons in the resonator is then given by

$$\Delta l = c\tau = \frac{1}{\alpha_r} = \frac{L}{\pi} \mathcal{F}, \quad (2.42)$$

where (2.41) was used. When building an optical cavity, it is important that the laser stays coherent within this length. Otherwise, after some time in the cavity the photons will no longer contribute to the standing wave therefore limiting the functionality of the cavity.

### 2.3.3 Stability

So far a cavity with planar mirrors was considered, but it turns out this configuration is highly sensitive to misalignments. When the beam entering the cavity is not exactly parallel with the cavity longitudinal axis, the light will drift from the center by consecutive reflections from the mirrors and is lost from the cavity after a short number of round-trips. The stability of the resonator can be increased by using spherical mirrors. Ray optics and the ABCD law can be used to investigate the stability and confinement conditions for the cavity.

We define the radii of curvature of each resonator mirror as  $R_1$  and  $R_2$ , with  $R > 0$  for convex and  $R < 0$  for concave mirrors. For the case with two planar mirrors in the previous section  $R_1 = R_2 = \infty$ . Assuming paraxial rays (having

small angles with respect to the optical axis) we can construct ray transfer matrices for both mirrors and the medium. Putting these into the ABCD law and demanding that the rays of consecutive round-trips overlap results in the stability condition:

$$0 \leq \left(1 + \frac{d}{R_1}\right)\left(1 + \frac{d}{R_2}\right) \leq 1, \quad (2.43)$$

which can also be written in terms of the so called  $g$  parameters,  $g_1 = 1 + \frac{d}{R_1}$  and  $g_2 = 1 + \frac{d}{R_2}$ :

$$0 \leq g_1 g_2 \leq 1 \quad (2.44)$$

If this condition is satisfied, the subsequent round-trips of light will overlap and the resonator is said to be stable. If not, the cavity is unstable, and the light will quickly 'walk out' of the cavity resulting in a very limited resonance intensity. The stability condition can be visualized with a diagram, as shown in Figure 2.7. Several possible configurations with different radius of curvatures for the mirrors are listed in the figure as well.

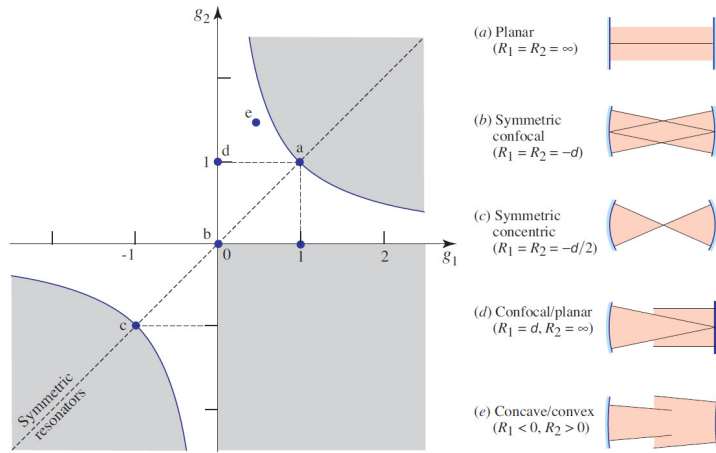


**Figure 2.7:** Resonator stability diagram. If the parameters  $g_1 = 1 + \frac{d}{R_1}$  and  $g_2 = 1 + \frac{d}{R_2}$  lie in the unshaded areas the cavity is stable. Several basic configurations are listed on the right with the letters indicating their position in the diagram. (Figure from ref. 23)

### 2.3.4 Gaussian beams

In addition to the longitudinal modes discussed earlier, optical resonators can also sustain transverse cavity modes, where the fields are normal to the  $z$  axis. These are called  $TEM_{mn}$  (transverse electromagnetic) modes, where the indices  $m$  and  $n$  indicate the integer number of transverse nodal lines in the  $x$ - and  $y$ -direction, respectively. For all applications in this thesis the  $TEM_{00}$  mode is used, because of its complete spatial coherence and the small angular divergence. The  $TEM_{00}$  mode of an optical cavity has a Gaussian profile: the intensity falls off transversely following a bell-shaped curve that is symmetrical around the central axis. To study how light can be coupled into an optical cavity we therefore need to use Gaussian beam optics.

The intensity profile in the  $x$ - $y$  plane of a Gaussian beam is described by an exponential decay function. Its width is characterized by the radius  $w$ , defined as the distance from the axis at which the electric field has dropped by a factor  $e$  from its axial value. The beam radius can be expressed as function of the longitudinal coordinate  $z$ :

$$w(z) = w_0 \sqrt{1 + \frac{z^2}{z_0^2}} \quad (2.45)$$

$$z_0 = \frac{\pi w_0^2}{\lambda} \quad (2.46)$$

At  $z = 0$ , where the focus is, the beam radius takes its minimum value  $w_0$ , called the waist. The beam radius increases in both directions from the focus. A characteristic of the divergence of the beam is the Rayleigh range  $z_0$ , the distance over which the cross-sectional area has doubled from its minimum value at the focus. The radius of curvature (ROC) of the wave front is given by

$$R(z) = z \left( 1 + \left( \frac{z_0}{z} \right)^2 \right) \quad (2.47)$$

and decreases from  $\infty$  at  $z = 0$  towards a minimum at  $z = z_0$ , after which it increases linearly with  $z$ , as is the case for a spherical wave. A Gaussian beam inside an optical resonator will only overlap with itself if the ROC of the mirrors equals that of the wave front. In the far field regime  $z \gg z_0$ , the Gaussian beam is nearly spherical and therefore spherical mirrors can be used. If a spherical mirror is used in combination with a planar mirror, then the latter has to be placed at the focus where the ROC of the Gaussian beam is infinite. If the mirrors have different ROC, the focus will be displaced from the center of the cavity. For now we will assume a symmetric configuration, where the mirrors have equal ROC and the focus is located in the center of the cavity, since for our application of an optical dipole trap we want to trap the molecules in the center of the resonator.

The waist size of a symmetric cavity is obtained by solving (2.45) with  $r$  equal to the ROC of the mirrors:

$$w_0 = \sqrt{\frac{\lambda}{2\pi} \sqrt{d(2r - d)}} \quad (2.48)$$

Where  $z$  was replaced by  $z = 2d$  because we are dealing with a symmetric configuration. This relation is plotted in Figure 2.8 for different mirror curvatures  $r$ . For fixed  $r$ , the waist size is maximal at  $d = r$ :

$$w_{0,max} = \sqrt{\frac{\lambda r}{2\pi}}, \quad (2.49)$$

for which the cavity has a confocal configuration. In this case, the length of the resonator equals twice the Rayleigh length and the beam width at the mirrors is twice the waist size, as shown in Figure 2.9. In this configuration all  $TEM_{mn}$  cavity modes are overlapping, which is a disadvantage because for our applications we want the cavity to sustain only the  $TEM_{00}$  mode. The waist size  $w_0 = 0$  when  $d = 2r$ , which is the concentric configuration. As indicated in Figure 2.7, concentric resonators are at the edge of the stability region. Figure 2.8 is in particular useful in the process of designing a cavity: it can be used to select appropriate mirrors for a desired range of waist sizes.

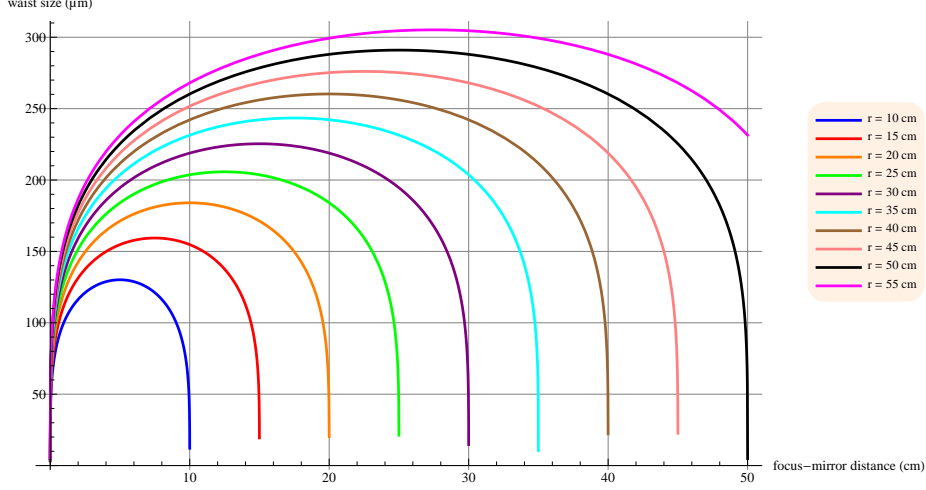


**Figure 2.8:** Waist size  $W_0$  at the focus of a symmetrical optical cavity as function of the cavity length  $d$  for different curvatures of the mirrors  $r$ . ROC of both mirrors are assumed to be the same. The maximum waist size for a given  $r$  occurs in a confocal configuration.

### 2.3.5 Mode matching

So far only the light inside the resonator has been considered, not how to get a laser beam coupled into a cavity. This is usually done via the back of one of the mirrors, which is called the incoupling mirror. After a number of round-trips the light leaves the cavity both through the incoupling mirror, traversing the incoming beam in opposite direction, and through the back mirror (outcoupler). Light leaking through the outcoupling mirror is usually used to monitor the behaviour of the cavity.

In order for light to be coupled into the cavity the incoming light should have the same parameters as the resonating light. For a Gaussian beam this means the beam waist, radius of curvature and focal position should match. This can be achieved by placing one or more lenses in the beam path before the cavity. We will start by assuming the fixed beam parameters for the cavity and calculate how we can match these parameters by placing one lens in a collimated laser beam. The cavity waist size is given by  $w_{0cav}$  and its Rayleigh range is  $z_{0cav} \equiv \pi w_{0cav}^2 / \lambda$ . Because the incoming light traverses through the spherical incoupling mirror both its waist size and the focus position are changed. Constructing the ray matrices and using the ABCD law we can calculate the virtual waist  $w_{0vir}$  and focus position  $z_{vir}$  the incoming light should have in order to match  $w_{0cav}$  and  $z_{0cav}$ <sup>22</sup>:

$$w_{0vir} = w_{0cav} \sqrt{\frac{z_{0cav}^2 + (d/2)^2}{z_{0cav}^2 + n^2(d/2)^2}} \quad (2.50)$$

$$z_{vir} = n \frac{dw_{0vir}^2}{2w_{0cav}^2} + \frac{t}{n} \quad (2.51)$$

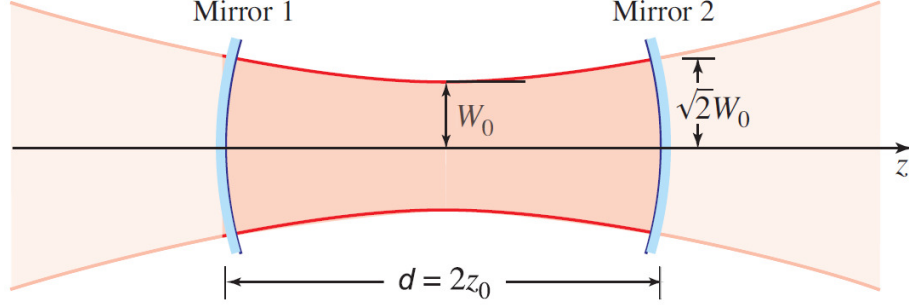


**Figure 2.9:** A Gaussian beam in a symmetric confocal cavity with concave mirrors. (Figure from ref. 23)

Here  $n$  is the refraction index of the mirror and  $t$  is the thickness. The beam after the mirror behaves as if it had a virtual focus at position  $z_{vir}$  with a virtual waist  $w_{0vir}$ , while the real focus is altered by the mirror and has  $z_{0cav}$  and  $w_{0cav}$  as indicated in Figure 2.10.

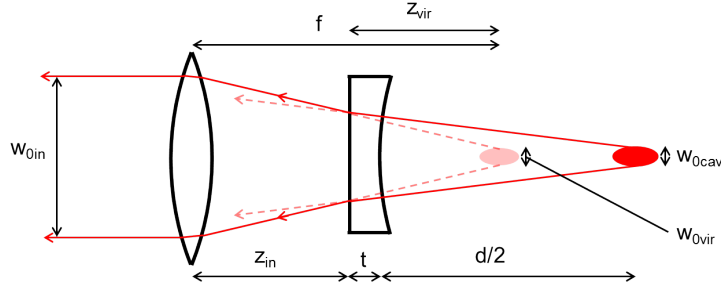


**Figure 2.10:** Schematic drawing of the mode matching optics. The incoupling mirror changes the position and waist of the focus of the incoming collimated beam to  $z_{vir}$  and  $w_{0vir}$  respectively.

Having determined waist size the focus of the incoming beam should have, we can now calculate the waist size  $w_{0in}$  of the incoming collimated beam before it is focused by a lens with focal length  $f$ :

$$w_{0in} = \frac{f\lambda}{\pi\sqrt{2}w_{0vir}} \sqrt{1 + \sqrt{1 - \left(\frac{2\pi w_{0vir}}{f}\right)^2}} \quad (2.52)$$

So the parameters of the incoming beam are matched with those of the light inside the cavity when both of these requirements are fulfilled:

- The waist size of the incoming collimated beam equals  $w_{0in}$ .
- A lens with focal length  $f$  is placed at distance  $z_{in} = f - z_{vir}$  from the incoupling mirror.

### 2.3.6 Power enhancement

In section 2.3.1 we derived the total intensity of the light inside a Fabry-Perot resonator as function of the intensity of the first round trip  $I_0$ . We saw that the intensity reaches a maximum at the resonance frequencies  $\nu_q$ , where the light forms a standing wave between the cavity mirrors. The many round-trips inside the cavity cause the intensity to be much higher than the incoming light intensity. To calculate the intensity enhancement, or power enhancement, we can use (2.37):

$$A = \frac{4I_{max}}{I_{in}} \approx \frac{4I_0}{I_{in}(1-r)^2} = \frac{4I_{in}(1-r)}{I_{in}(1-r)^2} = \frac{4}{1-R} \quad (2.53)$$

Where, as before, equal mirror reflectivities  $r$  close to 1 are assumed, losses are neglected and  $I_{in}$  is the intensity of the incoming light before it passes through the incoupling mirror. The factor 4 appears because the light inside the cavity interferes constructively, therefore doubling the electric field amplitude, resulting in a factor 4 increase in intensity. One can also express the enhancement in terms of the finesse:

$$A \approx \frac{4\mathcal{F}}{\pi} \quad (2.54)$$

Which is useful as a quick and easy indication of the power enhancement for a given Finesse. To get maximum power enhancement, the cavity should have a very high Finesse, which is achieved by using high reflectivity mirrors to store as much light as possible in the cavity (see (2.37)). However, to couple the light into the cavity the incoupling mirror should have a low reflectivity in order to reach a high incoupling efficiency: with very high reflectivity mirrors only a very small fraction of the light can enter the cavity. Both requirements contradict each other and therefore a trade-off for the reflectivity of the first mirror must be made between a high finesse and a high incoupling efficiency. To find the optimal value for the reflectivity of the first mirror  $\mathcal{R}_1$ , we take the power enhancement from (2.53) but instead of assuming equal mirror reflectivities  $r$  we plug in (2.40) allowing for different mirror reflectivities  $\mathcal{R}_1$  and  $\mathcal{R}_2$  and also including losses:

$$A = \frac{1 - \mathcal{R}_1}{(1 - \sqrt{\mathcal{R}_1 \mathcal{R}_2} \exp(-2\alpha_a d))^2} \quad (2.55)$$

Now by setting the derivative with respect to  $\mathcal{R}_1$  to zero we obtain the optimal value for  $\mathcal{R}_1$ :

$$\frac{\partial A}{\partial \mathcal{R}_1} = 0 \rightarrow \mathcal{R}_1 = \mathcal{R}_2 e^{(-2\alpha_a d)} \quad (2.56)$$

This equation is called the impedance matching condition. When losses are negligible the impedance matching condition gives equal mirror reflectivities for both mirrors. However, as the losses are becoming significant one should choose the mirror reflectivities according to the above relation to maximize the power enhancement of the cavity.

## 2.4 Optical dipole trap

An optical dipole trap (ODT) is an experimental technique where a strong light field is used to trap particles in a region in space. The working principle is based on the dipole force for which particles possessing a non-zero polarizability are subject to a potential depending on the light intensity. This particles can be atoms as well as molecules and usually trapping also works for different internal states at the same time. The depth and spatial extension of the trap are determined by both the frequency and the intensity of the light field used.

### 2.4.1 Dipole force

The working principle of an optical dipole trap is based on dipole force, arising from the interaction of the electric component of the light field and the particle. When an electric field  $\mathbf{E} = E_0 \exp(-i\omega t)\hat{\mathbf{e}}$  interacts with a particle (either atom or molecule), a dipole moment  $\mathbf{p}$  is induced, which depends on the (scalar) complex polarizability  $\tilde{\alpha}$ <sup>25</sup>. The amplitude of the dipole moment is given by:

$$p = \tilde{\alpha}E \quad (2.57)$$

The interaction potential between the electric field and the induced dipole moment is given by the following integral<sup>26</sup>:

$$U_{\text{dip}} = \int_0^E -\alpha \mathcal{E} d\mathcal{E} = -\frac{1}{2}\alpha E^2 \quad (2.58)$$

Where  $\alpha$  denotes the real part of the complex polarizability  $\tilde{\alpha}$ . The factor 1/2 occurs because the dipole moment is an induced one; for permanent dipoles this factor does not occur. The resulting force is the gradient of the interaction potential:

$$\mathbf{F}_{\text{dip}} = -\nabla U_{\text{dip}}(\mathbf{r}) = \frac{1}{\epsilon_0 c} \alpha \nabla I(\mathbf{r}) \quad (2.59)$$

Where the intensity is  $I = \frac{1}{2}\epsilon_0 c E_0^2$ . The potential gives rise to a conservative force, proportional to the gradient of light intensity. Thus, when concentrated on a single focus point, the particles will be attracted (or repulsed, which will be discussed in the next section) to the high intensity region. For a Gaussian beam the peak intensity  $I_0$  is related to the total laser beam power  $P_0$  by:

$$I_0 = \frac{2P_0}{\pi w_0} \quad (2.60)$$

Therefore we can express the potential depth of an optical dipole trap created by the focus of such a laser beam by<sup>27</sup>:

$$U_{\text{ODT}} = -\frac{1}{\epsilon_0 c} \alpha I_0 = -\frac{1}{\epsilon_0 c} \alpha \frac{2P_0}{\pi w_0^2} = -\frac{2\alpha}{\pi \epsilon_0 c w_0^2} P_0 \quad (2.61)$$

### 2.4.2 Stark Shift

Another way of viewing the dipole force is via the Stark shift. The electric component of a light field causes a shift in the energy levels of the atom or molecule, as in Figure 2.11. The magnitude of this shift depends on local light intensity,

and therefore varies in space in a Gaussian laser beam. The direction of the shift depends on the frequency of the trapping laser: if the wavelength of the laser is smaller than the energy splitting of the two relevant levels (blue-detuned), the splitting between both levels becomes larger and the force points towards regions with lower intensity. Consequently, the molecules will be repulsed by the light beam and an anti-trap is created. If however the wavelength is larger than the energy splitting (red-detuned), the force will attract the molecules towards the regions with higher intensity. Thus, by using red detuned light, molecules can be trapped into the focus of a laser beam.

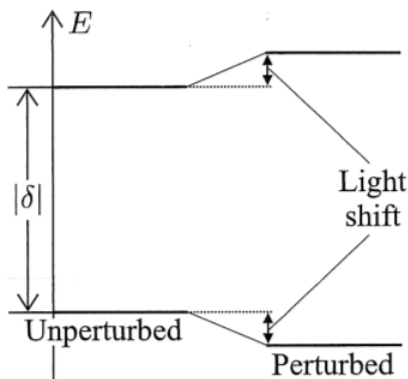


**Figure 2.11:** Shift in energy levels due to a light field. (Figure from ref. 26)

The selection of the right trapping wavelength is critical for the functionality of the dipole trap. When the operating frequency is close to a transition, scattering will be increased and can cause molecules in the trap to heat, and eventually they will escape from the trap. To minimize the scattering, a large detuning is preferred. When the detuning is very large, the resulting trap is called a Far Off Resonance Trap (FORT). If the detuning is increased even more, the molecules do effectively experience a static potential, and a Quasi Electrostatic Potential (QUEST) is formed.

### 2.4.3 Optical lattice

When a single focused beam is used to create a dipole trap, the trap will be cigar-shaped like the focus of the beam. The confinement in the radial direction will be stronger than the confinement in the axial direction. However, when using an optical cavity to create the dipole trap, the trapping light will form a standing wave. Because the molecules are attracted to the region of highest intensity, they accumulate at the anti-nodes of the standing wave. The trapping potential is then given by<sup>27</sup>:

$$U(r, z) = -\frac{4U_0}{1 + z/z_0} \exp\left(-\frac{2r^2}{\omega_0\sqrt{1 + (z/z_0)^2}}\right) \cos^2(kz) \quad (2.62)$$

Where the trap depth  $U_0 = U_{ODT}/2$  and  $r$  is the radial coordinate. We see that the dipole trap actually consists of a large number of pancake-shaped traps

separated by half the trapping wavelength. This is known as an optical lattice and is shown schematically in Figure 2.12.

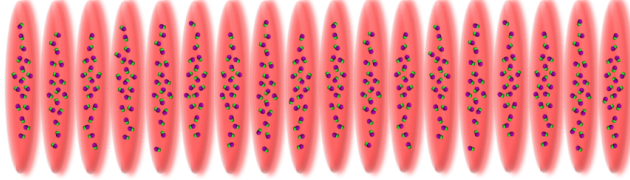


**Figure 2.12:** Schematic drawing of SrF molecules accumulating in the antinodes of a standing wave inside a cavity, forming a 1D optical lattice.

Once captured in the dipole trap, the molecules oscillate in all directions following the conservative potential of the dipole force. As long as the magnitude of the oscillations is much smaller than the trap depth, i.e. the molecules are not far from the center of the trap, the potential can be approximated as harmonic. The trap oscillation frequencies in a 1-D optical lattice are then given by<sup>28</sup>:

$$\omega_{axial} = \frac{2\pi}{\lambda} \sqrt{-\frac{2U_{dip}}{m}} \quad (2.63)$$

$$\omega_{radial} = \frac{2}{\omega_0} \sqrt{-\frac{U_{dip}}{m}} \quad (2.64)$$

Where  $m$  is the mass of the molecule and  $\omega_{axial}$  and  $\omega_{radial}$  are the angular frequencies in the direction of the trapping beam and in any direction orthogonal to the trapping beam, respectively. Because the axial length of the traps is very small (on the order of half a wavelength of the trapping beam) compared to the radial width (typically  $> 10\mu\text{m}$ ),  $\omega_{axial}$  is much larger than  $\omega_{radial}$  in an optical lattice. For a focused beam dipole trap however, the opposite is the case: the axial length of the cigar shaped trap is larger than the radial width so  $\omega_{axial}$  will be smaller than  $\omega_{radial}$ .

## 2.5 Cavity ring-down spectroscopy

Cavity ring-down spectroscopy (CRDS) is a technique for performing sensitive direct absorption measurements developed in the late 1980's. The main idea of this technique is to reflect the laser light back and forth many times inside an optical cavity and measure the decay of the light. In comparison to traditional spectroscopy experiments, where the light passes the sample just once, it is mainly the largely increased effective path length that results in a much higher sensitivity. Spectroscopy experiments, in general, use the absorption and emission of light by the sample of atoms or molecules. The Beer-Lambert law relates the intensity of the spectrum to the absorption by the sample<sup>29</sup>:

$$I = I_0 \exp(-\alpha l) \quad (2.65)$$

Where  $I_0$  is the incoming light intensity and  $I$  the intensity leaving the sample,  $l$  is the length of the sample and  $\alpha = \sigma(v)N$  the absorption coefficient with  $\sigma(v)$  the frequency dependent absorption cross-section of the sample and

$N$  the number of absorbing molecules per unit volume. A spectrum of a simple absorption measurement is obtained by measuring the small light attenuation on top of a large background signal of the incident beam. The resolution of such a spectrum is limited by the ratio of the small intensity deviation versus the large background.

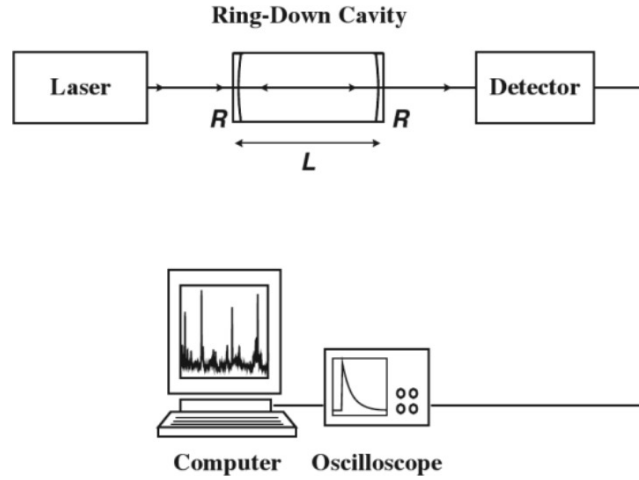


**Figure 2.13:** Schematic overview of a simple CRDS experiment. A laser pulse is sent through an optical cavity, with length  $L$  and mirror reflectivities  $R$ , containing the sample molecules. A detector measures the light leaking away through the back cavity mirror after a number of round trips. The exponential decay of the intensity characterizes the losses inside the cavity. (Figure from ref. 29)

A basic CRDS setup is shown schematically in Figure 2.13. A light pulse from a laser is coupled into a high finesse optical cavity with length  $L$  and mirror reflectivities  $R$  typically  $> 99.9\%$ . While the light pulse is trapped inside the cavity, bouncing back and forth between the mirrors, a small part leaks away through the back and front mirror and the leak intensity through the back mirror is measured by a photodiode. The leak intensity is described by the differential equation

$$\frac{dI}{dt} = -\frac{cT}{L}I \quad (2.66)$$

with  $c$  speed of light and  $T$  the transmission of the mirrors. When assuming no scattering or other losses in the mirrors  $T$  is related to  $R$  by  $T = 1 - R$ . The solution in terms of the ring-down time  $\tau = \frac{L}{cT}$  yields<sup>30</sup>

$$I(t) = I_0 \exp\left(-\frac{t}{\tau}\right). \quad (2.67)$$

So far only losses through the mirrors have been considered, but when placing the sample of interest inside the optical cavity additional losses due to absorption will occur. Therefore the molecular absorption coefficient  $\alpha$  from equation 2.65 should be added to the losses for each roundtrip, resulting in a modified ring-down time

$$\tau = \frac{L}{c(T + \alpha L)}, \quad (2.68)$$

where the length of the sample is taken equal to the length of the cavity  $L$ . Thus when recording the leak intensity, an exponential decay with time constant  $\tau$  will be obtained. With  $\tau$  being sensitive to both the mirror transmission and the molecular absorption, an absorption spectrum can be obtained after subtracting the transmission losses. Because of the high reflectivity of the mirrors, the effective path length of the light passing through the sample is greatly enhanced: for example with  $R = 99,99\%$  and a sample length of 20 cm, the effective path length is increased to 1 km. In practice a higher reflectivity boils down to a bigger change in the time constant, therefore increasing the sensitivity<sup>17</sup>. On the other hand, when increasing the reflectivity, less light can be coupled into the cavity, therefore reducing the intensity on the detector. As can be seen from equation 2.68, the ring-down time is independent of the incident light intensity. This offers the great advantage that fluctuations in the laser beam intensity do not influence the sensitivity of the measurement.

## Chapter 3

# Acetylene spectroscopy

This chapter reports on the acetylene spectroscopy project. First an overview of the experimental setup is given and the most important parts are described. The next section explains the measurement sequence and the way the data is analyzed. Subsequently, the results are presented and discussed, leading to a conclusion and outlook of the experiment.

### 3.1 Experimental overview

The experimental setup for measuring higher overtones of acetylene was already used before to perform spectroscopy in different ways on vibrational overtones of several molecules<sup>3, 31</sup>. For the current project, the setup was slightly changed to make it suitable for the new method of two photon excitation combined with CRDS.

#### 3.1.1 The laser system

The laser system consists of two main laser beam lines, a pump beam in the near infrared (IR) regime and a probe in the mid-IR regime. An overview of the setup is shown in Figure 3.1, where both beam paths are marked.

The laser beam in the visible regime, for exciting acetylene by several vibrational quanta, is produced by a Ti:sapphire ring laser (Coherent 899). This laser is tunable over a range from 700-1000 nm with three different sets of mirrors and has a linewidth around 20 MHz. Coarse- to fine tuning is achieved by a thick etalon, a galvo plate and a thin etalon, respectively. The output power of 1 W is sufficient for all experiments performed. The ring laser is pumped by a Coherent Verdi V-10 pump laser producing a 532 nm beam up to 10 W pump power. The wavelength of the ring laser is measured using a fiber coupled wavemeter with a resolution of  $0.01\text{cm}^{-1}$ . After exiting the ring laser, the beam is focused and directed through an AOM, which enables shutting off the beam needed for the cavity ring-down measurements. The first order deflected beam, containing  $\sim 35\%$  of the original power, is sent through two mode matching lenses. In the focus of the first lens a pinhole is located, which ensures the beam is nicely Gaussian shaped for optimal mode matching. After the second lens the beam is reflected by two right-angled mirrors on a micrometer translation

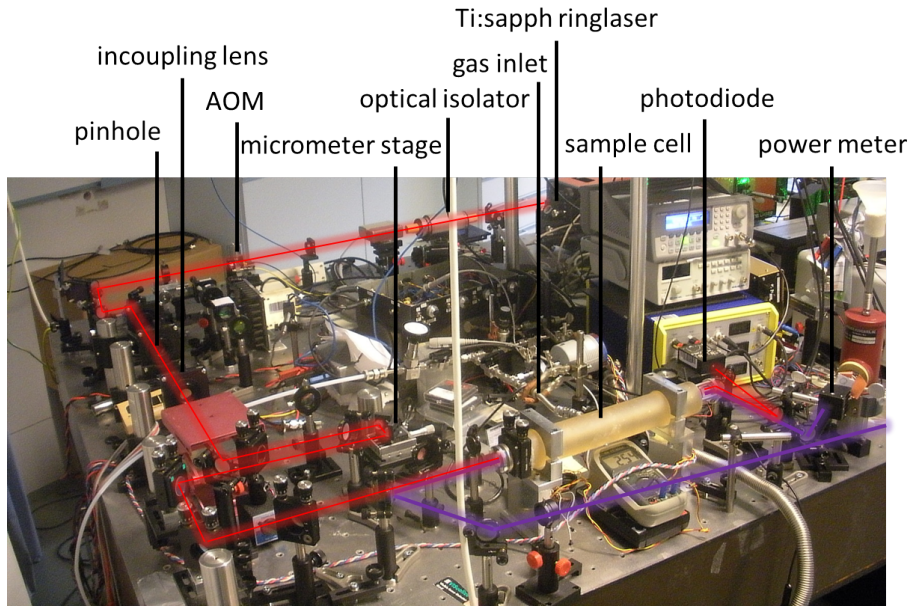


**Figure 3.1:** Overview of the experimental setup. The infrared pump beam path is marked purple and enters from the right. The visible pump beam is marked red and enters from top.

stage. With this stage the distance between the cavity and the mode matching optics can be fine-tuned to reach optimal incoupling of the light into the sample cell cavity, without changing the mutual distances between the lenses and the pinhole.

The mid-IR beam is produced by a home-built optical parametric oscillator (OPO), which is fed by a near-infrared beam. An overview of the OPO setup is shown in Figure 3.2. The OPO consists of a PPN-doped crystal, with 10 different poling periods, which is placed inside a optical cavity in bow-tie configuration. The cavity mirrors have a high reflectivity for the signal beam, while the pump and idler beam are mostly transmitted. To prevent damaging the crystal, it is heated to  $\sim 60^\circ C$ . In order to select only one frequency component a thin etalon is placed in the cavity, under a small angle relative to the signal beam.

The output frequency of the OPO is tunable over a broad range within the mid-IR: from  $\sim 2450nm$  to  $\sim 3900nm$ . Coarse- to fine tuning of the frequency is done by changing the poling period of the crystal, tuning the frequency of the input light and changing the temperature of the crystal, respectively. The threshold input power for the OPO is  $\sim 2.5W$  and an output power of  $100mW$  can be reached easily.

The OPO is pumped by a near-infrared beam from a Ti:sapph ring laser, which is tunable from  $750nm$  to  $850nm$ . Coarse tuning of the Ti:sapph is provided by a manually adjustable thick etalon while fine tuning of the frequency is done by a thin etalon via the control box. At maximum pump power the ring laser produces  $\sim 4.5W$ . The frequency of the OPO is measured with a wavemeter (EXFO) with a resolution of  $.005cm^{-1}$ . The short term stability ( $\leq 5$  min) of the OPO is better then the resolution of the wavemeter, but for

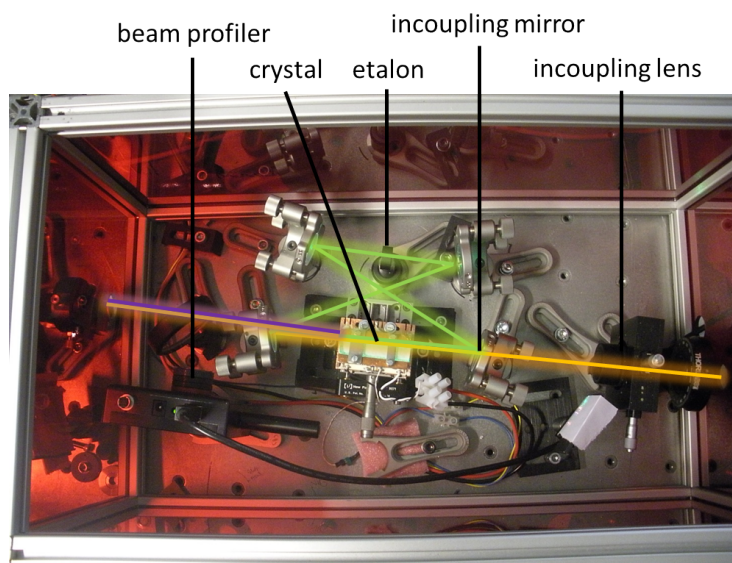


**Figure 3.2:** Overview of the OPO setup. The OPO pump beam is marked orange and enters from the right. The signal beam, marked green, is generated inside the crystal and circulates inside the cavity. The idler beam is marked purple and exits to the left, towards the sample cell.

longer timescales manual corrections in the pump frequency are necessary to keep the frequency at the desired value. These drifts are mainly caused by the ring laser while mode hops mostly occur inside the OPO.

The Ti:sapph ring laser is pumped by a Coherent Verdi pump laser with an wavelength of 532 nm and an output power up to 20W. However, due to some internal malfunction the output power of the device was limited to 17,5W during most experiments.

### 3.1.2 The sample cell

In the sample cell, schematically shown in Figure 3.3, the light of both lasers interacts with acetylene molecules. The cell consists of a cylindrical tube of Zerodur glass with low thermal expansion, closed off by the cavity mirrors on each end. The cell is connected to a mechanical vacuum pump and an acetylene gas bottle, such that the pressure of acetylene inside the sample cell can be regulated. A typical pressure used in the experiments was 1 mbar. A higher pressure leads to a stronger absorption signal, but also to larger losses from the intermediate state due to collisions, which lowers the absorption signal. The optimal value was found to be around 1 mbar in earlier experiments<sup>3</sup>.

The visible light beam  $TEM_{00}$  mode is coupled in the cavity through the flat front mirror, aligned to the center axis of the sample cell. The back mirror has a radius of curvature of 1 meter, while the front mirror is flat, and both mirrors have a reflectivity  $> 99.98\%$  for the Ti:sapph wavelength, while the reflectivity for the OPO-beam is low. The cavity length is scanned by a piezo actuator ring clamped between the glass cylinder and the back mirror. When the cavity comes into resonance with the incoupled light, that is when the cavity length

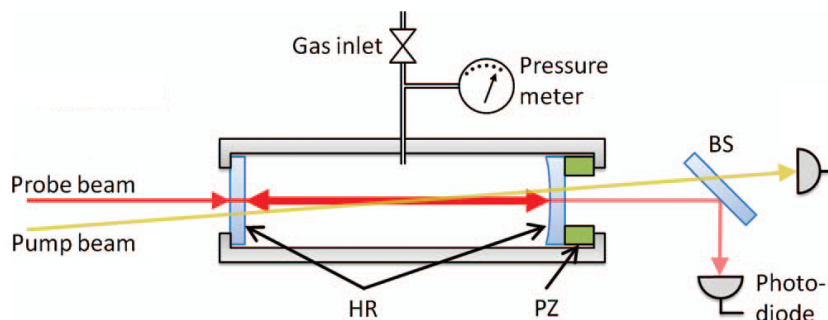


**Figure 3.3:** Schematic overview of the sample cell, made out of Zerodur glass. The pump beam is generated by the OPO and traverses the sample once before it is being detected by a power meter. The probe beam forms a standing wave when it is in resonance with the high reflectivity mirrors of the cavity, of which the length is scanned by a piezo. The exponential decay of the light intensity is recorded by a photodiode

equals an half-integer times the wavelength of the light, power starts to build up inside the cavity. This is measured by the high frequency photodiode behind the back mirror and when the intensity reaches a defined threshold, a home-built comparator switches off the AOM. The incoupled light drops instantly to zero and the light in the cavity starts to leak away through both mirrors. This results in an exponential decay of in the intensity recorded by the photodiode. The decay time  $\tau$  is a very sensitive measure for all losses from the cavity. Because losses through transmission of the mirrors are constant, changes in  $\tau$  directly reflect absorption peaks of the sample molecules.

The OPO-beam is directed into the cavity almost parallel to the visible beam, just under a slight angle of  $\sim 0.5^\circ$  such that they overlap in the middle of the cavity. Because of the high transmission of the cavity mirrors, the OPO beam makes a single pass through the sample cell and is then separated from the leaking part of the visible beam by a dichroic mirror. Detection by a thermal power meter was usually sufficient to detect the absorption peak. Inside the sample cell the power of the OPO beam is  $\sim 30$  mW.

### 3.1.3 Data acquisition

The cavity ring-down times were recorded with a National Instruments DAQ-card. A home-built Labview program gives both a real time estimation of the ring-down time and saves the raw data to a binary file. The fitting and averaging of all the exponentials is done on a separate PC by a C++ script. In this way, faster acquisition rates can be achieved. For the measurements performed here, the repetition rate of the ring-down signals was usually 40 Hz. After the data is processed by the script, the standard deviation of the noise on the ring down time without any absorption peaks present, while at a stable frequency, is 0.02%.

### 3.1.4 ECDL setup

Because the above described setup did not give satisfying results within reasonable time, a change in the setup was made. Exciting the molecules by several vibrational quanta results in very weak transition peaks, therefore it was decided

to first try to excite the molecules by just one or two quanta and then later move on to more quanta. Because these transitions are out of the Ti:sapph range we needed to switch to a different laser, a near infrared commercial External Cavity Diode Laser (ECDL) (New Focus, Velocity 6328) which was also used for other CRDS experiments. This laser is tunable between  $6350\text{ cm}^{-1}$  and  $6575\text{ cm}^{-1}$  and has an output of about 20mW with a linewidth  $\sim 1\text{ MHz}$ <sup>32</sup>. An overview with the ECDL laser is shown in Figure 3.4, with the beam path marked.

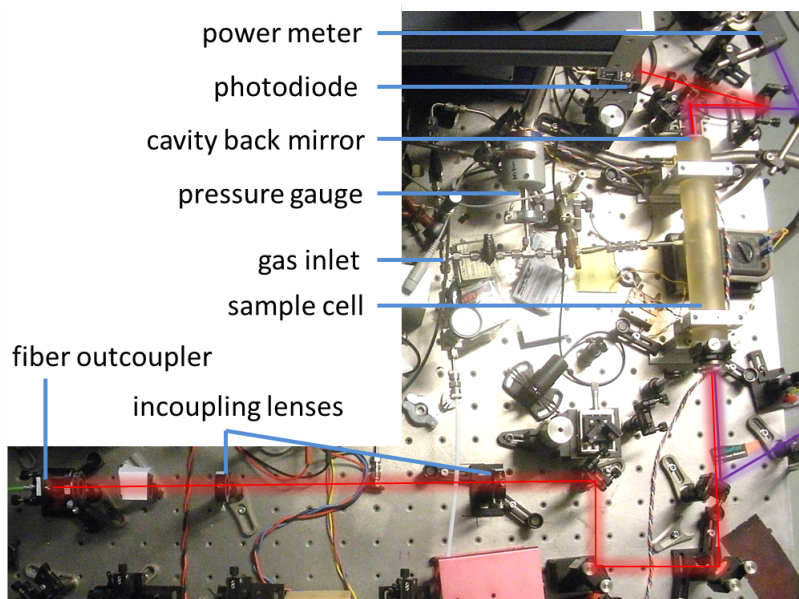


**Figure 3.4:** Overview of the ECDL setup. The infrared pump beam is marked purple and enters from the right. The visible probe beam is marked red and enters from the optical fiber.

The wavelength is measured by a wavemeter (EXFO, WA-1500) with a resolution of 40 MHz. For the ECDL laser a separate beam path to the sample cell cavity was used because different mirrors were required by the larger wavelength. After passing through an AOM the beam is directed through a polarizing beam splitter and a  $\frac{\lambda}{2}$ -waveplate and coupled into a polarization maintaining multi-mode optical fiber. Because of the Gaussian shape, the output of the fiber can be coupled straight into the cavity without the need for a pinhole. Two mode matching lenses optimize the coupling into the cavity. The cavity mirrors, the dichroic beam splitter mirror and the photodiode were replaced by similar ones suitable for the new wavelength. Also the data acquisition system was changed to a different Labview program, now working with a fast 12-bit data acquisition card (Gage, Compuscope 12100).

## 3.2 Performing the experiments

Previous tries to measure higher overtones of acetylene by Mikael Siltanen using this unique two photon CRDS setup did not succeed, probably due to lack of time and uncertainties in the exact frequencies of the overtones. These over-

tones have never been measured before and therefore one has to rely on the theoretical predictions of the frequencies, in which some uncertainties are involved. Moreover, also the experimental method of two photon excitation is new. To avoid having too much uncertainties it was decided to first try the new method on a molecule with well known transitions in order to optimize the signal before moving on to acetylene. A very suitable candidate for this is the water molecule, being a simple molecule with transitions in the same frequency regime as acetylene and very well documented. Because normal water is very abundant in room air, hitting a resonance would cause the laser beams to decrease in intensity considerably before they even reach the sample cell. To avoid this we choose a heavy water isotope,  $\text{H}_2^{18}\text{O}$ . For this molecule a set of suitable transitions was selected for both the OPO and the Ti:sapph beam, shown in Table 3.1.

Transition, normal and (local) notation	Laser	Transition frequency ( $\text{cm}^{-1}$ )
$000(00^+) \rightarrow 001(10^-)$	pump	3674.3475
$001(10^-) \rightarrow 202(31^+)$	probe	10504.4721
$001(10^-) \rightarrow 500(50^+)$	probe	13169.0504
$000(00^+) \rightarrow 001(10^-)$	pump	3823.1267
$001(10^-) \rightarrow 500(50^+)$	probe	13020.2712
$000(00^+) \rightarrow 001(10^+)$	pump	3843.8485
$001(10^+) \rightarrow 401(50^-)$	probe	13009.9778

**Table 3.1:** Transition frequencies for  $\text{H}_2^{18}\text{O}$  for both the first excitation with the OPO (pump) laser beam and the second step by the Ti:Sapph (probe) laser. Transition frequencies are obtained from HITRAN<sup>33</sup>.

### 3.2.1 Measurements on heavy water

To obtain a gas sample of heavy water molecules from the available liquid substance, the water was evaporated under vacuum pressure ( $\sim 10^{-4}$  mbar). A thermodynamic equilibrium between the gas and liquid phase is formed and fills a bottle of gaseous heavy water with a pressure of  $\sim 25$ mbar, which is the vapour pressure of water at room temperature. After filling the sample cell with the heavy water up to a pressure of 1 mbar, the OPO beam was sent through and tuned exactly at the transition denoted in Table 3.1. The OPO power sent in the cavity is 100 mW and when non-resonant the measured power after the cavity was around 11 mW, which implies roughly 10% of the infrared light is transmitted through both cavity mirrors. As expected, the power meter behind the sample cell detects a drop in intensity when the laser is at resonance, as shown in Figure 3.5.

The OPO beam is kept at the maximum of the absorption peak during the rest of the experiment to populate the (001) vibrational state. The Ti:Sapph laser beam is sent through the sample cell and its frequency is scanned across the resonance listed in table 3.1 by rotating the galvo plate inside the laser cavity with a scan rate of approximately  $0,008 \text{ cm}^{-1}/\text{min}$ . The cavity length is scanned over one free spectral range with 40 Hz, resulting in 80 exponential decay curves being recorded by the data acquisition card in the PC every second. After the scan has completed, the curves are fitted by exponentials and the corresponding

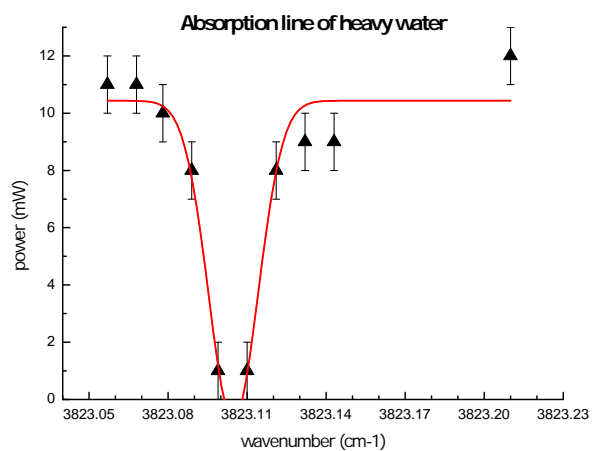


**Figure 3.5:** Measured power behind the sample cell filled with 1 mbar  $H_2^{18}O$  as function of wavenumber. The red line is represents a fit of a Gaussian line shape with FWHM of  $0.022\text{ cm}^{-1}$  centered at  $3823.105\text{ cm}^{-1}$ .

decay times are averaged and saved. The resulting plot of three successive scans is shown in Figure 3.6.

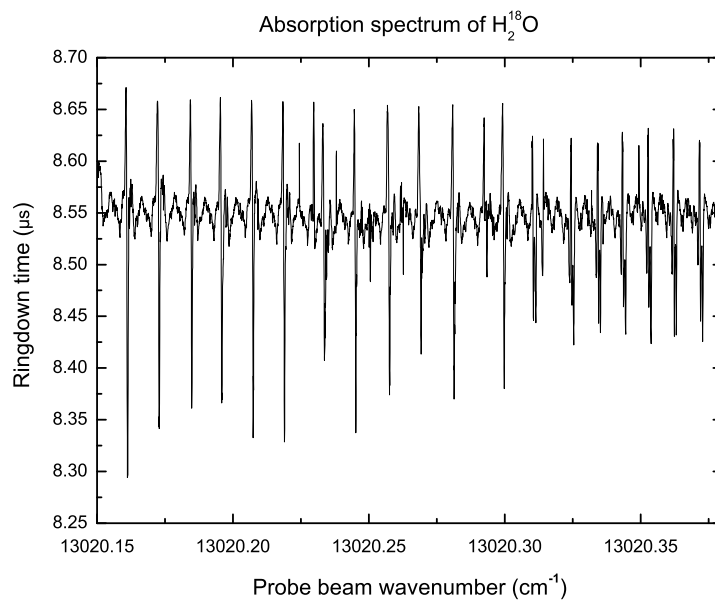


**Figure 3.6:** Three successive scans of the  $H_2^{18}O$  spectrum around the  $303 \rightarrow 212$  vibrational resonance, at  $13020.2712\text{ cm}^{-1}$ . The repetitive peak pattern is an artifact due to the piezo scanning of the cavity and does not represent any absorption features of the sample molecules.

The plot of the ring-down times shows a repeating pattern of peaks and dips. It turns out these peaks occur when the resonance peak in the optical cavity is at a specific position of the piezo ramp. The peaks repeat after  $0.012 \text{ cm}^{-1}$ , which is almost exactly one free spectral range (FSR) of the cavity (430 MHz). It can be seen that not only the major peaks and dips repeat, but also the smaller variations in the ring-down time show a repeating pattern with the same length. Therefore it is clear that most of the peaks visible in Figure 3.6 are not a spectral feature of the sample molecules but are caused by some effect related to the scanning of the optical cavity. A detailed picture of the mounting of back mirror and the piezo stack is shown in Appendix A. As a result of previous experiments performed with this setup the piezo stack is quite thick, allowing for large scans of the cavity length. This feature was used in earlier experiments, but for the current setup we only need to scan a single FSR. Because of its thickness however, the piezo stack could cause the mirror to tilt slightly at a certain point in the scan, being no longer exactly perpendicular to the laser beam axis. When the mirror is slightly tilted the finesse of the cavity drops and the ring-down time, which is very sensitive to any losses of light in the cavity, decreases as well. The piezo stack changing the angle of the mirror during the scan is probably the cause of the peaks and dips shown in the absorption spectrum.

From the plot in Figure 3.6, it is clear the expected absorption peak (303)  $\rightarrow$  (212) at  $13020.2712 \text{ cm}^{-1}$  is not resolved. Several possible improvements were tried resolve the second resonance step of  $\text{H}_2^{18}\text{O}$  :

- Pressure of  $\text{H}_2^{18}\text{O}$  in the sample cell was varied between 0.5 mbar and 10 mbar.
- Different scan rates between  $0.005$  and  $0.1 \text{ cm}^{-1}/\text{min}$ .
- Several different transitions schemes of  $\text{H}_2^{18}\text{O}$  were tried, as listed in Table 3.5. However for the (000)  $\rightarrow$  (001) transition the OPO did produce only very little power due to a normal water absorption line inside the crystal. Therefore mainly the (000)  $\rightarrow$  (001), with different rotational levels, and (000)  $\rightarrow$  (100) transitions were used.

Despite efforts and these changes, the higher overtones of  $\text{H}_2^{18}\text{O}$  were not observed. Probably the lack of signal is due to the very low transition strength. Therefore it was decided to first try the experimental setup and optimize the signal using a stronger transition.

### 3.2.2 Measurements on acetylene

Instead of the higher overtones transitions we now aim for an absorption measurement of acetylene going up by just two vibrational quanta instead of five. This should increase the transition strength by several orders of magnitude and therefore the spectra should be easier to resolve. In Figure 3.7 the two relevant transitions for the pump and probe beam is shown. The intermediate state ( $0010^00^0$ ) is metastable, having a lifetime  $\sim$  ms. The sample molecules are first taken to this level by the pump beam and from there excited to the upper state. In Table 3.2 a number of the relevant calculated transition frequencies is listed, selected such that they are in the range of our lasers.

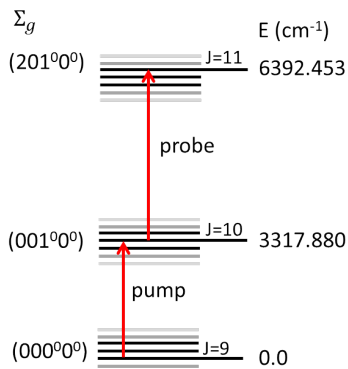


**Figure 3.7:** Energy level scheme of acetylene with the measured probe and pump beam transitions indicated.

To fill the sample cell with acetylene molecules, a bottle with gaseous acetylene under high pressure is connected and the pressure in the sample cell is regulated to 1 mbar via two pressure valves. The experiment is carried out in the same way as in the case for the heavy water measurements, i.e. the OPO (pump) beam is kept at the maximum of the absorption peak from the first excitation step while the Ti:sapph (probe) beam is scanned across the second excitation step.

### 3.3 Results

In this section the results of the measurements on the lower overtones of acetylene are presented and discussed. They are obtained with the ECDL setup as described before. In Figure 3.8 the results of two scans are shown: one with the pump beam turned off and one with the pump beam being present. Both curves show a large variation in the ring-down time (RDT) caused by a nearby strong acetylene absorption line at  $6392.4137 \text{ cm}^{-1}$ . This can be viewed as the background signal, the interesting feature is the dip in ring-down time in the black curve around  $6392.395 \text{ cm}^{-1}$ . The dip indicates a higher absorption with the pump beam than without the pump beam. The absence of the dip while the pump beam is turned off proves this absorption dip represents the second resonance step of the acetylene molecules.

The dip in Figure 3.8 does however consist only of a few data points and the shape is therefore not clearly resolved. This was due to a limitation in the data acquisition system of the ECDL laser; each RDT is assigned to the frequency value measured by the wavemeter, which has a resolution of  $0.001 \text{ cm}^{-1}$ . Even though data points are collected with  $\Delta f < 0.001 \text{ cm}^{-1}$ , this information is lost because they are rounded to the closest value from the wavelength meter. To circumvent this problem and get a better resolution, now instead of scanning the probe beam, the pump beam was scanned while the probe beam was kept at the same frequency during the scan. The absorption signal of the probe beam is then recorded as function of the pump beam scan time. Simultaneously, the pump beam frequency is recorded and also related to the scanning time of the pump beam. A trigger output signal of the pump laser makes sure the pump

Acetylene transition (normal mode notation)	J (upper state)	Branch	Transition frequency ( $\text{cm}^{-1}$ )	Laser
0000 <sup>0</sup> 0 <sup>0</sup> → 0010 <sup>0</sup> 0 <sup>0</sup>	J=6 → J'=7	R	3311.067487	pump
0000 <sup>0</sup> 0 <sup>0</sup> → 0010 <sup>0</sup> 0 <sup>0</sup>	J=7 → J'=8	R	3313.348542	pump
0000 <sup>0</sup> 0 <sup>0</sup> → 0010 <sup>0</sup> 0 <sup>0</sup>	J=8 → J'=9	R	3315.619792	pump
0000 <sup>0</sup> 0 <sup>0</sup> → 0010 <sup>0</sup> 0 <sup>0</sup>	J=9 → J'=10	R	3317.880408	pump
0000 <sup>0</sup> 0 <sup>0</sup> → 0010 <sup>0</sup> 0 <sup>0</sup>	J=10 → J'=11	R	3320.130748	pump
0000 <sup>0</sup> 0 <sup>0</sup> → 0010 <sup>0</sup> 0 <sup>0</sup>	J=11 → J'=12	R	3322.36971	pump
0000 <sup>0</sup> 0 <sup>0</sup> → 0010 <sup>0</sup> 0 <sup>0</sup>	J=12 → J'=13	R	3324.596916	pump
0000 <sup>0</sup> 0 <sup>0</sup> → 0010 <sup>0</sup> 0 <sup>0</sup>	J=13 → J'=14	R	3326.812475	pump
0000 <sup>0</sup> 0 <sup>0</sup> → 0010 <sup>0</sup> 0 <sup>0</sup>	J=14 → J'=15	R	3329.015606	pump
0010 <sup>0</sup> 0 <sup>0</sup> → 2010 <sup>0</sup> 0 <sup>0</sup>	J'=7 → J''=6	P	6351.537	probe
0010 <sup>0</sup> 0 <sup>0</sup> → 2010 <sup>0</sup> 0 <sup>0</sup>	J'=8 → J''=7	P	6348.996	probe
0010 <sup>0</sup> 0 <sup>0</sup> → 2010 <sup>0</sup> 0 <sup>0</sup>	J'=9 → J''=8	P	6346.427	probe
0010 <sup>0</sup> 0 <sup>0</sup> → 2010 <sup>0</sup> 0 <sup>0</sup>	J'=10 → J''=9	P	6343.831	probe
0010 <sup>0</sup> 0 <sup>0</sup> → 2010 <sup>0</sup> 0 <sup>0</sup>	J'=11 → J''=10	P	6341.209	probe
0010 <sup>0</sup> 0 <sup>0</sup> → 2010 <sup>0</sup> 0 <sup>0</sup>	J'=12 → J''=11	P	6338.56	probe
0010 <sup>0</sup> 0 <sup>0</sup> → 2010 <sup>0</sup> 0 <sup>0</sup>	J'=13 → J''=12	P	6335.886	probe
0010 <sup>0</sup> 0 <sup>0</sup> → 2010 <sup>0</sup> 0 <sup>0</sup>	J'=14 → J''=13	P	6333.186	probe
0010 <sup>0</sup> 0 <sup>0</sup> → 2010 <sup>0</sup> 0 <sup>0</sup>	J'=15 → J''=14	P	6330.461	probe
0010 <sup>0</sup> 0 <sup>0</sup> → 2010 <sup>0</sup> 0 <sup>0</sup>	J'=7 → J''=8	R	6386.273	probe
0010 <sup>0</sup> 0 <sup>0</sup> → 2010 <sup>0</sup> 0 <sup>0</sup>	J'=8 → J''=9	R	6388.361	probe
0010 <sup>0</sup> 0 <sup>0</sup> → 2010 <sup>0</sup> 0 <sup>0</sup>	J'=9 → J''=10	R	6390.421	probe
0010 <sup>0</sup> 0 <sup>0</sup> → 2010 <sup>0</sup> 0 <sup>0</sup>	J'=10 → J''=11	R	6392.453	probe
0010 <sup>0</sup> 0 <sup>0</sup> → 2010 <sup>0</sup> 0 <sup>0</sup>	J'=11 → J''=12	R	6394.458	probe
0010 <sup>0</sup> 0 <sup>0</sup> → 2010 <sup>0</sup> 0 <sup>0</sup>	J'=12 → J''=13	R	6396.435	probe
0010 <sup>0</sup> 0 <sup>0</sup> → 2010 <sup>0</sup> 0 <sup>0</sup>	J'=13 → J''=14	R	6388.386	probe
0010 <sup>0</sup> 0 <sup>0</sup> → 2010 <sup>0</sup> 0 <sup>0</sup>	J'=14 → J''=15	R	6400.31	probe
0010 <sup>0</sup> 0 <sup>0</sup> → 2010 <sup>0</sup> 0 <sup>0</sup>	J'=15 → J''=16	R	6402.208	probe

**Table 3.2:** Transition frequencies of acetylene for both the first excitation with the OPO (pump) laser and the second step by the Ti:Sapph (probe) laser.  $J$  represents the rotational angular momentum, R-branch refers to  $\Delta J = J' - J = 1$  and P-branch to  $\Delta J = -1$ . Transition frequencies are obtained from HITRAN<sup>33</sup>.

beam frequency can be related to the absorption signal afterwards. This results in a plot of the absorption signal as function of the pump beam frequency. Since the probe beam frequency is constant for each plot, several plots are made for different probe beam frequencies. The result of a single scan, zoomed in to the RDT dip, is shown in Figure 3.9, where the ECDL was kept at a frequency of  $6392.392 \text{ cm}^{-1}$  and the pump beam scanning rate was  $0.001 \text{ cm}^{-1}/s$ .

Now it becomes clear that the earlier observed dip consists of two distinct peaks, comparable in both height and width. The fact that there are two dips instead of one is explained by the direction of the pump and probe laser beams and the associated Doppler shift. This can be understood with Figures 3.10 and

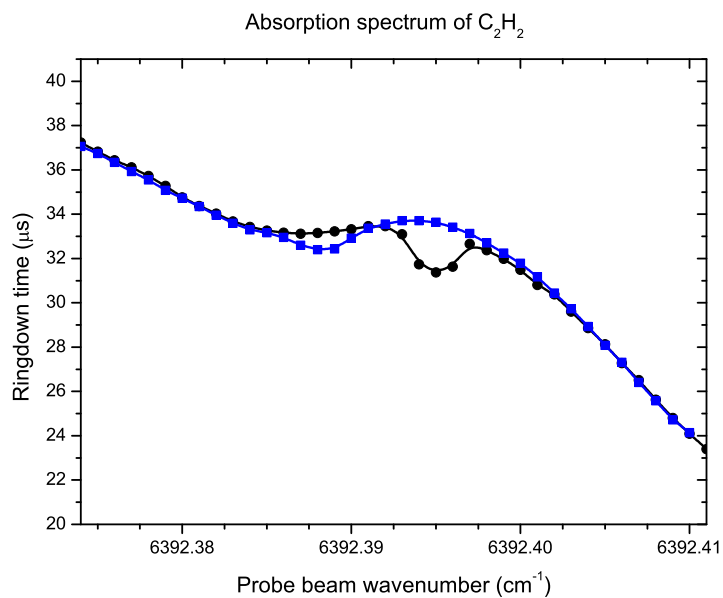


**Figure 3.8:** Acetylene absorption spectrum obtained by scanning the probe beam. Black circles: scan with pump beam present. Blue squares: scan with pump beam turned off. Both datasets are interpolated with a B-spline curve. Acetylene pressure in the sample cell is 1.1 mbar and the pump beam is tuned to  $3317.87\text{ cm}^{-1}$ .

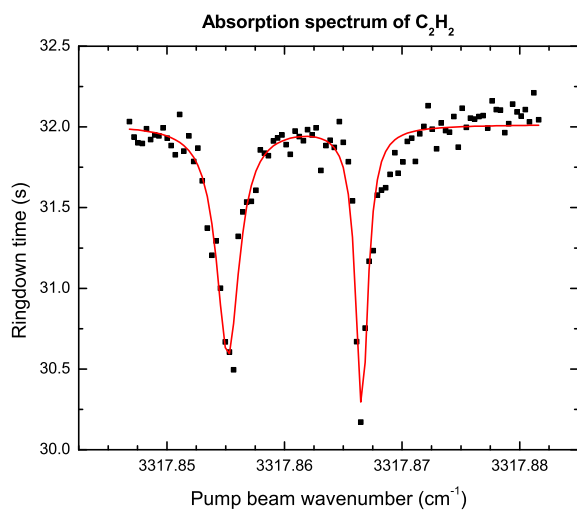


**Figure 3.9:** Acetylene spectrum obtained by scanning the pump beam, with probe beam frequency  $6392.392\text{ cm}^{-1}$ . The red curve is the sum of two Lorentzians fitted to the two peaks, centered at  $3317.8552$  and  $3317.8666\text{ cm}^{-1}$ .

3.11, where the population of the three energy levels of interest is schematically depicted as function of the molecular velocity component in the laser beam direction. In Figure 3.10 the probe beam is tuned exactly to the resonance between the two upper levels, while the pump beam is scanned across the lower resonance. With the pump beam tuned below resonance, molecules moving towards the laser beam with speed  $v$  matching the Doppler shift  $\Delta\omega_{pump}/k$  will still be excited to  $|e_1\rangle$ , known as Doppler broadening of the resonance. These molecules are however not excited to  $|e_2\rangle$  because the probe laser is only resonant with zero speed molecules. So only when pump beam is scanning across the center of the resonance, the probe beam excites molecules to  $|e_2\rangle$ . The obtained absorption spectra are free of Doppler broadening, therefore resolving more spectral features.

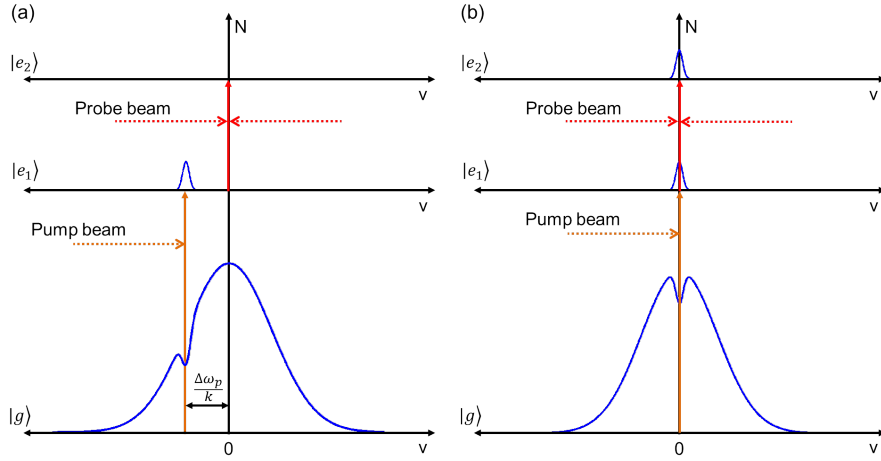


**Figure 3.10:** Schematic drawing of the level population  $N$  of the ground state  $|g\rangle$ , first excited state  $|e_1\rangle$  and second excited state  $|e_2\rangle$  as function of molecule velocity  $v$  directed along the laser beam. The probe beam frequency is fixed exactly at the  $|e_1\rangle \rightarrow |e_2\rangle$  transition, while the pump beam is scanned across the  $|g\rangle \rightarrow |e_1\rangle$  transition. (a) With the pump beam off-resonance  $|e_1\rangle$  is still populated due to Doppler broadening, while the probe beam does not excite molecules having nonzero velocity. (b) If the pump beam hits the exact resonance, the probe beam excites  $v = 0$  molecules from  $|e_1\rangle$  to  $|e_2\rangle$  and a Doppler-free absorption spectrum is obtained.

When the probe beam is slightly detuned from the upper resonance it excites molecules in  $|e_1\rangle$  with a velocity  $v = \Delta\omega_{probe}/k'$ , as shown in Figure 3.11. So when the detuning of the pump beam matches the detuning of the probe beam, both are in resonance and an absorption peak will be visible. However, because the probe beam is reflected back and forth between the cavity mirrors, the probe beam part traveling in the opposite direction of the pump beam is resonant with the  $|e_1\rangle$  molecules having a velocity  $v = \Delta\omega_{pump}/k = \Delta\omega_{probe}/k'$  in the pump beam direction. This is where the second absorption peak arises. When the pump beam detuning does not match the probe beam detuning, for instance when it is exactly on resonance, no absorption of the probe beam occurs. In conclusion, because of the Doppler shift and the counter propagating probe beam, two similar peaks centered around the central resonance will be visible

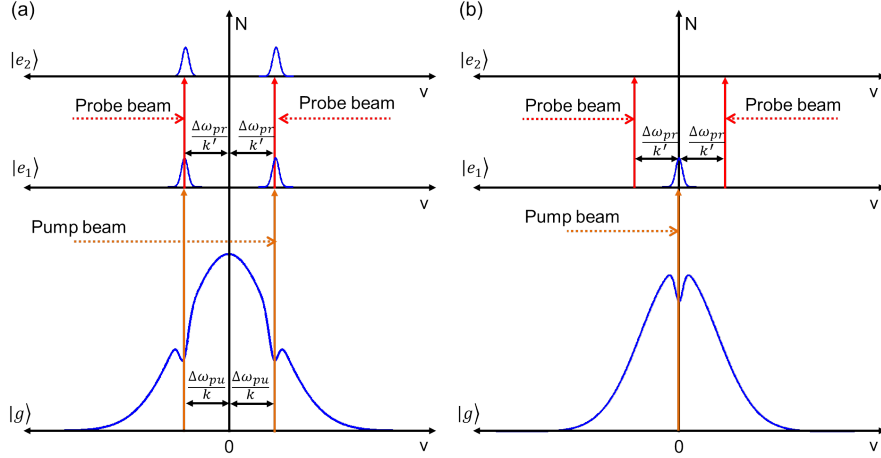


**Figure 3.11:** Schematic drawing of the level population  $N$  of the ground state  $|g\rangle$ , first excited state  $|e_1\rangle$  and second excited state  $|e_2\rangle$  as function of molecule velocity  $v$  directed along the laser beam. The probe beam frequency is detuned with  $\Delta\omega_{probe}/k'$  from the  $|e_1\rangle \rightarrow |e_2\rangle$  transition, while the pump beam is scanned across the  $|g\rangle \rightarrow |e_1\rangle$  transition. (a) When the probe beam detuning matches the pump beam detuning,  $|e_2\rangle$  is populated. Because the probe beam travels in two directions, this happens both for a positive and negative pump beam detuning, centered around the resonance frequency. (b) If the pump beam hits the exact resonance, no absorption peak is visible because the detuned probe beam is not in resonance with the zero velocity  $|e_1\rangle$  molecules.

when the probe beam is slightly detuned.

From this analysis it is clear that in Figure 3.9 the probe beam was detuned from the  $|e_1\rangle \rightarrow |e_2\rangle$  transition. Therefore several different scans were made while varying the frequency of the probe beam, they are shown in Appendix B. All peaks are fitted by Lorentzian curves, because the line shapes are dominated by pressure and lifetime broadening since the reflected probe beam ensures a Doppler-free signal. The fit parameters can also be found in Appendix B. All scans are plotted together in Figure 3.12. There the offset of the pump beam wavenumbers has been adjusted for each scan to match the central resonance frequency, which is for each scan exactly in the middle of the two peaks. The discrepancy in the  $|g\rangle \rightarrow |e_1\rangle$  wavenumber for the different scans is probably caused by an error in the synchronization of the frequency data from the wavemeter with the RDT data and has a standard deviation of  $0.0012 \text{ cm}^{-1}$ .

The dips of the different scans in Figure 3.12 behave as expected; when the probe beam detuning approaches towards zero, the peaks move closer towards each other, until they overlap and form a single dip when  $\Delta\omega_{probe} = 0$ . This is at the point where both pump and probe beam are exactly on resonance. The frequency shift of the two symmetric dips in the probe beam from the center resonance frequency can be calculated from the detuning of the probe beam by

$$\Delta\omega_{pump} = \Delta\omega_{probe} \frac{k}{k'} = \Delta\omega_{probe} \frac{\omega_{pump}}{\omega_{probe}} = 0.52\Delta\omega_{probe}. \quad (3.1)$$

As is indicated in Figure 3.11. The values of  $\Delta\omega_{pump}$  are calculated in Table

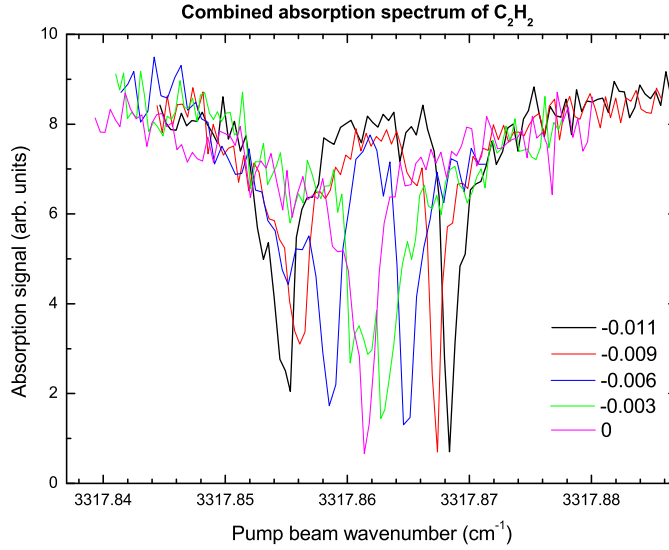


**Figure 3.12:** Acetylene spectrum of multiple pump beam scans, with different probe beam detunings (colours, values in  $\text{cm}^{-1}$ ) from the resonance at  $6392.403 \text{ cm}^{-1}$ . The pump beam wavenumber offset has been adjusted for each scan to correct for the offset from the averaged center of resonance, as in Table B.1.

Figure	3.9	B.1	B.2	B.3	B.4
ECDL detuning	-0.011	-0.009	-0.006	-0.003	0
Left peak width	0.00235	0.0031	0.00641	0.00742	0.00294
Right peak width	0.00128	0.00119	0.00157	-	-
Offset from averaged center resonance	-0.0006	0.0014	0.0002	-0.0018	0.0008
$0.52\Delta\omega_{probe}$	0.0057	0.0047	0.0031	0.0016	0
Half of peak difference	0.0057	0.00490	0.00345	-	-

**Table 3.3:** Parameters extracted from the Lorentzian fits of the absorption spectra of  $\text{C}_2\text{H}_2$ , all values are in  $\text{cm}^{-1}$ .

3.3 and can then be compared with shift of the symmetric dips in Figure 3.12. These values are indicated in the last row of Table 3.3 and they match the calculated values within 10%. This means the position of the symmetric pairs of dips in Figure 3.12 can be very well explained by the Doppler shift between the pump and the probe beam inside the sample cell.

One would expect the dip size to increase by a factor 2 at zero probe beam detuning because the signal of both counter propagating parts of the probe beams then adds up. However, this effect is not clear from the figure, which could either be caused by the fact that the probe beam was actually not exactly on resonance. Or the power of the pump beam limited the number of molecules in  $|e_1\rangle$  and therefore also limited the size of the absorption dip. From the figure

and the fit parameters in Table 3.3 one sees the width and size of the two dips of the individual scans are not always similar. Deviations of this kind could be caused by fluctuations in the scan rate resulting in a non-linearity in the scan, or by some other effect of the experimental arrangement.

Finally, the  $0000^0_0 \rightarrow 0010^0_0$  and  $0010^0_0 \rightarrow 2010^0_0$  measured transition frequencies are given in Table 3.4. The obtained values are close to the reference values from HITRAN and earlier measured ones, but still deviate  $\sim 0.04 \text{ cm}^{-1}$  which is significantly more than the error indicates. A possible explanation for this is that the wavelength meter was not calibrated carefully for the measurements due to a lack of time. Furthermore, some yet unknown systematic effect in the experimental setup could have caused the shift in frequency.

Transition (normal mode notation)	$0000^0_0 \rightarrow 0010^0_0$	$0010^0_0 \rightarrow 2010^0_0$
J (upper state)	10	10
Branch	R	R
Measured frequency ( $\text{cm}^{-1}$ )	$3317.8615 \pm 0.002$	$6392.403 \pm 0.003$
Reference frequency <sup>33</sup> ( $\text{cm}^{-1}$ )	3317.880408	6392.453
Experimental frequency <sup>34</sup> ( $\text{cm}^{-1}$ )	3317.880389	

**Table 3.4:** Summary of measured, reference and earlier experimental values for the pump and probe beam frequencies.

### 3.4 Conclusion

In this chapter a new method was used pursuing the measurement of higher overtones of acetylene. The technique of two photon excitation combined with CRDS is never demonstrated before and therefore first it was tried to measure a molecule with very well-known transitions,  $\text{H}_2^{18}\text{O}$ , before moving on to overtones of acetylene, for which no experimental data exists yet. Because this did not produce satisfying results small changes in the setup were made, moving towards the infrared regime of lower overtones of acetylene and therefore gaining several orders of magnitude in line strength. The expected absorption lines of the  $0000^0_0 \rightarrow 0010^0_0$  and  $0010^0_0 \rightarrow 2010^0_0$  transitions were measured at  $3317.8615 \pm 0.002$  and  $6392.403 \pm 0.003 \text{ cm}^{-1}$  respectively. With a signal to noise ratio close to 10 the spectra show clearly resolved peaks free from Doppler broadening. The obtained frequencies differ from the literature values by  $\sim 0.04 \text{ cm}^{-1}$  which is probably due to some systematic error in the experimental arrangement. So far no time has been spend trying to find the experimental source of the error.

With these results, the two photon excitation technique has proven to work as a new method to perform high sensitivity molecular spectroscopy in the infrared and visible regime. Continuing work should include performing more measurements and further optimizing the setup. Probably this will improve the signal quality significantly and increase the sensitivity, because so far very few efforts were made optimizing the signal. With this done, it should be possible to measure the never observed higher overtones of acetylene using this new method.

## Chapter 4

# Dipole trapping of cold molecules

In this chapter the experimental realization of an optical dipole trap is investigated. First, the requirements of our optical trap are formulated, mainly dictated by the goal of our experiment: the measurement of parity violation. In the second section these requirements are transferred into parameters for an optical dipole trap and the laser source. Subsequently, an experimental setup is designed to realize the ODT and its most important aspects are discussed. In the next section, a literature study is carried out to improve the loading of the ODT, resulting in the idea of a single photon transition scheme, whereof the different aspects are investigated. In the fifth part of this chapter the building of an experimental setup is reported, together with the first results. The chapter ends with the main conclusions of the preceding sections and an outlook of the experiment.

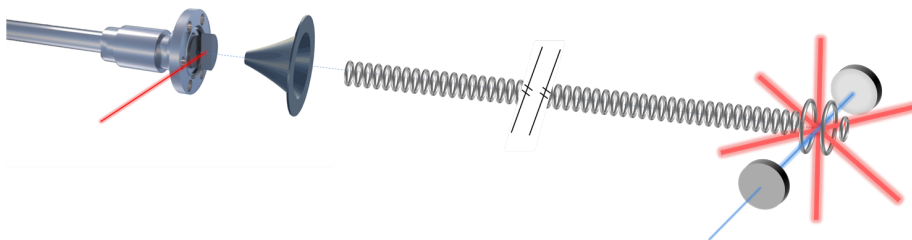


**Figure 4.1:** Schematic overview of the experimental setup. The molecules are ablated from a solid SrF<sub>2</sub> pill by a laser. A carrier gas, expanding adiabatically in the vacuum, takes the molecules through a skimmer, which selects only molecules with low transverse velocity, into the Stark decelerator. Alternating high voltages on the ring-shaped electrodes slow down the *lfs* SrF molecules, ending up in a static electric trap in the middle of the two larger electrodes at the end of the decelerator. At this position the molecules are laser cooled (indicated by the red laser beams) and captured in a dipole trap (indicated in blue), where the final parity violation measurements are performed.

## 4.1 Trap requirements

The goal of the Cold Molecule experiment is to perform high precision measurements on ultra-cold molecules. To retrieve a sample of cold molecules, they are first slowed down and subsequently laser cooled below mK temperatures, as shown schematically in Figure 4.1. In order to measure the transition strength between two states, the molecules need to be kept in some sort of trap during the time of the measurement. Therefore we aim for a trap lifetime of  $\sim 1$  s. During the Stark deceleration stage, all molecules are in the low field seeking state (lfs). However, in the subsequent laser cooling process some of them will decay into high field seeking states (hfs) and different rovibrational states. To not lose these molecules in the final trapping stage, they should also be captured in the trap. Furthermore, the trap depth should be such that the laser cooled molecules are strongly confined in the trap. After laser cooling, the temperature is estimated to be  $\sim 150 \mu\text{K}$ , but since recent developments<sup>35</sup> suggest this temperature might be hard to reach in practice, we aim for a trap depth of at least 1 mK. Prior to the laser cooling stage, the molecules are captured in a static electric trap and after laser cooling the estimated size of the SrF cloud is  $1 \text{ mm}^2$ . To capture a sufficient fraction of molecules in the trap, its volume should be significant in comparison with the SrF cloud. As an experimentally achievable goal we therefore set the minimum trap volume at 5% of the initial cloud volume.

In summary, the requirements for the final trapping stage of SrF are:

- Trapping lifetime  $\sim 1$  s
- Trap depth  $> 1$  mK
- Trap volume  $> 0.05 \text{ mm}^2$
- Confinement of lfs, hfs as well as different rovibrational states

The first three requirements can be fulfilled by several different trap types, such as a magneto-optical trap (MOT) or optical dipole trap (ODT). The last requirement is however not easily achieved by the different traps. A MOT for instance, relies on optical transitions induced by near resonant laser beams. To trap different states at the same time, one would need an additional laser frequency for each state. Apart from the complicated laser system, the different frequencies would also cause molecules in close-lying blue detuned states to be heated out of the trap. Therefore a MOT is not suitable as our final trapping stage. An ODT however, does not have this disadvantage because it is based on the optical dipole force rather than individual resonant optical transitions. Because the dipole force induces an energy shift in all rovibrational states of the molecule, an ODT can trap all these states using a single, off-resonant laser beam. With an ODT it is in fact harder to reach the required trap depth and volume because the force that the molecules experience is rather small and depends on their polarizability. However, the trap can be made as large and deep as necessary by using sufficient laser power. The trap lifetime of an ODT depends critically on the stability of the trapping laser and will be discussed later on, but lifetimes of several seconds are possible.

## 4.2 Design of an optical dipole trap

Because of the molecular structure of SrF, lots of rovibrational sub-states exist within every electronic state. An energy level diagram of the molecule of the ground state and first excited electronic states is shown in Figure 4.2, where the bands with rovibrational states are in the white areas, and in the shaded areas no states exist. The latter frequency regions would therefore be suitable for dipole trapping. Because only the ground state and first excited state are of interest to us and we want to use red-detuned light to create a trap at the focus of a laser beam, the trapping wavelength should be in the lower shaded area, as explained in section 2.4.2. At 1064 nm powerful lasers and a lot of optics are available, therefore we choose this wavelength for the dipole trap. With the resulting large amount of detuning from the X-A electronic transition we create a QUEST, where the molecules experience effectively a static potential.

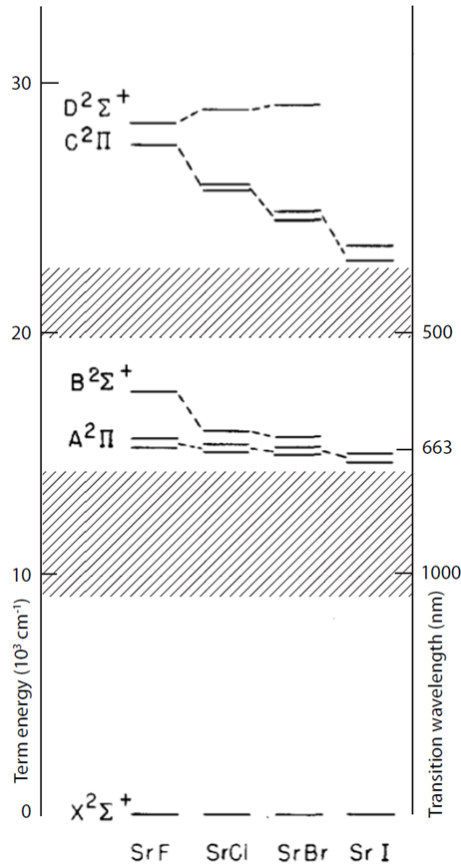


**Figure 4.2:** Energy level diagram of the ground state and first four electronically excited states of SrF and a few other alkaline-earth mono-halides. The shaded areas indicate the energy regimes wherein no rovibrational transitions exist and which are thus suitable as dipole trapping wavelengths. (Figure from ref. 36)

To calculate the laser power needed for the required trap depth of 1 mK we use (2.61). Here we also need the ground state polarizability of SrF, which has

been calculated to be  $\alpha_{SrF} = 11.6 \text{ \AA}^3$ , where polarizability volume units are used. As a first estimation we set the waist of the laser beam focus, which is the small radius of the cigar-shaped trap, at  $100 \mu\text{m}$ . This results in a required laser power of

$$P_0 = \frac{cw_0^2}{4\alpha_{SrF}} \frac{U_{ODT}[\text{mK}]}{k} \approx 900\text{W}, \quad (4.1)$$

where  $k$  is the Boltzmann constant, put in to convert the trap depth in mK to energy. From this first estimation we learn that we need a large amount of laser power in the focus. Using just a single focused beam as a trap, one would need a very powerful laser, which is both hard to handle and expensive. A relatively easy way to obtain enough trapping power is the use of an enhancement cavity where the constructive interference of a large number of round-trips can enhance the laser power by several orders of magnitude.

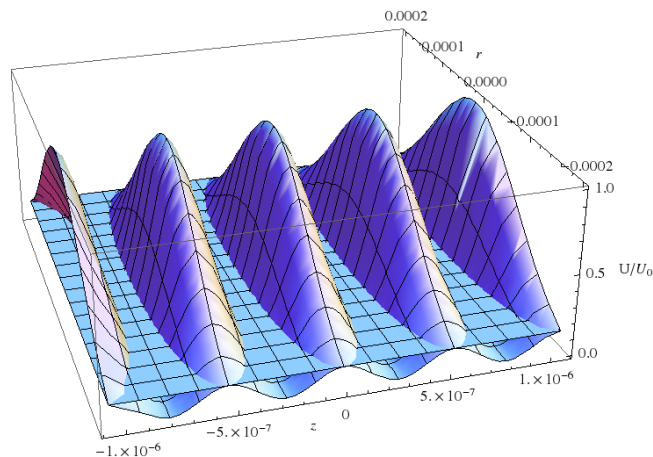


**Figure 4.3:** Dipole potential for a 1-D optical lattice with trapping wavelength  $\lambda=1064$  and beam waist  $w_0 = 200\mu\text{m}$ . The flat plain indicates the  $r,z$  interface where the potential has dropped to  $1/e^2$  of its maximum value.

When using the focus of an enhancement cavity as optical trapping region the trap is no longer cigar-shaped, but consists of a sequence of many flat traps as in a 1-D lattice, as described in section 2.4.3. The total volume of the lattice traps is thus smaller than that of single focus dipole trap with the same beam parameters. This is illustrated in Figure 4.3, where the potential of a 1-D lattice with  $\lambda=1064$  and beam waist  $w_0 = 200\mu\text{m}$  is plotted. The volume of a 1-D lattice can be calculated using the lattice potential from (2.62) and is approximately given by:

$$V_{lat} = N * \frac{\pi}{4} \lambda w_0^2, \quad (4.2)$$

where  $N$  is the number of traps overlapping with the molecular cloud.  $V_{lat}$  is calculated for different waist sizes in Table 4.1, assuming the dipole trap to traverse a molecular cloud with a diameter of  $1 \text{ mm}^3$ . In the table also the corresponding trap depths are indicated, calculated with (2.61) and (2.62). However, in the calculation of the trap depths some uncertainty is involved. To be on the safe side, we therefore aim for a trap depth of  $> 4 \text{ mK}$ . Together with

the trap volume requirement of  $V_{lat} > 0.05 \text{ mm}^3$ , this leads to a required laser power of  $>4 \text{ kW}$ , indicated in bold in the table.

Beam waist( $\mu\text{m}$ )	500W	1000W	2000W	<b>4000W</b>	Trap volume( $\text{mm}^3$ )
50	9	18	36	72	0.004
100	2	4	9	18	0.016
<b>200</b>	0,5	1	2	<b>4</b>	<b>0.07</b>
300	0.2	0.5	1	2	0.14

**Table 4.1:** Calculated dipole trap depths in mK and volumes for different values of laser power and trapping beam waist. The bold numbers indicate the parameters we have chosen for our dipole trap.

### 4.2.1 Enhancement cavity design

Commercial lasers in the range of few tens of Watts are widely available and affordable. To reach  $\sim 4 \text{ kW}$  at our optical trapping region the optical cavity therefore needs to enhance the laser light by a factor of  $\sim 400$ . To easily achieve this we choose mirror reflectivities  $R \geq 0.998$ . Because our cavity will operate in the vacuum, and the wavelength is far detuned from any resonance of the molecules, we have very low losses inside the cavity and therefore the mode matching condition in (2.56) indicates both mirror reflectivities should be equal. For the mirror placement we choose the confocal configuration, because it is intrinsically stable and has a large waist. We can use Figure 2.8 to select the radii of curvature of the mirrors and the cavity length. We aim for a waist size of  $200 \mu\text{m}$  and because of limited space in the vacuum we are bound to left side of the waist size parabola's. In terms of stability it is convenient to be close to the confocal condition, but not exactly because then all TEM modes of the cavity overlap and it is hard to sustain only the TEM<sub>00</sub> mode. Therefore we want to be slightly off the confocal condition. When we select a cavity length of  $16 \text{ cm}$  and ROC of  $25 \text{ cm}$ , we are close to the confocal condition and obtain a waist of  $200 \mu\text{m}$ . Also, once implemented we can still change to higher ROC to increase the waist size, or towards smaller ROC to decrease the waist, while still avoiding the confocal condition.

In conclusion, the parameters we choose for the enhancement cavity are summarized in Table 4.2.

Waist	$w_0 = 200\mu\text{m}$	Mirror reflectivity	$R = 0.998$
Trap volume	$V = 0.07\text{mm}^3$	Radius of curvature	$ROC = 0.25\text{m}$
Wavelength	$\lambda = 1064\text{nm}$	Cavity length	$d = 0.18\text{m}$
Trap depth	$U_0 = 11\text{mK}$	Free spectral range	$v_{FSR} \cong 800\text{MHz}$
Enhancement	$A = 500$	Linewidth	$\Delta v_{cav} \cong 530\text{kHz}$
Intracavity power	$P_{cav} = 10\text{kW}$	Finesse	$\mathcal{F} \cong 1600$

**Table 4.2:** Parameters of the enhancement cavity designed for operating a dipole trap which meets the requirements set in section 4.1.

## 4.2.2 Laser requirements

The laser producing the light for the dipole trap has to meet several requirements. As discussed in the previous section, the laser should have  $\sim 20$  W of power at a wavelength of 1064 nm. In order to couple all the light in the cavity, the linewidth of the laser should be equal or smaller than the linewidth of the cavity. Therefore the linewidth of the laser should be smaller than 530 kHz. In section 2.3.2 it was explained the laser should have a sufficient coherence length, depending on the cavity length and Finesse. This statements can be easily rewritten into a boundary on the linewidth of the laser:

$$\Delta v_{las,mean} \leq \frac{\pi c}{d\mathcal{F}} = 3.3MHz \quad (4.3)$$

However, this calculation was done for the mean time a photon stays inside the cavity. When we reduce this linewidth to<sup>22</sup>

$$\Delta v_{las} \leq \log(0.0005\Delta v_{las,mean}) \cong 440kHz, \quad (4.4)$$

only 0,05% of the photons are left inside the cavity after a time equal to the coherence time of the laser. This means that the vast majority of photons contributes to the standing wave inside the cavity and losses due to incoherent photons are negligible when the linewidth of the laser is smaller than 440 kHz. This is a slightly stricter boundary than the 530 kHz arising from the cavity linewidth.

Other prerequisites for the laser arise from the requirement that the lifetime of the trap should be  $> 1$  s. Molecules can be heated out of the trap very easily when the trap shakes with twice the frequency with which the molecules oscillate in the trap. This shaking of the trap takes place when the laser power coupled into the cavity fluctuates. Therefore the intensity of the laser should have very low noise at twice the trap frequencies<sup>38</sup>. The trap frequencies are calculated by (2.63) and (2.64):

$$f_{axial} = \frac{\omega_{axial}}{2\pi} \cong 1.2MHz \quad (4.5)$$

$$f_{radial} = \frac{\omega_{radial}}{2\pi} \cong 1.5kHz \quad (4.6)$$

In<sup>22</sup> and<sup>39</sup> it is described how to calculate the maximum amount of noise allowing for a trap lifetime of 1 second. Following a similar calculation, we obtain for our trap:

$$S_k(2f_{axial}) \leq 10 \log_{10}\left(\frac{\Gamma_x}{\pi^2 f_{axial}^2}\right) = -127dB/Hz \quad (4.7)$$

$$S_k(2f_{radial}) \leq 10 \log_{10}\left(\frac{\Gamma_r}{\pi^2 f_{radial}^2}\right) = -69dB/Hz \quad (4.8)$$

$S_k$  stands for a one sided power spectrum, as a measure of the relative intensity noise (RIN) in a logarithmic scale.  $\Gamma_x$  and  $\Gamma_r$  are the axial and radial heating rates, respectively, which are set by the required trap lifetime. So the intensity noise of the laser should be below -127 dB/Hz at a frequency of 1.2 MHz and below -69 dB/Hz at 1.5kHz.

Wavelength	$\lambda = 1064\text{nm}$
Power	$P_0 \geq 20W$
Linewidth	$\Delta\nu_{las} \leq 440\text{ kHz}$
RIN at 1.2 MHz	$S_k \leq -127\text{dB}/Hz$
RIN at 1.5 kHz	$S_k \leq -69\text{dB}/Hz$

**Table 4.3:** Requirements of the laser needed to feed an enhancement cavity and create a trapping potential stable enough for trapping SrF molecules.

The requirements for the laser are summarized in Table 4.3.

Considering all the above requirements, we decided to buy the Mephisto MOPA 42W laser from the company Coherent. This laser has proven itself suitable for optical lattices<sup>38</sup> and no commercially available alternatives are meeting the above requirements.

## 4.3 Experimental setup

To come up with a design for the experimental setup for the dipole trap we looked at several dipole traps reported in literature<sup>27;28;40;41;38;42</sup>. All of these traps are designed for atoms, but since molecules experience a similar potential in a dipole trap we can still learn from the techniques used in atom traps and choose which ones are most applicable to our system.

### 4.3.1 Trapping region

In Figure 4.4 a schematic overview of the trapping region is shown. At the end of the decelerator the molecules are caught in a static electric trap where the laser cooling takes place. The dipole trap has to be superimposed on this electric trap, so the focus of the enhancement cavity must overlap the electric trap. The design of the electrodes for the electric trap by Corine Meinema is such that there is maximum optical access, both for the laser cooling beams and for the trapping beam. To minimize collisional losses by background gasses the trapping region needs to be at ultra high vacuum (UHV) pressure ( $\sim 10^{-13}$  mbar). Although it is possible to place the mirrors of the enhancement cavity outside the vacuum with the advantage of easy control, as was done in some other experiments<sup>38;27</sup>, we choose to place the whole cavity inside the vacuum. This is mainly because we need a large enhancement and very high power inside the cavity and having view-ports in between the cavity mirrors would introduce significant intra-cavity losses, which strongly limit the power enhancement. Furthermore, the view-ports would have to withstand the very high power inside the cavity without getting damaged, which not impossible, although it would be quite challenging to find suitable view-ports for this.

### 4.3.2 Dipole trap stability

One of the disadvantages of using a cavity to create the dipole trap is that the trap becomes very sensitive to fluctuations in the laser frequency and intensity. Not only the linewidth of the laser, as discussed in section 4.2.2, but also the frequency has to exactly match the cavity to obtain a large enhancement, as

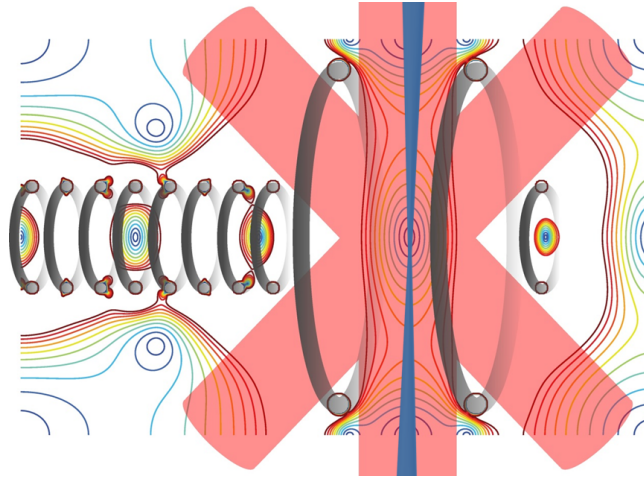


**Figure 4.4:** Schematic overview of the trapping region at the end of the decelerator. The colored lines are equipotentials where the electric field is constant. The smaller rings are the last few electrodes of the decelerator, the two big rings create the static electric trap in where the molecules are trapped and laser cooled by the red beams. The dipole trap is indicated in blue (not to scale) and is superimposed on the electric trap. (Figure adapted from ref. 13)

explained in section 2.3.1. The latter can be done in two general ways; either locking the laser frequency to a cavity resonance or locking the cavity length to the laser frequency. Because locking the cavity to the laser is most commonly used and the laser we ordered is quite stable, we choose to modulate the length of our cavity to match the frequency of the laser. Note that the dipole trap potential itself is not sensitive to minor changes in the frequency; it is only the cavity that needs to be exactly on resonance. However, if it still turns out to be necessary it would be relatively easy to implement an extra frequency reference at the laser table to keep our laser frequency precisely fixed.

To perform certain types of measurements, like time of flight, and also to improve the loading on the dipole trap<sup>28</sup>, it is very useful to have dynamic control of the intensity of the dipole trap. This means we want to be able to switch the trap on and off quickly. However once the trap is switched off, the frequency lock of the cavity length is lost and the cavity will be out of resonance when the beam is turned on again. Conventional schemes use a flywheel circuit to 'remember' the drifts of the laser while the dipole trap is turned off (and thus unlocked), but these are limited in the turned off time and by drifts of the laser. In a recent paper by Edmunds and Barker<sup>28</sup>, a clever trick to circumvent this problem was presented. Their setup sends two beams through the cavity, one for locking the cavity to the laser frequency and the other one for creating the dipole trap. The beams are separated by using orthogonal polarizations, and hence the trapping beam can be switched off while the independent locking beam maintains the cavity lock at all times. Therefore we decided to base our setup on this scheme.

In Figure 4.5 an overview of the proposed laser setup for the dipole trap is shown. A high intensity trapping beam creates the dipole potential, while a small amount of light is split off, polarized exactly orthogonal and sent through

the enhancement cavity from the opposite side. This beam ensures stable locking of the cavity to the laser frequency at all times. The intensity of the trapping beam is stabilized using a second feedback loop with an acousto-optical modulator (AOM).

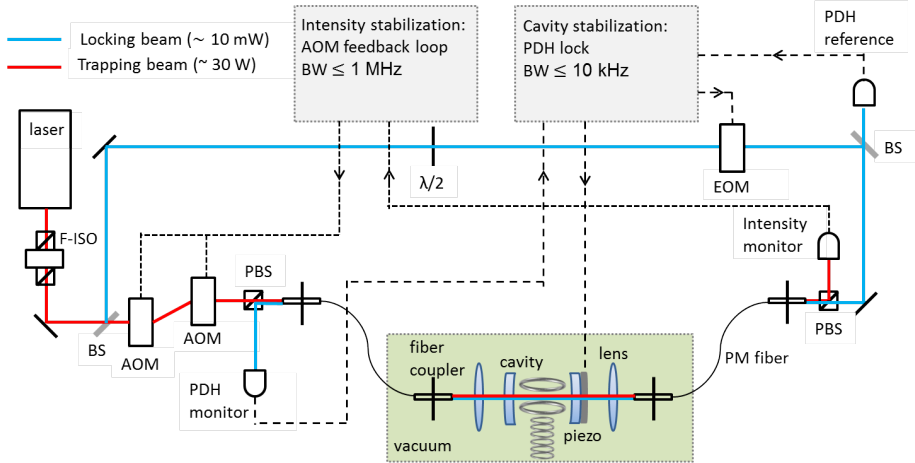


**Figure 4.5:** Schematic overview of the proposed laser setup for the dipole trap. The enhancement cavity is situated in the vacuum chamber (indicated in green), and is fed from both sides by two beams separated by orthogonal polarizations. The low intensity locking beam (blue) locks the cavity length to the laser frequency using a low bandwidth PDH locking scheme, while the high intensity beam (red) creates the dipole trapping potential and is intensity stabilized by a high bandwidth AOM feedback loop.

### 4.3.3 Pound-Drever-Hall lock

To make sure the cavity is in resonance with the laser frequency a piezo electric transducer is placed behind one of the mirrors to modify the length of the cavity. The thickness of the piezo is via an amplifier controlled by locking electronics and should follow the frequency of the laser to ensure the cavity is always on resonance. There are two locking schemes most widely used for locking resonance cavities, the Hänsch-Couillaud (HC) locking scheme<sup>43</sup>, and the Pound-Drever-Hall (PDH) locking scheme<sup>44;45</sup>. For HC-locking, a linear polarizer needs to be placed in the beam path inside the cavity. It is therefore complicated to combine this locking with the double beam setup, because the two beams have orthogonal polarization and those polarizations should not mix. Moreover, in the final experiment we want to be able to control the polarization of the trapping beam in order to increase the coherence time of the measurement<sup>46</sup>. Finally, we do not want optical elements inside our cavity since this limits the power build up, as mentioned in the previous section.

Therefore we choose to use the PDH locking scheme. This method uses the reflection from the front mirror of the cavity to generate a feedback signal, which drops to zero at a cavity resonance. An electro-optical modulator (EOM) is placed in the beam line to generate sidebands and by mixing the RF-signal input to the EOM with the feedback signal from the photodiode, an asymmetric error signal is obtained, with a zero crossing around the cavity resonance. This

signal is amplified and fed back to the piezo, which changes the length of the cavity accordingly to keep the error signal at zero.

#### 4.3.4 Intensity stabilization

As mentioned in section 4.2.2, it is very important to have very low noise in the intensity of the trapping beam, especially at twice the trap frequencies. We selected our laser to have very low RIN, but other sources, for instance vacuum pumps, can also induce noise in the system. The PDH lock removes most noise at frequencies  $< 10$  kHz, but to also get rid of higher frequency noise we can use an AOM feedback loop<sup>47</sup>. The intensity of the deflected output of the AOM is monitored and compared to a reference current. The difference is used to control the RF input power of the AOM. With a stable reference current, intensity noise is removed by the AOM. The bandwidth is limited to a few MHz by the response time of the AOM, originating from the relatively low speed of sound in the crystal. In our setup we need a second AOM to shift back the frequency of the intensity beam in order to match the frequency of the locking beam. This is important because only when their frequencies are exactly the same both beams are locked stably to the enhancement cavity. By changing the reference current in the AOM feedback loop we can rapidly change the intensity of the trapping beam and therefore control the depth of our dipole trap. This is a very useful feature, since it was reported that gradually increasing the intensity of the dipole trap, instead of turning it on instantly, can increase the number of trapped atoms by 50%<sup>28</sup>.

#### 4.3.5 Separating the beams

According to Edmunds and Barker<sup>28</sup>, it is very important to keep the locking and the trapping beams clearly separated: no light of the trapping beam may leak into the locking beam otherwise the PDH lock will be lost. Therefore polarization optics is used to separate both beams. A small fraction of the trapping beam is split off by a pellicle beam splitter (BS) and its polarization is changed exactly  $90^\circ$  by a half wave plate. Before entering and after leaving the vacuum, both beams are sent through two Glan Laser Calcite polarizing beam splitters (PBS) with an extinction ratio of 100 000:1. Because the locking beam has an exactly orthogonal polarization, it is fully transmitted through the first PBS and fully reflected by the second PBS, while for the trapping beam it is vice versa. The photodiodes for the intensity stabilization and the cavity lock are both placed behind the PBS, therefore making sure only light of the relevant beam is detected.

#### 4.3.6 Vacuum feed-through

A challenge is still to transport the beam into the vacuum. One could send the beam through vacuum windows, but those do often change the polarization a little bit, which is already enough to destroy the cavity lock. Furthermore this would require very precise stabilization of the mirrors outside the vacuum with the cavity inside the vacuum. A more convenient option is to send both beams through an optical fiber. In this way one would only need to stabilize the optical parts inside the vacuum, and vibrations on the laser table will not influence the

alignment of the cavity. The challenge here is to get the high power of the trapping beam through the fiber. The maximum power through an optical fiber is in general limited by a process called stimulated Brillouin scattering (SBS). Basically, when the power sent through an optical fiber reaches a certain threshold, an acoustic wave is induced in the fiber, which alters the refractive index of the fiber. The fluctuations in refractive index of the fiber scatter the initial light resulting in a reflected wave in opposite direction. Therefore, above the threshold, power of the incident light is lost into SBS and the output power of the fiber saturates. The threshold is inverse proportional to the length of the light<sup>48</sup>, so for short fibers the SBS threshold is higher. In our case, we can transport 20 W of power when using a fiber no longer than 5 m.

In order to keep the trapping and locking beam separate, also the fibers should strictly maintain the polarization of the overlapping beams. This is possible using polarization maintaining (PM) fibers, where the polarization along a fast and a slow axis, orthogonal to each other, is maintained throughout the fiber. To transport the high amount of power through the fiber, it needs to have a large mode field diameter, which is typically the case for photonic crystal fibers (PCF). This type of fibers have proven to be suitable for this application in other experiments as well<sup>49</sup>. We found suitable PM PCF with high power connectors from the company NKT Photonics.

## 4.4 Improving dipole trap loading

In order to perform a high precision measurement of transition strengths to detect parity violation, we need as many molecules as possible in the dipole trap. However, the estimated number of molecules in the preceding electric trap is only  $\sim 10000$ , and as is clear from Figure 4.4 the spatial overlap between the electric trap and the dipole trap is rather small. From Table 4.2 we read that the volume is  $0.07 \text{ mm}^3$ , which is  $\sim 7\%$  of the volume of the electric trap. Because the dipole potential is a conservative one and there is no dissipation inside the trap, only molecules initially located at the dipole trap position are trapped when the trap is turned on: molecules diffusing into the trap at later time will gain speed and also fly out of the trap again. To increase the number of trapped molecules I have therefore looked into ways to improve the loading of the ODT. In the following sections different possibilities are explored and the applicability to our setup is investigated.

### 4.4.1 Gray molasses

Gray molasses is a laser cooling technique for reaching sub-Doppler temperatures. It was first demonstrated in the mid 90's<sup>51;52</sup> by combining the velocity selective coherent population trapping (VSCPT) technique with the dissipative slowing force of a Sisyphus cooling scheme, as shown in Figure 4.6. The VSCPT pumps the atoms into a dark state which is decoupled from the light field and has a low momentum. The Sisyphus scheme ensures that atoms decaying into the bright state lose energy by climbing a potential hill, created by two counter-propagating light beams with opposite circular polarization, before being pumped back into the dark state. Using gray molasses cesium and rubidium atoms have been cooled below  $10 \mu\text{K}$ <sup>53</sup>.

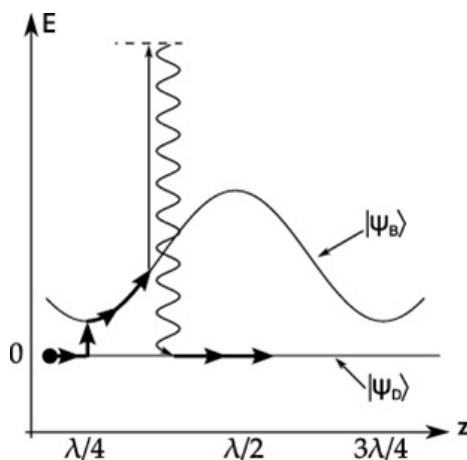


**Figure 4.6:** Cooling principle in gray molasses. When a  $F \rightarrow F' = F$  or  $F \rightarrow F' = F - 1$  optical transition is blue detuned, the ground state splits into a bright  $|\Psi_B\rangle$  and a dark  $|\Psi_D\rangle$  manifold. Adding a polarization gradient by using counter-propagating orthogonal circular polarizations causes energy shifts in the bright state. Motional coupling between  $|\Psi_B\rangle$  and  $|\Psi_D\rangle$  is maximal at the potential minima, therefore the particle has a higher probability of climbing the potential hill, and thus losing energy, before it decays back into the dark state, as in Sisyphus cooling. (Figure from ref. 50)

The forces of gray molasses are slowing forces, so no trapping can be achieved with gray molasses only. However, the gray molasses scheme can be used to improve the loading of an optical dipole trap<sup>55</sup>. The authors state that this is feasible because the molasses both decrease the temperature and increase the phase-space density. Meanwhile, the authors do not quantify how much the molasses improve the loading of the dipole trap, and when comparing the numbers it seems that they only trap 1% of the atoms from the molasses into the dipole trap. Besides this, the authors expect the dipole trapping laser not to disturb the molasses because the trapping laser does not change Raman detuning, which is critical for the gray molasses to work. The article however does not further underpin this statement either.

In general, it seems that the gray molasses technique does not compress the volume of a cloud of atoms, because it is only a slowing force. This conclusion is verified by several experiments<sup>50;56</sup>. However gray molasses could still be an interesting option for intra-trap cooling of particles, as earlier suggested, because very low temperatures can be reached. On top of that, the possibility of improved loading exist, however not yet proven.

Gray molasses have, to our knowledge, not been applied to molecules yet. To apply the gray molasses scheme, ones needs a  $\Lambda$ -type transition which for an electronic ground state is  $F \rightarrow F' = F$  or  $F \rightarrow F' = F - 1$  ( $F$  = total angular momentum). In our case of SrF, a transition in the the -almost- closed laser cooling scheme would be most suitable, which could be the transition from the  $F=2$  hyperfine level of the  $v=0, N=1 X^2\Sigma^+$  ground state to the  $F'=1$  hyperfine level of the  $v'=0, J'=1/2, A^2\Pi_{1/2}$  excited state, as shown in Figure 4.7. However, in the excited state the  $F'=1$  hyperfine level is not resolved from the  $F'=0$  level; the splitting between the two is less than 3 MHz. Therefore the  $\Lambda$ -scheme is possibly not fully working anymore, since a small splitting between

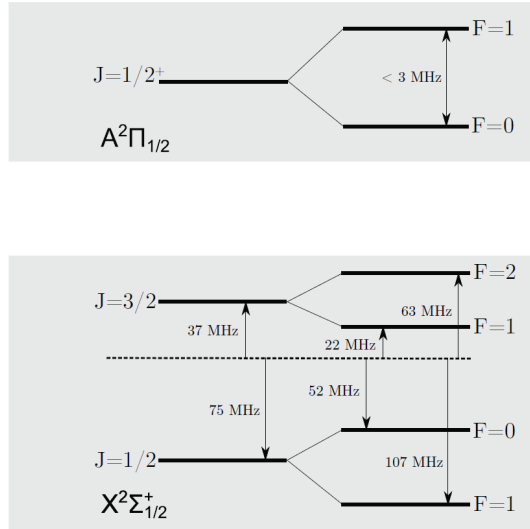


**Figure 4.7:** Hyperfine energy level structure of SrF of the  $N=1$  rotational state in the electronic ground state and  $J=1/2$  state in the first electronic excited state, both states with vibrational quanta  $v=0$ . (Figure from ref. 54)

the hyperfine levels in the excited state causes a large off-resonant excitation<sup>50</sup>, which would lead to a large rate of departure from the dark state. These two arguments suggest that gray molasses is not applicable to this transition in SrF, but we have not investigated all the options of this complicated scheme yet.

#### 4.4.2 RF-knife

In a recent paper<sup>57</sup> by Zeppenfeld et al. an opto-electric cooling method is presented. They use a very sophisticated 3D electric trap<sup>58</sup> which has a flat potential at the center and steep exponential potential at the walls, as shown in Figure 4.8. Utilizing their Stark shift, they can trap  $10^6$   $\text{CH}_3\text{F}$  molecules. An RF signal pumps molecules at the edge of the trap to a state with a smaller Stark shift, thereby dissipating kinetic energy. With a few additional repumping frequencies a closed cooling scheme is obtained. After the cooling stage, an intense RF field is applied to drive the hotter molecules to an untrapped state, keeping only the colder molecules in the trap. With this technique molecules can be cooled down to 29 mK.

Because the potential of the trap is flat in the center, it does not compress the volume of the molecules. Nevertheless, compression could take place when the potential in the trap center is changed to V-shaped or harmonic. However, it then becomes harder to address the optical transitions due to Stark broadening. Another disadvantage of the trap presented in<sup>58</sup> would be that the optical access to the trap center is limited, because the trap is surrounded by electrodes at a very close distance. Nevertheless, the RF-knife is an interesting possibility for cooling molecules, but seems at first sight not directly applicable for improving the loading of a dipole trap.

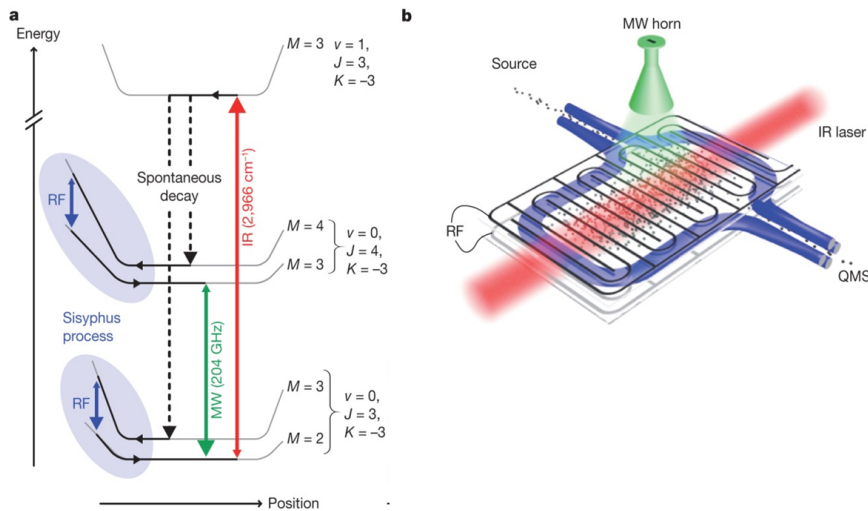


**Figure 4.8:** **a)** Energy level shifts of  $\text{CH}_3\text{F}$  molecules in a micro-structured electric trap. In the strong field edge region molecules lose more energy than they regain when returning to the trap center in a more weakly trapped state. Two repump lasers transfer the molecules back to strongly trapped states, closing the cooling cycle. **b)** Schematic overview of the electric trap, with radio frequency (RF), microwave (MW) and infrared (IR) fields superimposed for the cooling and repumping transitions. A quadrupole mass spectrometer (QMS) is used for detection. (Figure from ref. 57)

#### 4.4.3 Optical one-way barrier

In a paper by Thorn et al.<sup>59</sup> a special optical barrier is applied to  $^{87}\text{Rb}$  atoms in a dipole trap. Two laser beams form a barrier halfway the trap which only atoms approaching from one direction can pass, as shown in Figure 4.9. Atoms traveling from the opposite direction are reflected off the barrier. In this way the volume of the Rb cloud in the dipole trap can be reduced, increasing the phase-space density. This method seems not applicable for compressing a cloud of SrF, because it only offers a 1D barrier. It is quite complicated to compress a 3D cloud with only 1D laser beam barriers.

#### 4.4.4 Continuous loading

In a paper by Yang et al.<sup>60</sup> calcium atoms are loaded into an ODT using spatially selective optical pumping. A sample of calcium atoms in the  $^3\text{P}_2$  state is prepared in a MOT. The ODT is superimposed on the MOT, and traps only atoms in the  $^1\text{S}_0$  state. A laser beam exactly overlapping the ODT pumps the atoms from the MOT cloud into the  $^3\text{P}_1$  state from where they decay into the  $^1\text{S}_0$  state, as shown in Figure 4.10. Atoms in this state are trapped by the ODT, allowing this scheme to continuously trap spatially selected atoms from the MOT into the ODT. The authors claim to reach an increase in phase space density of nearly  $10^3$ , which proves this method is feasible.

For loading our optical dipole trap with SrF molecules however, this method is not suitable. Our ODT is intended to trap all states of the molecule so no spatially selective loading can take place, moreover because there are no states of

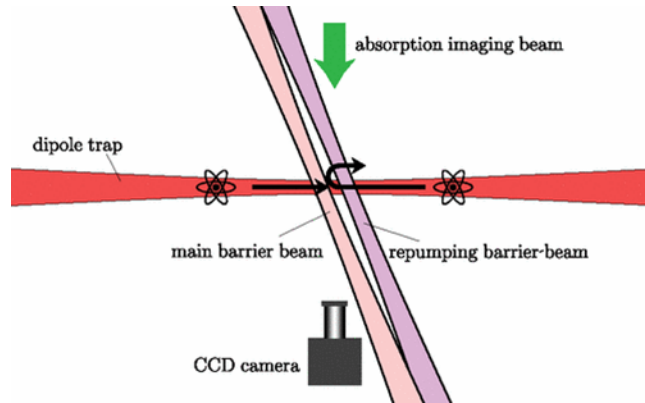


**Figure 4.9:** Schematic overview of a one-way optical barrier for  $^{87}\text{Rb}$  atoms. The main barrier beam forms a potential well for the atoms in the  $F=1$  ground state and a potential barrier for atoms in the  $F=2$  ground state. The repump laser pumps atoms that pass the potential well to the  $F=2$  state, confining them to the right side of the main barrier beam. (Figure from ref. 59)

SrF towards which all the laser cooled molecules can easily be pumped without losing lots of atoms to dark states.

#### 4.4.5 Loading with optical molasses

In a paper by Hamilton et al.<sup>61</sup> loading of an ODT directly from a MOT is compared to loading with optical molasses. They find that using an optimized molasses stage can load twice as much atoms in the ODT as an optimized MOT stage. The only difference between their MOT and molasses is essentially a magnetic field, and they report that applying a magnetic field during loading reduces the number of trapped atoms. They explain this loosely with the fact that the cooling efficiency with a magnetic field is lower away from the small center (zero field region), so at the sides of the ODT the cooling with a magnetic field is less efficient causing the number of trapped atoms to drop.

In a paper by Hudson et al.<sup>62</sup> it is also stated that the loading of an ODT with an optical molasses cooling stage is more efficient than loading directly from a MOT. They report an increase of a factor 40, however this seems mostly due to the low trap depth of their ODT. They mainly use the optical molasses to further cool down the atoms below the depth of the ODT. So this direct comparison with the MOT is unfair because the atom temperature in the MOT is roughly a factor 4 higher.

Nevertheless, in the number of trapped atoms in the ODT reported by Hamilton<sup>61</sup> is  $\sim 2\%$  of the number of atoms in the MOT while Hudson<sup>62</sup> reports  $\sim 5\%$ . Therefore we conclude that in general, optimizing the optical molasses stage will not dramatically improve the number of trapped atoms in an ODT.

#### 4.4.6 Single photon transition scheme

None of the loading options from literature discussed in the previous section seemed directly applicable to our setup. However, inspired by all these inter-

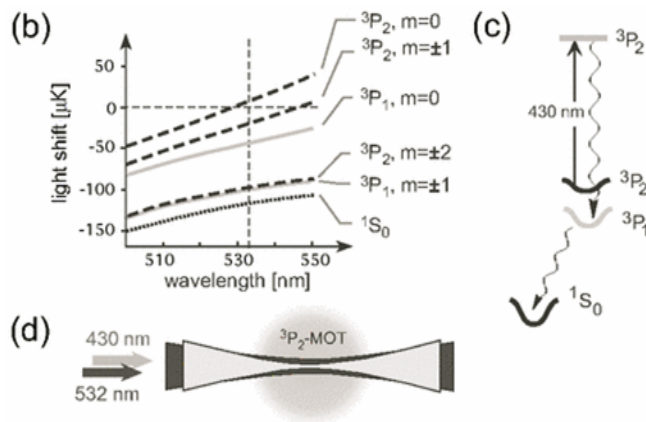


**Figure 4.10:** *b)* Light shift levels for calcium atoms. 532 nm is used as trapping wavelength, where the light shift for the  $^3P_2$  state vanishes. *c)* Atoms initially in the  $^3P_2$  state are pumped in to the strongly trapped ground state  $^1S_0$ . *d)* The ODT and the pump beam exactly overlap such that atoms are selectively transferred into the dipole trap. (Figure from ref. 60)

esting techniques we came up with a loading scheme which might work for our trap: a single photon transition scheme. The main idea is to selectively load SrF molecules into the middle of the dipole trap using an optical transition. In the following section the details are worked out and the advantages and challenges are discussed.

### Exploiting the Stark shift

In Figure 4.11 an overview of the electric trap is shown, with the dipole trap located displaced from the center of the electric trap. The single photon transition scheme uses the Stark shift of the  $v=0, N=1$  ground state of SrF to selectively trap molecules from the electric trap into the dipole trap using only a few photon scatterings.

The potential as function of  $x$  position in the electric trap is shown in Figure 4.12. Initially, all the molecules are in the lfs states. The molecules in the trap are oscillating in all directions, with an average velocity of 2-3 m/s. When the ODT is added to the electrical trap, most of the molecules will just fly straight through, because the ODT is a conservative potential and no dissipation takes place.

Because of the difference in slope of the stark shift between the lfs and the hfs, the center of the dipole trap is slightly displaced between the lfs and the hfs. This effect could be exploited in the single photon transition scheme to selectively load only molecules with zero velocity into the ODT, which are then trapped.

### Trapping in hfs

When the ODT is placed at the side of the electric trap, the velocity of the electrically trapped lfs molecules will drop when they approach the ODT because of the harmonic shaped potential of the electric trap. Molecules with enough

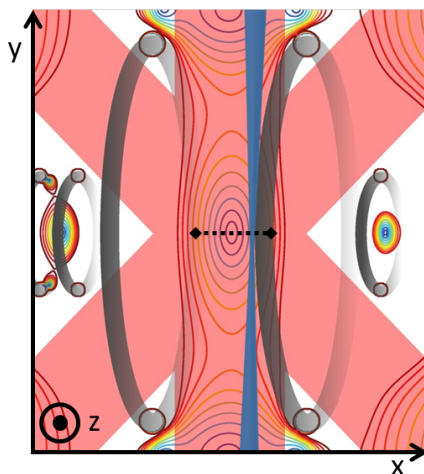


**Figure 4.11:** Overview of the electric trap with superimposed the dipole trap in blue. The three spatial directions as mentioned in the text are indicated. The dotted line shows where Figures 4.12 and 4.15 are located in space. (Figure adapted from ref. 13)

energy to pass the ODT will come to their turning point just after the ODT, where they have zero velocity in the  $x$ -direction. This point is indicated with the red arrow in Figure 4.13. If only the molecules at that position are excited, they most probably decay back into one of the hfs and end up almost exactly in the center of the ODT. Because they had nearly zero velocity in the  $x$ -direction when they were excited, they will be trapped in the ODT potential in the hfs.

Only molecules which have just enough energy to pass the ODT are excited and trapped, molecules with lower energy do not reach that point. In order to trap molecules with lower kinetic energies (in the  $x$ -direction) one could either lower the electrical field, or change the position of the electric field relative to the ODT, and trap all the lower energy molecules. In Figure 4.14 this is shown for an electric field reduced by a factor 2 compared to the original setting. However, now the molecules do not end up in the center of the ODT potential in the hfs. At this point this is not a problem because they are still deep enough in the trap. Nonetheless, one could reduce this effect by reducing the depth of the dipole trap by the same factor as the electric field. However, below 0.2 times the original electric field, the difference in the Stark shift of the lfs and hfs becomes too small to use this single photon transition scheme. This means the selective loading does not work very close to the center of the electric trap.

### Differential Stark shifts

To optically pump only molecules with a certain energy, the pump laser should only be resonant with those molecules. Because the electric field shifts the energy levels of the ground state as well as the levels of the  $A^2\Pi_{1/2}$ ,  $v=0$ ,  $J=1/2$  excited state also the difference between those two states, the differential Stark shift, varies with the electric field strength. Therefore, by adjusting the laser frequency one is only resonant with molecules at a certain position in the electric trap.

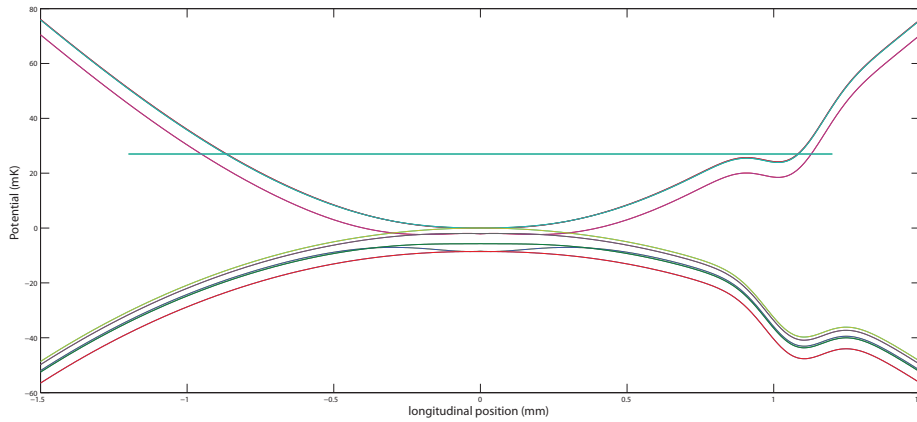


**Figure 4.12:** Stark shifts of the different hyperfine levels of SrF in the electric trap, at the position indicated in Figure 4.11. Initially all molecules will be in lfs (upper two lines) and therefore trapped in the electric potential. Hfs molecules (lower lines) are anti-trapped by the electric potential. At  $x=1.07$  mm the potential of a 15 mK deep optical trap is added, with a waist size of  $200 \mu\text{m}$ . The horizontal line represents molecules with 2-3 m/s velocity.

In Figure 4.15 the differential Stark shifts for the different hyperfine levels of the ground state are shown as function of  $x$ . The two lfs (now the lower lines) can be dressed as indicated by the red lines at the ODT position (black vertical line) in order to employ the single photon transition scheme. An advantage of the differential stark shifts is that once the molecules are in the hfs, trapped in the ODT, they cannot be excited again, because their (differential) stark shifts have opposite signs. However, from the figure it can be seen that the laser frequency for pumping the  $F=1, M=0$  lfs (upper of the two lower lines in the figure) is also resonant with the  $F=2, M=0,1$  lfs (lowest line) at a position closer towards the trap center, indicated by the upper red dotted line. This would imply that molecules from this state can be excited at the wrong position (not ending up in the ODT), become untrapped in the hfs and are lost from the trap. To circumvent this problem one could adjust the laser beam position such that laser is absent at this spot (indicated by the red solid line). However, one must then be very careful with reducing the trap depths to capture lower energy molecules, because the position of the single photon trapping might change, as can be seen in Figure 4.14. Note that for the  $F=2, M=0,1$  lfs (lowest line) pumping laser this is not a problem, because the resonance from this laser with the  $F=1, M=0$  lfs (upper lower line) is further from the electric trap center, where no molecules are apparent (because they are already transferred to the hfs when passing the single photon transition location).

### AC Stark shift

So far it was assumed that the differential Stark shift is not influenced by the ODT. This is however very unlikely, the dipole trapping laser will most probably induce an AC Stark shift in both the ground state and excited state. At this point, the AC polarizability of the involved states of SrF is not known and therefore we cannot calculate the AC Stark shift of these states easily. In a

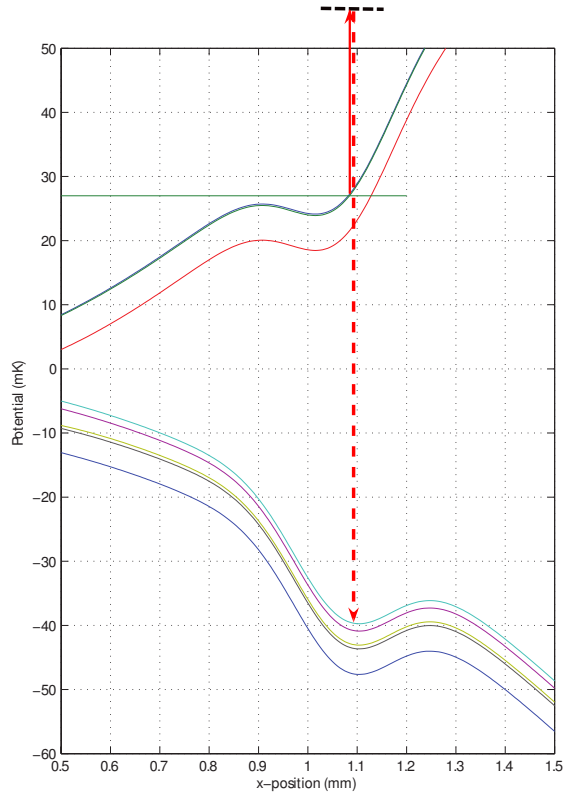


**Figure 4.13:** Zoom in of Figure 4.12, at the position of the arrow the molecules are excited from the lfs and decay most probably back into one of the hfs, in which they are trapped by the ODT, as explained in the text.

recent paper from Kotochigova et al.<sup>63</sup> it is shown that the AC polarizability of the excited state can be tuned to be the same as in the ground state by changing the angle between a background field and the polarizability of the dipole trapping laser. This means that the differential Stark shift caused by the dipole trap can be tuned to zero for certain states. This would resemble the situation in Figure 4.14. Because these AC Stark shifts are not yet known, they are taken as zero for now. But in principle a non-zero AC Stark shift does not prevent the single photon transition scheme to work, one would only need to adjust the laser frequency, ODT depth and electric field strength accordingly.

When the electric trap depth is reduced, the differential Stark shift is also reduced, therefore the single photon transition laser should follow. This means the frequency has to be changed over a few hundred MHz, carefully following the reduction in the electric field strength.

### 3D confinement

Until only the  $x$ -direction has been considered, but the molecules must also be confined in the  $y$ -direction. When the single photon transition lasers are directed along the dipole trapping laser direction, therefore overlapping the ODT, a first cooling step in the radial direction can be made in the single photon transition

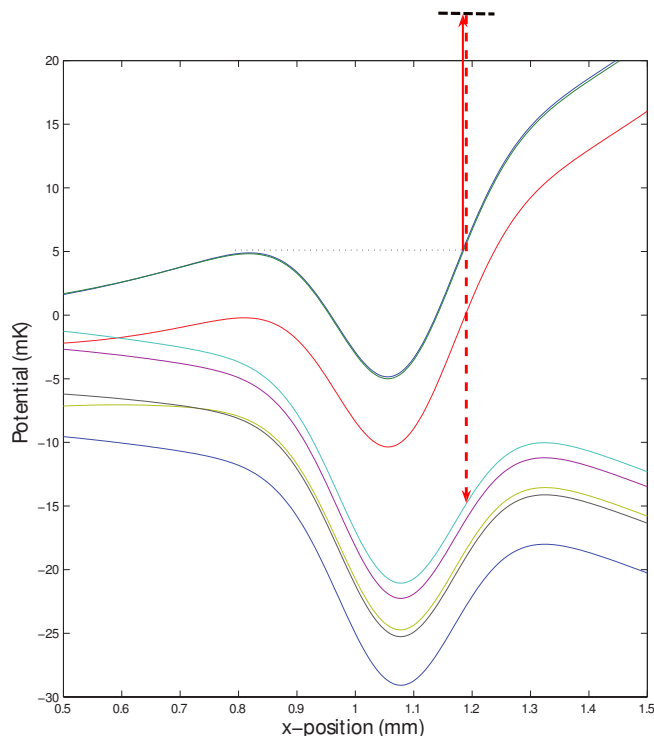


**Figure 4.14:** Zoom in of Figure 4.12, with the electric field reduced by a factor 2. At the position of the arrow the molecules are excited from the lfs and decay most probably back into one of the hfs seeking states, however now they do not anymore end up exactly in the middle of the ODT, as explained in the text.

itself when those lasers are detuned slightly to the red. Further cooling in the  $y$ -direction could be done inside the dipole trap, because then the hfs are not lost, which would be the case when cooling only in the electric trap. Cooling inside the ODT is however not trivial, and should be investigated in detail.

In general, atoms will have a velocity component in all three directions. The above mechanisms can cool the velocity components in the  $x$  and  $y$  direction, but when the velocity in the  $z$  direction is not cooled, molecules cannot be trapped in the ODT. Cooling in the  $z$  direction can only take place inside the ODT, because cooling anywhere else will pump the molecules to the hfs where they will quickly escape from the trap. So also a cooling laser in the  $z$  direction to cool the molecules inside the ODT is needed.

### Wing-losses

Another problem arising from the 3D picture is that the potential for the hfs trapped in the ODT displaced from the center of the electric trap drops for high and low  $x$ . This can be seen in Figure 4.16. Because we use a resonator cavity, the trapping laser forms a standing wave and the molecules are confined to the light-maxima in the direction of the dipole trapping beams. However, if this force is not strong enough to counteract the potential drop of the hfs in this direction due to the electric field, molecules can leak out of the trap. In

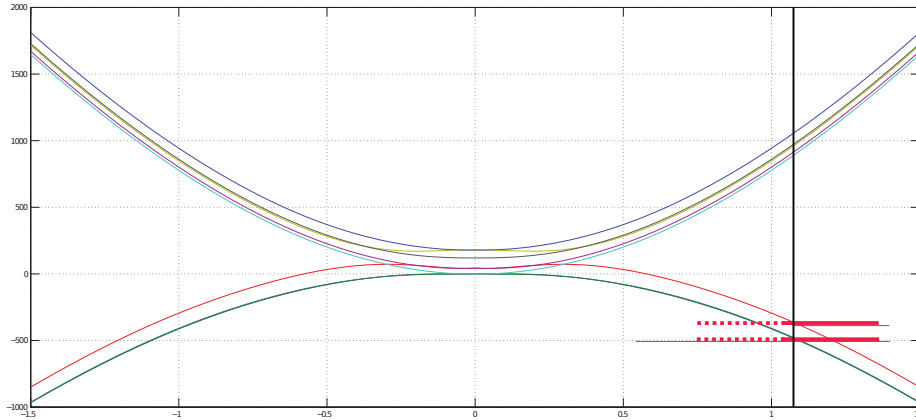


**Figure 4.15:** *Differential stark shift of the hyperfine levels from the 663 nm transition in SrF as function of  $x$ -position in the electric trap. Now the lower states are lfs, while the upper states are hfs. The red lines indicate the resonance of both lfs with the pump laser, at the position of the single photon transition (black vertical line), as explained in the text.*

a paper by Griffin et al.<sup>64</sup> it is stated that Rb atoms usually end up in the wings of the ODT, because the differential light shift is smaller there. If this would happen in our trap, then molecules would leak away easier, so it should be investigated whether the effect of wing-loading would also take place in our trap with molecules.

### Summary

In summary, the single photon transition scheme can be a feasible way to increase the transfer efficiency from the electric trap to the dipole trap, but there are several issues which should be taken care of in order for the scheme to work, they are listed below.

#### Advantages:

- Large transfer ratio from electric trap to ODT.
- Only 3 counter-propagating laser beams needed (1  $y$ -cooling, 1  $z$ -cooling, 1 pump transition).
- No further fields or modifications needed.

#### Challenges:

- Make sure the  $F=1, m=0$  lfs single photon transition beam does not excite the lfs  $F=2, m=0,1$  lfs at the wrong spot, or make sure molecules excited there are not lost.
- Calculate the AC Stark shift for all ground states and the excited state.
- All laser frequencies must be carefully swept by a few hundred MHz when the electric trap depth is reduced, or when the electrical trap center is displaced.

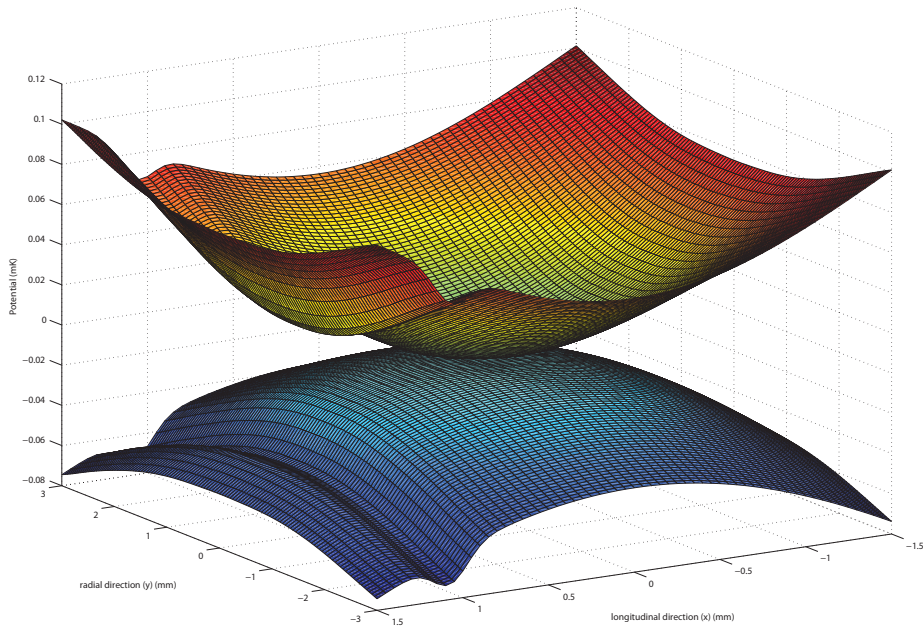


**Figure 4.16:** 2D potential of the electric and dipole trap for the  $F=2, M=0$  lfs (upper surface) and  $F=0, M=0$  hfs (lower surface). It looks like molecules in hfs can 'roll out' of the ODT in the  $y$ -direction, but this is prevented by the potential of the 1-D optical lattice, as explained in the text.

- Laser cooling inside the ODT must work in both  $y$ - and  $z$ - direction.
- Leakage from the wings of the ODT should be prevented.
- Make sure no molecules are lost during lowering of the electrical potential, or during the change in position of the electric field minima with respect to the dipole trap.

## 4.5 Test setup

After the conceptual design of the dipole trap setup was finished, the ordering of parts and building the setup could start. However, since the building of the decelerator was delayed by problems with the high voltage amplifiers, the deceleration and laser cooling of molecules took longer time. This implied that there would be no decelerated molecules to capture in the dipole trap in the near future. Therefore it was decided to start with building the locking part of the dipole trap laser system. Once this works, we could move on to the trapping part of the setup. The locking does not need to take place in vacuum, so for simplicity it was decided to first build a cavity setup at room pressure and try to implement the PDH cavity lock. In Figure 4.17 a schematic overview of the test setup is shown. In the next sections, the different parts of the setup will be discussed and finally the first results will be presented.

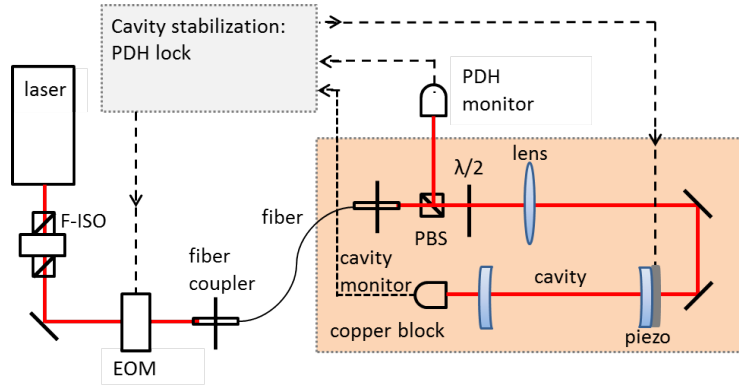


**Figure 4.17:** Schematic overview of the test setup as it was realized to implement PDH locking of the cavity.

## Mirrors

The cavity mirrors are the most critical part of the setup and therefore we have carefully selected their properties. As we determined earlier (see Table 4.2), the reflectivity of both mirrors should be 0.998, the shape should be concave with a ROC of 0.25 m. The size of the mirrors was not specified before but since one of the mirrors is attached to a piezo element, one should take into account the mechanical vibrations of the mirror-piezo system. Glue can be used to attach the mirror to the piezo, but since this is always a tricky process with the risk of spilling glue on the mirror, we decided to try clamping the mirror and piezo with a spring. The resonance frequency of a mass-spring system is given by  $\sqrt{k/m}$ , with  $k$  the spring constant and  $m$  the mass. We want to avoid resonances and hence be far below the resonance frequency. Therefore we select the smaller 1/2" mirrors with a lower mass. The resonance frequency of the system is then  $\sim 11$  kHz, which is just right since it is slightly above the locking bandwidth we aim for.

One aspect not mentioned before is the mirrors must be able to withstand the high intensity of the trapping beam. To calculate the power at the mirrors, we use (2.60) and plug in (2.45) to obtain:

$$I = \frac{2P_0}{\pi w_0 \sqrt{1 + \frac{z}{z_0}}} \quad (4.9)$$

Which gives at the mirror position  $z = d/2 = 9\text{cm}$  an intensity of  $I \sim 2 \text{ MW/cm}^2$  for 10 kW intra-cavity power. The laser intensity damage threshold (LIDT) of the mirrors should thus be higher than this value. Because of the high power on the mirrors they will start heating, which causes deformations and changes the properties of the cavity. This issue is discussed by Edmunds and Barker<sup>28</sup> and depends a lot on the switched on / switched off time of the trapping laser. Because for the test setup we will use only a low power locking beam, this issue is not further investigated here. Finally, the mirrors should also be suitable for use in the UHV.

With all the parameters set we requested quotations from two companies, Layertec and Laseroptik. To save money and time we decided for now to drop

the UHV and high power requirements since these are not necessary for the test setup. These aspects will become important when the trapping beam path is included. The reflectivity and transmittance of the Laseroptik mirrors were with 99.8 % and 0,1%, respectively, closest to our demands so these mirrors were bought.

For mounting the mirrors, Polaris™ mounts from Thorlabs were selected. They offer a high stability, low thermal expansion coefficient as well as UHV compatibility.

### Copper baseplate

As shown in Figure 4.17, the cavity mirrors are placed on a copper block. Ideally, one would want to mount the cavity mirrors directly to a tube material having an ultra low thermal expansion coefficient, such as Zerodur or ultra low expansion glass (ULE), to minimize the sensitivity of the cavity to temperature changes. However, having a tube around the dipole trap limits the optical access and is hard to fit together with the ring-shaped electrodes close by the cavity focus. Therefore we plan to use the Polaris mirror mounts to attach the mirrors to a rod of material, which then could be temperature stabilized if necessary. Because ultra low expansion materials are expensive and limited in availability, we decided to first use copper as base material for our test setup and see if this would be satisfactory. Copper has a thermal expansion coefficient of  $16.5 \cdot 10^{-6}/K^{65}$ , which could cause a drift in cavity length of  $3\mu\text{m}/^\circ\text{C}$ , roughly three wavelengths. For the test setup this seems acceptable since the PDH lock will be much faster than the thermal drifts, and therefore be able to keep the cavity locked during slight changes in temperature.

The advantage of having a copper block as a base material is that we can also mount mode matching and alignment optics on the same baseplate and therefore minimize mechanical drifts and vibrations between the alignment optics and cavity mirrors. This is important since the power buildup in the cavity is very sensitive to misalignments, even though the cavity mirrors are in an intrinsically stable, confocal configuration as explained in section 2.3.3. The laser beam is transported to the copper block by an optical fiber, offering two main advantages. First, the output from the fiber is a nicely shaped Gaussian beam, which has maximum incoupling efficiency to the TEM<sub>00</sub> mode of the cavity, as mentioned in section 2.3.4. Second, mounting the fiber outcoupler directly on the copper block removes any mechanical vibration caused by optics earlier in the beam path.

### Mode matching

In order to couple the light coming from the fiber efficiently into the cavity, we can use the formulas discussed in section 2.3.5. Substituting the refractive index of the incoupling mirror of 1.5, a cavity waist of  $200 \mu\text{m}$  and a wavelength of  $1064 \text{ nm}$ , we obtain from (2.50) a virtual waist  $w_{0vir} = 165\mu\text{m}$ . Using the thickness of the mirrors,  $6.35 \text{ mm}$ , equation (2.51) gives  $z_{vir} = 9.7 \text{ cm}$  as the distance between the focus of the mode matching lens and the front mirror. We set the focal length of the mode matching lens to  $25.0 \text{ cm}$  as a convenient length for alignment, which means the position of the lens should be  $15.3 \text{ cm}$  from the incoupling mirror. Now we use (2.52) and we get a beam waist of  $0.5$

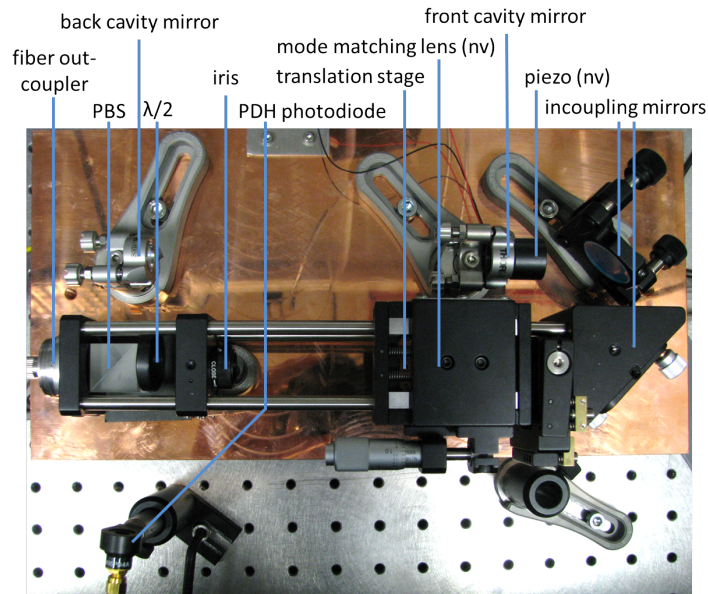


**Figure 4.18:** Picture of the parts of the test cavity setup mounted on the copper baseplate. The light enters through the fiber outcoupler on the left. The part reflected from the cavity is measured by the photodiode on the bottom and used for the PDH locking, the transmitted part is monitored by a similar photodiode behind the cavity, not visible (nv) on this picture.

mm, which means that the incoming collimated beam should have a diameter of 1 mm. This we can easily make sure by selecting a proper output coupler for the fiber, in our case the PAF-X-5-B from Thorlabs which has a waist diameter of 1.00 mm. To be able to optimize the position of the mode matching lens experimentally, it was mounted inside on a cage system, in which its position along the beam can be changed without altering the alignment, as shown in Figure 4.18.

### PDH lock

To implement the PDH lock on the cavity an EOM was placed in the beam path before the fiber, and a 90:10 beam splitter was placed in front of the cavity to split off the reflected beam. However, the signal from this beam splitter turned out to be too weak to provide a proper feedback signal. Therefore a polarizing beam splitter and a half waveplate was inserted, to direct all reflected light to the photodiode. The light from the photodiode is send to a DigiLock module from Toptica. This digital module is controlled via a PC and can be used to implement different locking schemes, including the PDH lock. The module also generates a RF signal which is amplified and send to the EOM to generate the sidebands. The feedback is fed to a Scan Control module from Toptica which amplifies the signal and drives the piezo element behind the front cavity mirror. A picture of the setup is shown in Figure 4.19. Because the Mephisto laser had not yet arrived, we used a Koheras fiberlaser as temporarily beam source, although it produced light of a slightly different frequency,  $\lambda = 1107.8$  nm, with

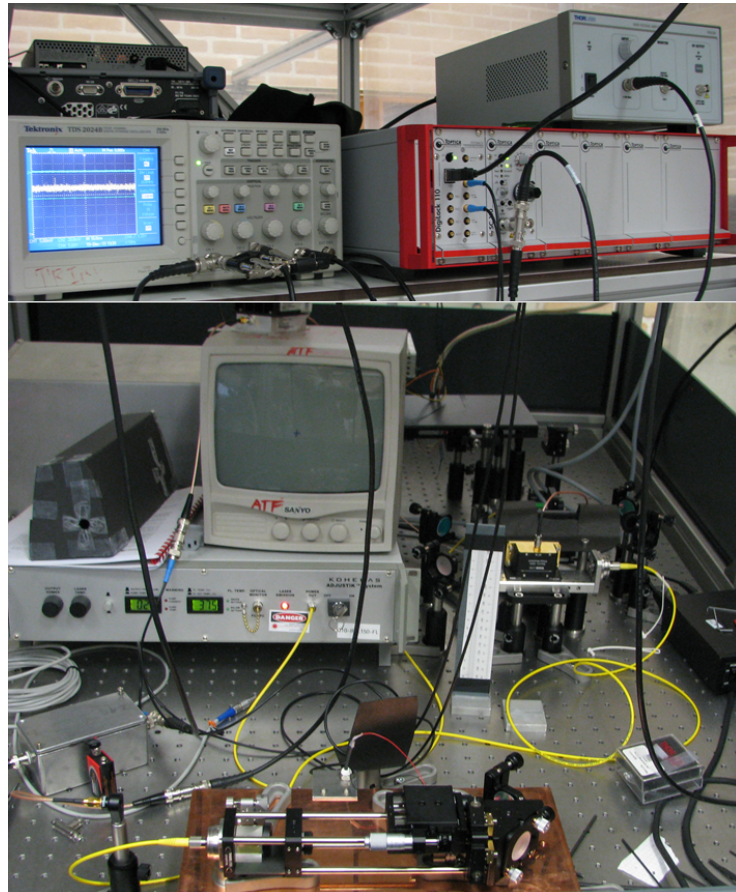


**Figure 4.19:** Picture of the test cavity setup. Below: optical beam path starting from a Koheras fiber laser, after which the light is guided through an optical isolator and EOM on the right, and then send through an optical fiber to the cavity on the copper baseplate (details in Figure 4.18). A camera is used to align the cavity to the infrared beam. Top: Locking electronics, with the DigiLock and Scan Control module from Toptica mounted in a DC 110 electronics rack and the oscilloscope used to monitor reflected and transmitted intensities.

a linewidth of  $\sim 100\text{kHz}$  and a power up to  $30\text{ mW}$ .

## Results

After carefully aligning the cavity mirrors to the infrared beam, the piezo was set to scan the cavity length at  $25\text{ Hz}$ . When the cavity length comes across a resonance, a sharp peak in the transmitted intensity is observed, while at the same instant there is a dip in the reflected intensity. The ratio of the inter-peak distance to the peak width gives the Finesse of the cavity, as in (2.38), for our cavity this turns out to be  $\sim 1300$ . This number is slightly lower than we calculated in Table 4.2, but on the right order of magnitude. The lower Finesse is probably caused by an imperfect alignment and scattering losses in the cavity; recall that in Table 4.2 we assumed a vacuum and therefore zero scattering losses in the medium while the test cavity is operating at room pressure. The reflected intensity drops below  $20\%$  of its nominal value at a resonance, which means the incoupling efficiency, mainly determined by the alignment and mode matching optics, is  $> 80\%$ . This value is fairly good for a first test setup compared to literature, for instance in<sup>28</sup> and<sup>40</sup> they report incoupling efficiencies of  $30\%$  and  $45\%$ , respectively.

With the cavity alignment optimized the EOM was switched on, generating sidebands for the PDH lock, and the reflected beam intensity signal was used to lock the cavity length to the laser frequency. After some trial and error with the digital locking interface, this succeeded and the cavity could be locked to a resonance peak stably for several minutes. Due to a lack of time however, the locking parameters were not yet optimized and no long term stability measurements were taken.

## 4.6 Conclusion

In this chapter a design for a trap was made to capture laser cooled SrF molecules. According to the calculations done it is possible to make a dipole trap with a sufficient trap depth and volume to capture a significant amount of SrF molecules. It was found that it is thereby very important have extremely low noise in the laser frequency and intensity in order to reach trapping lifetimes of  $1\text{ s}$ , as was imposed by the initial requirements. The most efficient way of reaching the high laser power regime, needed for the dipole trap, is by using an enhancement cavity, as was done in several other experiments with atoms, reported in literature. Based on a paper by Edmunds and Barker I designed an experimental setup which provides all important requisites for the dipole trap: operation in UHV, high laser power  $\sim\text{kW}$ , very low intensity and frequency noise, stable operation and dynamic control of the trap depth.

None of the investigated experimental tricks from literature are directly applicable to improve the transport of SrF molecules from our electric trap to the dipole trap. Therefore we came up with a new, single photon transition scheme in which a Stark shift asymmetry is exploited to resonantly transfer lfs molecules to the center of the dipole trap potential in hfs. Using only a few extra laser beams, this method looks promising and should be able to increase the loading efficiency of the dipole trap. However, there are still some challenges which should be investigated, for instance by simulations, to proof the method

is really feasible.

Finally, the first part of the experimental setup was built and light was coupled into a test cavity. With a Finesse of 1300 and an incoupling efficiency of over 80 %, the cavity behaves as predicted by the preliminary calculations. The PDH locking of the cavity length to the laser frequency has proven to work and thereby the goal of the test setup was accomplished. The next step is to improve the stability of the lock by optimizing the locking and alignment parameters. Then the rest of the designed experimental setup can be built, of which the most important parts have already been selected.

## Chapter 5

# Transfer cavity lock

In this chapter the building and testing of a transfer cavity lock for one of our cooling lasers is described. First, the choice for a transfer cavity lock is explained and the stability aims are stated. Then an overview of the experimental setup is given, discussing the main components of the lock system. In the third section, the first results are presented and discussed. The chapter ends with a conclusion and an outlook where further improvements for the lock are suggested.

### 5.1 Locking objectives

The most common way to keep a laser at the right frequency is to lock it to an atomic or molecular transition, as is currently done with our 663.3 detection laser, which is locked to an Iodine resonance. However, this lock turned out not to be as stable as was anticipated. Mainly the limited available power, the small capture range and high sensitivity to temperature variations cause the system to become unlocked easily. Lately, the average locking time was less than 30 minutes, and since the current deceleration experiments going on rely on resonant detection of the molecules by the 633.3 nm laser<sup>11</sup>, the locking instability causes serious delays in doing measurements.

An alternative technique for locking a laser is the scanning transfer cavity lock (TCL). Instead of providing an absolute frequency reference, this method transfers the stability of a reference laser to the laser cooling laser by keeping their frequency difference at a fixed value. Both beams are sent into an optical cavity of which the length is scanned by a piezo. Resonance peaks arise from each beam when the cavity length equals a half-integer times the wavelength, therefore in general two sets of equidistant peaks arise, each from one laser frequency, as shown in Figure 5.1. Usually the cavity is scanned over one or a few FSR, such that from each laser one or a few peaks arise. The lock works by determining the difference between two peaks, each from one laser, and keeping this at a constant value by adjusting the frequency of the laser cooling laser.

The scanning TCL provides several advantages over an absorption spectroscopy lock. First of all, since the lock does not depend on an atomic transition it can be used to lock at any frequency by adjusting the inter-peak difference accordingly. Second, the capture range is set by the FSR of the cavity, usually a few GHz, and is therefore much larger compared to absorption locking. Fi-

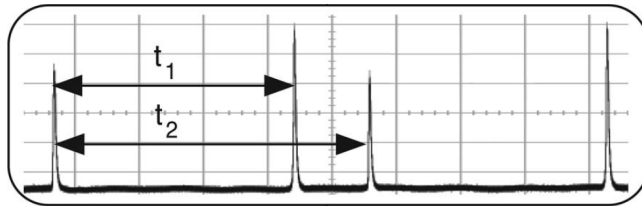


**Figure 5.1:** Cavity transmission signal for a single piezo scan over 2 FSR. The two lower peaks arise from resonances with the reference laser, while the two higher peaks originate from the cooling laser. A simple TCL lock works by determining the difference  $t_2 - t_1$  and keeping this at a constant value by adjusting the frequency of the cooling laser. (Figure from ref. 66)

nally, only a low amount of power is needed for this type of lock since the cavity enhances the light at resonance and therefore provides a strong peak signal in general. In the past a TCL was considered expensive and complex since one needs a stable reference laser, a transfer cavity and a control system. However, recent developments have shown the lock can be implemented in a cost-effective way using a simple feedback system<sup>66</sup>. Also once implemented for a single laser, the same reference laser can be easily used to lock several laser cooling lasers at different frequencies<sup>67</sup>.

The  $X^2\Sigma^+(v=0) \rightarrow A^2\Pi_{1/2}(v'=0)$  SrF transition at 663.3 nm has a lifetime of  $\tau = 1/\Gamma = 24.1$  ns<sup>35</sup>. The Iodine lock we use for this transition has an estimated short term stability of 2-5 MHz, which is on the same order of magnitude as the ECDL linewidth. This is good enough for the 663 nm transition because its linewidth is slightly larger:  $\Gamma = 2\pi * 7$  MHz. However, for the  $X^2\Sigma^+(v=0) \rightarrow A^2\Pi_{1/2}(v'=1)$  transitions at 686.0 nm the lifetime is much smaller because of the smaller branching ratio. Ideally, one would want the laser then also to have a smaller linewidth and better stability, but since this is not crucial we set the stability objective of the scanning TCL first at  $\sim 1$  MHz, also because the linewidth of the ECDL we use has a linewidth  $\sim$  MHz anyway.

## 5.2 Experimental setup

Starting from the cost-effective and simple realization of a scanning TCL by Burke et al.<sup>66</sup> we studied some other implementations in literature<sup>67;68;69;70</sup> and then decided on the experimental setup we would build for stabilizing our 685 nm cooling laser. A schematic overview of the locking system is shown in Figure 5.2, and in the next sections the most important parts of the setup are discussed.

### 5.2.1 Reference laser

The most easy choice for the reference laser would be the 663 nm laser, which is locked to the Iodine cell and therefore can provide an absolute frequency reference. However, as discussed in the previous section we are currently not satisfied with the locking stability of the 663 laser and using this laser as reference means that every time the 663 nm laser unlocks, also the 686 laser might loose its lock

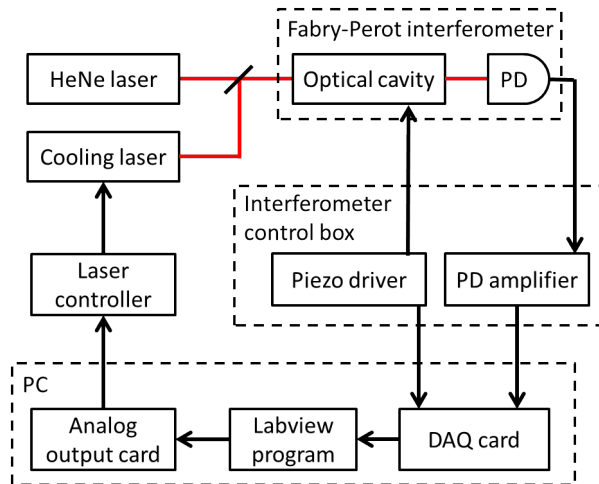


**Figure 5.2:** Schematic overview of the lock system. Both lasers are sent into an optical cavity, which is scanned by a piezo driver in the control box. Both the amplified transmission signal and the scan trigger signal are sent to the PC, which generates a feedback signal for the cooling laser.

and both will have to be relocked manually again. Since this process costs a lot of time and because we want our TCL to be more stable than the Iodine lock we decided not to use the 663 laser as a reference. In fact, if the TCL turns out to work much better than the Iodine lock we might also use it to lock the 663 laser and discard the unstable Iodine lock completely.

The newly bought Mephisto MOPA 1064 nm laser for the optical dipole trap could also be used as a frequency reference. The intrinsic stability of this laser is specified as  $< 1$  MHz/min. This means the frequency can drift up to 60 MHz/hour, which is obviously not stable enough for our purpose, since we aim for a stability of  $\sim 1$  MHz. Moreover, the wavelength difference between the Mephisto and the 686 laser is quite large (338 nm), which makes the lock more sensitive to temperature and pressure changes, as will be discussed later on.

Another option is to buy a new reference laser, such as a Helium Neon (HeNe) laser, which are internally stabilized and commercially available. Because of its easy way to set up and good frequency stability we decided to buy the 25-STP-912 HeNe laser from Melles Griot. This laser has a wavelength of 632.8 nm and an intrinsic frequency stability of  $< 1$  MHz/h. The laser is delivered with its own power supply and needs no further control electronics: by switching on the power the laser warms up, stabilizes itself and is ready to use within 10 minutes.

### 5.2.2 Transfer cavity

Mainly the transfer cavity determines how efficient the stability of the reference laser is transferred to the cooling laser and therefore its properties should be selected carefully. In Burke's experiment<sup>66</sup> they use a commercially available confocal cavity with a FSR of 1.5 GHz and a finesse of 550. They find a long term locking stability of  $\sim 1$  MHz, mainly limited by drifts in the optical path length in the cavity caused by both pressure and temperature changes. The

resulting drift in the cooling laser frequency is given by

$$\dot{\nu} = \frac{\Delta\nu}{\nu_{FSR}} R, \quad (5.1)$$

where  $\Delta\nu$  is the frequency difference between the cooling laser and the reference laser and  $R$  is the drift in the FSR of the cavity. The authors report a typical drift rate of  $R = 1$  kHz/h, using no further stabilization of their cavity. In a paper by Rossi et al.<sup>70</sup> thermal stabilization of the cavity is used, but because of their larger frequency difference,  $\Delta\nu = 43$  nm versus  $\Delta\nu = 3$  nm in Burke's experiment, they obtain a slightly worse long term stability of  $\sim 4$  MHz. In an experiment by Uetake et al.<sup>69</sup> the transfer cavity is temperature as well as pressure stabilized, by placing it in a non-evacuated tube to protect the cavity from humidity and pressure changes. A long term stability of 100 kHz is achieved, with an even larger frequency difference of  $\Delta\nu = 233$  nm.

In our case  $\Delta\nu = 27.9$  m GHz, which would result in a long term stability of 19 MHz with a  $\nu_{FSR}$  of 1.5 GHz and the same  $R$  as measured by Burke. To decrease this number one could take a larger FSR, but this implies a longer cavity, according to (2.33), and in a longer cavity changes in pressure and humidity have a larger effect on the FSR, therefore increasing  $R$ , leading to a worse stability. A better option would be to stabilize the temperature or pressure in the cavity as was successfully done in the experiments by Rossi and Uetake.

For the first version of our TCL we decided to use the SA200-5B scanning Fabry-Perot cavity from Thorlabs, with  $\nu_{FSR} = 1.5$  GHz and a finesse of  $> 200$ . This cavity is easy to use since it is delivered with a piezo and a photodiode. If necessary, later on we can install temperature or pressure stabilization on this cavity, but at first we will try how good the locking works without this.

### 5.2.3 Feedback system

The experiment by Burke uses a micro-controller to generate a feedback signal for the laser. Since we already have a data acquisition card and a PC available we decided to use these to provide the feedback for our cooling laser. The data acquisition card in our PC is a PCI-6023E from National Instruments. A Labview program was written to readout the data from the photodiode and transfer this into a feedback signal which is then fed to the cooling laser.

The piezo is driven by a SA201-EC interferometer control box (ICB) from Thorlabs, generating a 50 Hz ramp signal which scans the cavity length. The photodiode signal measuring the cavity transmission is amplified in the same ICB and send to a data-acquisition card (NI PCI-6023E from National Instruments) in the PC. The external trigger signal from the piezo scan is also fed to the PCI card. When a trigger pulse arrives, the PCI card starts sampling a specified number of values from the photodiode, and thus acquires a waveform for a single cavity scan. The offset and range of the scan are manually adjusted with knobs on the ICB such that one FSR is scanned and exactly three peaks are recorded. In Figure 5.3 the Labview interface is shown, with the three transmission peaks visible in the middle. The two outer peaks are from the reference laser, while the middle peak arises from a resonance of the cooling laser.

The Labview program locates the peaks by first taking the derivative of the sampled photodiode signal. Subsequently, each individual value of the derivative signal is multiplied by the next individual neighboring value. The resulting



**Figure 5.3:** Interface of the Labview program generating the feedback signal for the cooling laser.

list of values are all positive, except the ones next to a zero-crossing in the derivative signal (multiplying two negative values results in a negative value, while multiplying a positive and a negative value results in a negative value). So the peaks are located at the zero's in the latter list, and having found the peak positions the program calculates the (scan time) difference between the two outer (reference) peaks  $t_2$  and the difference between the first two peaks  $t_1$  (using the same labeling as in Figure 5.1), which appear as numbers in the Labview interface in Figure 5.3. The ratio between the two differences,  $\delta = t_1/t_2$  is then compared to a value  $\Delta_{set}$ , which is set by the user. This difference  $\Omega = \Delta_{set} - \delta$  gives an error signal with a zero-crossing at  $\delta = \Delta_{set}$ , so using  $\Omega$  as laser feedback will push the laser frequency such that the ratio  $\delta t_1/t_2$  becomes equal to  $\Delta_{set}$ . Therefore  $\Omega$  is amplified by a gain factor and send to an analog output card (NI PCI-6023), which is connected to the cooling laser control box. The frequency of the laser will be adjusted according to the feedback signal and the cooling laser resonance peak will move such that  $\Omega$  converges to  $\Delta_{set}$ . For each scan a feedback signal is generated and thus the feedback loop has a bandwidth of 25 Hz. The ratio  $\delta = t_1/t_2$  rather than the absolute peak difference  $t_2 - t_1$  is used since in this way variations in the scan rate cancel out.

## 5.2.4 Laser controller

As mentioned in section 1.3, we use a home built ECDL the generate the laser cooling light. We use a Moglabs DLC-202 laser controller to operate our ECDL.

The temperature of the laser can be set on the control box and a feedback loop keeps the laser temperature stable at the set value. The laser frequency and intensity are controlled via both the diode current and a high voltage send to a piezo element behind the laser cavity grating. The control box can be used as a locking system itself: when a photodiode signal is offered to the box, a slow (piezo) and a fast (diode current) feedback loop can lock the laser, for instance to an atomic resonance. However, the internal lock system is not sophisticated enough to be used for a transfer cavity lock, since it can not calculate the difference between specific peaks in a photodiode signal. Therefore we offer the feedback signal from the PC as an external error signal to the box. The error signal offset and gain can then be adjusted on the control box and fed back to the laser via both the slow and fast feedback loop.

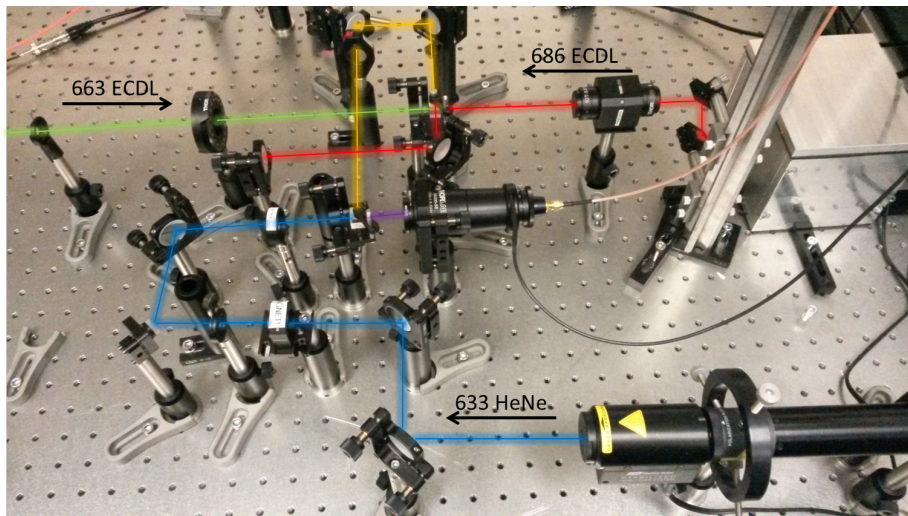


**Figure 5.4:** Picture of the optics setup for the TCL. The HeNe laser beam (blue) is send into the transfer cavity (middle of picture) via four alignment mirrors, through a mode matching lens and a BS. The 663 laser light (green) is send in through the iris on the left, reflected by the PBS, and then via two alignment mirrors (top of picture) and a mode matching lens merged with the HeNe light in the BS (purple), ending up in the cavity. The 686 ECDL is placed on the right, and the light (red) is first double passed through a PBS, allowing for independend alignment by the two mirros in the middle of the picture, before it is merged with the 663 laser beam path (orange).

### 5.3 Results

During the implementation of the TCL we had problems with the Moglabs box controlling our cooling laser. The slow locking function did work due to some internal malfunction of the box. Since the feedback signal is relatively slow ( $\leq 25$  Hz), this slow locking function is crucial for our setup. Therefore the box was send back to the manufacturer to be repaired and in the meantime we used our 663 laser, which is operated by the same type of control box, to test the TCL. Therefore we had to feed the 663 laser light into the the transfer cavity, which is shown in a picture of the optics setup in Figure 5.4. All results below

are thus obtained with the 663 nm laser. This comes with the advantage that we can now easily compare the TCL with the Iodine lock which is normally used to lock this laser.

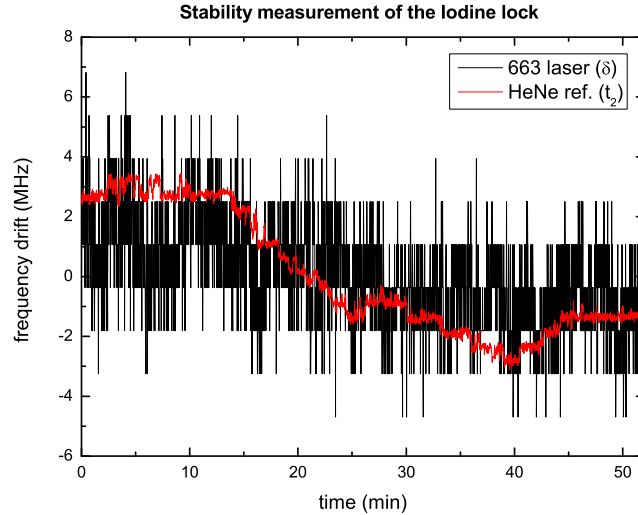


**Figure 5.5:** Frequency drift of 663 laser locked to the Iodine cell (black) with respect to the HeNe laser, recorded in the transfer cavity. The red line shows the drift of the reference scan time  $t_2$ . The resolution of the black line is low caused by rounding of the variable while it was stored, and is thus not limited by the acquired photodiode signal.

To first determine the stability of both the transfer cavity itself and the recorded photodiode signal, the 663 laser was locked to the Iodine peak and the cavity transmission was recorded by the Labview locking program. A plot of the reference peak distance  $t_2$  in the cavity and the relative 663 laser peak position  $\delta = t_1/t_2$  is shown in Figure 5.5. The reference scan time  $t_2$  represents the distance in cavity length between two adjacent cavity modes of the same input laser frequency, given by the FSR. Despite the fact that the FSR of a cavity is fixed, the mode spacing  $t_2$  does depend on the laser frequency because FSR is a frequency difference, and the mode spacing  $t_2$  will decrease for higher absolute frequencies. The drift of  $t_2$  visible in Figure 5.5 of  $\sim 3$  MHz/h can however not be explained by variation in the cavity mode spacing since the frequency drift of the HeNe laser is  $\leq 1$  MHz/h, which causes a negligible effect on the cavity mode spacing. Because most environmental variations such as temperature and pressure do only change the absolute peak position in the cavity and not the mode spacing  $t_2$ , the drift in  $t_2$  can only be attributed to variations in the scan rate of the piezo, or non-linearities in the ramp signal. The real mode spacing of the cavity does thus not change, it is the recorded mode spacing  $t_2$  measured in the time domain which changes due to either variations or irregularities in the scanning of the piezo. The relative 663 peak position  $\delta$ , although not very resolved in this figure, seems to follow the drift of the mode spacing  $t_2$ . This is remarkable, since variations in the scan rate should cancel out by the division of

$t_2$  in  $\delta = t_1/t_2$ . This implies that either the drift of  $\delta$  is caused by non-linearities in the scan or by environmental effects (temperature, pressure, etc.) and is by coincidence similar to the drift of  $t_2$ . The figure confirms the estimated short term ( $\leq 1$  s) stability of the Iodine lock, with a standard deviation of  $\sigma = 1.4$  MHz. From Figure 5.5, it can be concluded that both the transfer cavity and the recording part of the TCL control system are stable enough on a timescale of  $\sim 1$  h to enable locking with a few MHz stability, which meets our locking objective.

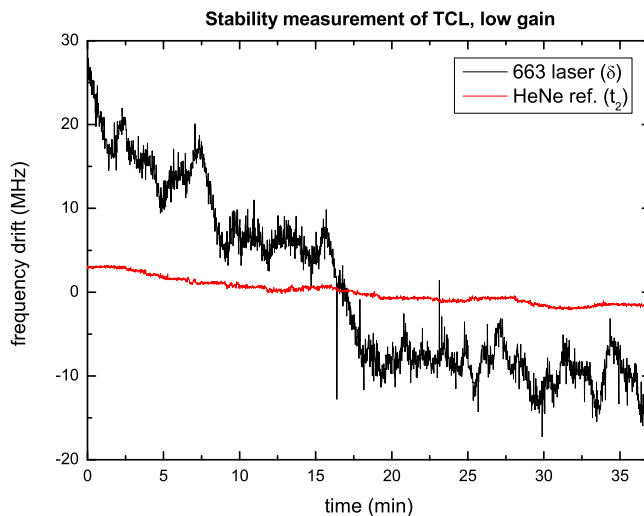


**Figure 5.6:** Frequency drift of the 663 laser locked to the HeNe using the TCL with a lower gain, recorded in the transfer cavity. The red line shows the drift of the reference scan time  $t_2$ .

Next, the same 663 laser was locked using the TCL and again the reference peak distance  $t_2$  and the laser peak position  $\delta$  were recorded. The results are shown in Figure 5.6 and 5.7, using a lower and higher feedback gain, respectively. A more quantitative definition of the gain is explained in Appendix C. The lock shows a much better long term stability for higher gain, while the short term stability is slightly better using lower gain. This reflects one of the issues we experienced implementing the feedback signal. It turned out the feedback signal to the Moglabs box had to be very weak ( $\sim 1$  mV), otherwise the system starts oscillating and the lock is lost. For comparison: the Iodine feedback signal is usually  $\sim 200$  mV. This is probably due to the relatively slow response of the feedback loop: when the laser adjusts the frequency, the next feedback signal is only generated after the piezo of the transfer cavity has completed one scan, which takes currently 20 ms. Meanwhile, the laser is using the 'old' feedback value, and when the gain is large the laser overshoots the locking point and the system starts oscillating. This could be improved by using a faster piezo scan, but this means the resolution of a single scan recorded by the PC gets worse since the PCI card has a maximum sampling rate of 200 kHz. Currently, we are therefore limited by a trade-off between scan resolution

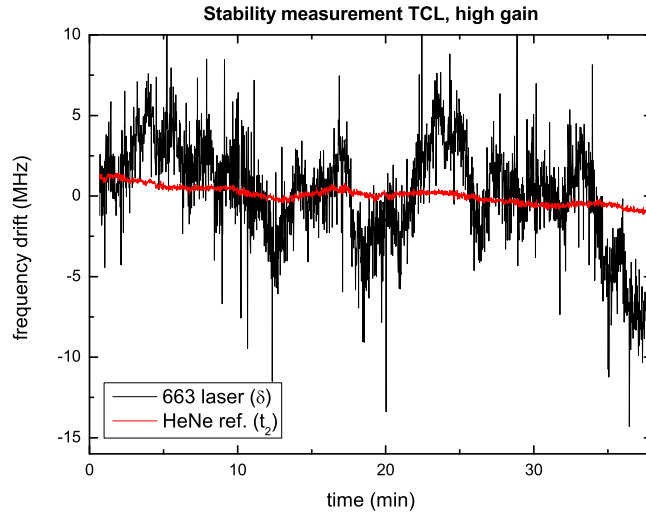


**Figure 5.7:** Frequency drift of the 663 laser locked to the HeNe using the TCL with a higher gain, recorded in the transfer cavity. The red line shows the drift of the reference scan time  $t_2$ .

and speed. The stabilities measured in standard deviations from the figures are listed in Table 5.1. The short term stability of the TCL with higher gain is thus worse because it overshoots locking point. The long term stability is however better for higher gain than for lower gain, probably because for lower gain the feedback signal fed to the laser is very weak and small signals, picked up from neighboring cables or in the electronics, can cause drifts of the lock.

	Iodine lock	TCL, low gain	TCL, high gain
Long term stability	1.71 MHz	10.66 MHz	2.87 MHz
Short term stability	1.41 MHz	0.99 MHz	1.53 MHz

**Table 5.1:** Measured stabilities of the Iodine lock and the TCL. All values are standard deviations of the frequency drifts,  $\leq 1$  s labeled as short term, and  $\leq 35$  min labeled as long term. For the TCL, different measurements were taken using a lower and a higher gain of the feedback signal.

The reference peak distance  $t_2$  shows similar drifts in Figures 5.6 and 5.7 as in the measurement with the Iodine lock. However, the drifts in the 663 laser using the TCL are large compared to the drift of  $t_2$ . This indicates the 663 laser drifts should not originate from the  $t_2$  drift, and the locking stability would therefore currently not be limited by  $t_2$  drifts. However, the two lines in Figure 5.6 show a strong correlation (not very clear in this actual figure due to the scale) and this indicates that in fact the  $\delta$  drift is related to the  $t_2$  drift. Although it probably has to do with irregularities in the scan rate, the precise experimental mechanism responsible for this correlation is not yet clear. Nonetheless, it is clear that the TCL stability on the measured timescales is currently not limited by environmental effects, since these cause at most a  $\delta$

drift of 1.7 MHz, as measured using the Iodine lock. On longer timescales,  $\sim 10$  h, these effect might become more important since slow drift of for instance temperature, can over a long timescale cause significant frequency drifts.

## 5.4 Conclusion

A transfer cavity lock of a 663 nm cooling laser to a HeNe laser was built using a commercially available cavity and a home built control system. As a reference measurement, the system was used to characterize the stability of the 663 laser locked to Iodine absorption peaks. The stability was measured to be 1.71 MHz/h, which confirmed the estimated stability and also shows the data acquisition part of the TCL control system is working properly. Subsequently, the TCL was implemented successfully and stability measurements were done. The stability turned out to depend on the gain, and is 2.87 MHz/30 min using a high gain, with a short term stability of 1.53 MHz/s. These values are very close to the measured stability of the Iodine lock, which proves this method is a promising alternative for the Iodine lock.

One of the limiting factors of the lock is currently the sampling speed of the DAQ card used to record the cavity transmission. Using a card with a higher sampling rate would allow for faster scanning of the piezo. The feedback speed would then increase and most probably a higher gain could be used, increasing the stability of the lock. A second problem are irregularities in the piezo scan, caused by non-linearities or rate variations in the piezo element itself or in the ramp signal. Earlier we experienced similar problems using the PC to generate the ramp signal, and changing to the Thorlabs interferometer controller as ramp source improved the ramp signal a lot. Using an even more stable ramp signal source could therefore possibly solve this issue. Alternatively, the transfer cavity could be replaced by one with a smaller FSR, to decrease the sensitivity of the lock to scanning irregularities. When the TCL is operating for longer times ( $> 2$  h), the resonance peaks used for locking tend to 'walk' out of the scan range due to temperature or pressure changes in the cavity. This can be prevented by manually adjusting the piezo scan offset, but can also be corrected automatically by the control system. The latter needs an external input of the scan offset, which is not provided on the interferometer controller we currently use. We would therefore need a different ramp signal generator with an external input for the scan offset. Improvements on the control system could be made by fitting the detected peaks and determine the zero-crossings more accurately by interpolation. The next step here would be to use a transfer cavity with higher finesse, leading to sharper resonance peaks and a higher resolution. The current system is used to lock one cooling laser, but can be fairly easily expanded to lock multiple lasers fed into the same transfer cavity using the same control system. Finally, small frequency drifts induced by environmental effects such as temperature and pressure can be removed by placing it in a non-evacuated tube and applying a thermal feedback loop.

Currently, the TCL is almost as good as the Iodine lock for timescales  $< 1$  h, and the locking objectives are therefore achieved. Applying a few of the above mentioned modifications can improve the lock stability on both short and long timescales. The transfer cavity lock could then be used to stably lock several cooling lasers using a single control system.

## Chapter 6

# Outlook

In this thesis three experimental projects in molecular physics were carried out, each using one or more optical cavities as main experimental features. For each of the projects, the properties of optical cavities are exploited in a different way.

In the acetylene experiment, it is mainly the large optical path length inside the cavity, providing a long interaction length between the sample molecules and the probing light which results in much better resolved absorption spectra. Precise measurements on the never observed higher overtones of acetylene can lead to a more accurate experimental determination of the vibrational term values. Comparing these values to theory improves our knowledge on the structure and dynamics of not only acetylene, but of molecules in general.

For dipole trapping of cold molecules it is especially the constructive interference inside a cavity which enables a power build up of light, resulting in a sufficient deep trap to capture the molecules. Capturing molecules in a dipole trap opens a new field in molecular physics where precise measurements on ultra-cold molecules can be performed. Not only parity violation can be measured more accurately than before, also for instance dipole-dipole interactions and quantum simulations can be studied when molecules can be loaded in an optical lattice.

In the case of the transfer cavity lock, the narrow cavity resonances for a very broad range of input frequencies provide an accurate measure of the relative input frequencies, allowing for very precise control of the frequency difference. Using this method, it becomes much easier and cheaper to lock multiple lasers to a single frequency reference. Furthermore, locking frequencies are no longer limited to atomic resonances, but the lock can be used for any frequency. These features are very beneficial for the SrF experiment, where several lasers are used which have to be locked at different frequencies.

Since the working principle of every cavity is the same, all cavities obey the same general physical laws described in the Theory chapter. Although exploited differently, in each experiment the operation of a cavity boils down to the same principle: the confinement of light between reflectors. In all three experiments one had to take care of the same effects which recur for every cavity, for instance the mode matching, mirror reflectivities, mirror configuration etc.

It was therefore very useful to work with cavities in different experiments to develop a better understanding of the physics of optical cavities and how this physics can be exploited in a favourable way for a certain application. The three

applications discussed in this thesis are only the tip of the iceberg and optical cavities are not only widely used in the field of molecular physics, but also in other fields, such as atomic physics, quantum physics, solid state physics etc. This leads to the conclusion that the optical cavity is a very powerful method for the manipulation of light, applicable in a wide variety of situations where light is used either as a probe or as system under observation itself.

## Chapter 7

# Acknowledgements

First of all I want to thank Steven for his enthusiastic supervision. I felt very comfortable having a large amount of freedom during my research, but at the same time Steven provided me always with very useful feedback, guiding me through the research process from start to finish. I really appreciate he gave me the possibility to do part of my research in Helsinki.

Many thanks to Markus as well for welcoming me in the physical chemistry group and supervising me on the acetylene project. His help and support with the experiment were indispensable and have meant that I gained a lot of experience in doing experiments and performing measurements.

Also thanks to Hans Beijers for reading my thesis and providing feedback.

From the KVI I would like to thank Oliver, Lorenz and Klaus for the useful discussions and their help on all laser-related matters and Leo and the people from the workshop for their help on technical issues.

Of course thanks to the people from the Cold Molecules group, Steven, Joost, Corine, Sreekanth, Artem and Peter. It was very nice to work with these people, always ready to help me with anything, ranging from vacuum cleaning the lab to reminding me to get my colloquium points. Furthermore, thanks to Keri, Mayerlin, Elwin, Tom, Amita and Nivedya and all other members from the FIS-group and colleagues from the KVI for the nice Moghul food- and game evenings as well as PV-activities, which I enjoyed a lot.

From the University of Helsinki thanks to Markku and Ville for their help and support on the experiments, also to the people from the Physical Chemistry group and Laboratory for Instruction in Swedish, especially Sergio for organizing the great floorball games

My final thanks go to all Finnish and international students I met in Helsinki, especially my roommates from the third floor Markus, Miro, Ondra, Salavat, Diego, Peter and Lars as well as my Finnish speaking friends Adéla, Diane, Fanny, Alice and Lu for making my exchange period an incredible experience.

# Bibliography

- [1] M. Herman, A. Campargue, M. I. El Idrissi, and J. Vander Auwera. Vibrational spectroscopic database on acetylene,  $x1(\sigma_g)+(12c2h2,12c2d2,$  and  $13c2h2)$ . *Journal of Physical and Chemical Reference Data*, 32(3):921–1361, 2003.
- [2] Brian J. Orr. Spectroscopy and energetics of the acetylene molecule: dynamical complexity alongside structural simplicity. *International Reviews in Physical Chemistry*, 25(4):655–718, 2006.
- [3] Mikael Siltanen, Markus Metsala, Markku Vainio, and Lauri Halonen. Experimental observation and analysis of the  $3v1(\sigma_g)$  stretching vibrational state of acetylene using continuous-wave infrared stimulated emission. *The Journal of Chemical Physics*, 139(5):–, 2013.
- [4] C.V. Raman. A new radiation. *Indian J. Phys.*, 2:387–398, 1928.
- [5] Samir Kassi and Alain Campargue. Cavity ring down spectroscopy with  $5e-13$   $cm^{-1}$  sensitivity. *The Journal of Chemical Physics*, 137(23):–, 2012.
- [6] Carter Kittrell, Evan Abramson, James L. Kinsey, Stephen A. McDonald, David E. Reisner, Robert W. Field, and Daniel H. Katayama. Selective vibrational excitation by stimulated emission pumping. *The Journal of Chemical Physics*, 75(5):2056–2059, 1981.
- [7] Markus Metsala, M., Shengfu Yang, Olavi Vaittinen, and Lauri Halonen. Laser-induced dispersed vibration-rotation fluorescence of acetylene: Spectra of ortho and para forms and partial trapping of vibrational energy. *The Journal of Chemical Physics*, 117(19):8686–8693, 2002.
- [8] J. van den Berg. *Ultracold SrF molecules using Stark deceleration and laser cooling*. Phd start essay, University of Groningen, 2011.
- [9] E. S. Shuman, J. F. Barry, D. R. Glenn, and D. DeMille. Radiative force from optical cycling on a diatomic molecule. *Phys. Rev. Lett.*, 103:223001, Nov 2009.
- [10] J.E. van den Berg, S.H. Turkesteen, E.B. Prinsen, and S. Hoekstra. Deceleration and trapping of heavy diatomic molecules using a ring-decelerator. *The European Physical Journal D*, 66(9), 2012.
- [11] J.E. van den Berg, S.C. Mathavan, C. Meinema, J. Nauta, T.H. Nijbroek, K. Jungmann, H.L. Bethlem, and S. Hoekstra. Traveling-wave deceleration of srf molecules. *Journal of Molecular Spectroscopy*, 300(0):22 – 25, 2014.

- [12] C. Meinema. *Laser cooling and Stark deceleration to make ultracold molecules*. Phd startessay, University of Groningen, 2012.
- [13] C. Meinema. Laser cooling of diatomic molecules towards a parity violation measurement. In *Poster, NNV-AMO Lunteren*, 2014.
- [14] S. Hoekman. Exciting cold molecules. Mastersthesi, University of Groningen, 2011.
- [15] Wolfgang Demtroder. *Molecular Physics*. Wiley-VCH, 2003.
- [16] George Cassiday Grant Fowles. *Analytical Mechanics*. Brooks/Cole, 2005.
- [17] Markus Metsälä. *Cavity-enhanced laser spectroscopic studies of vibrational overtones of acetylene*. PhD thesis, University of Helsinki, 2006.
- [18] Gerhard Herzberg. *Molecular Spectra and Molecular molecules I*. D. van Nostrand Company, Inc., 1939.
- [19] Gerhard Herzberg. *Molecular spectra and molecular structure II: Infrared and raman spectra of polyatomic molecules*. D. van Nostrand Company, Inc., 1945.
- [20] Nathalie Picque. *Non-linear Triatomic Molecules*. Springer Berlin Heidelberg, 2012.
- [21] Peter F Bernath. *Spectra of Atoms and Molecules*. Oxford University Press, 2005.
- [22] A. Trenkwalder. Design of a resonator enhanced optical dipole trap for fermionic mixtures. Master’s thesis, University of Innsbruck and Austrian Academy of Sciences, May 2007.
- [23] M.C. Teich B.E.A. Saleh. *Fundamentals of photonics*. John Wiley & Sons, Inc, 2007.
- [24] E. Hecht. *Optics*. Addison Wesley, fourth edition edition, 2002.
- [25] Rudolf Grimm, Matthias Weidemüller, and Yurii B Ovchinnikov. Optical dipole traps for neutral atoms. *Advances in atomic, molecular, and optical physics*, 42:95–170, 2000.
- [26] C. J. Foot. *Atomic Physics*. Oxford University Press, 2005.
- [27] Luciano S. Cruz, Milena Sereno, and Flavio C. Cruz. Deep optical trap for cold alkaline-earth atoms. *Opt. Express*, 16(5):2909–2914, Mar 2008.
- [28] P. D. Edmunds and P. F. Barker. A deep optical cavity trap for atoms and molecules with rapid frequency and intensity modulation. *Review of Scientific Instruments*, 84(8), 2013.
- [29] Kevin K. Lehmann, Giel Berden, and Richard Engeln. *Cavity Ring-Down Spectroscopy: Techniques and Applications*. John Wiley & Sons, Ltd, 2010.
- [30] Martyn D Wheeler, Stuart M Newman, Andrew J Orr-Ewing, and Michael NR Ashfold. Cavity ring-down spectroscopy. *Journal of the Chemical Society, Faraday Transactions*, 94(3):337–351, 1998.

- [31] Markus Metsala, Joseph Guss, Olavi Vaittinen, Raul Z. Martinez, and Lauri Halonen. High repetition rate cavity ringdown spectroscopy of vibrational overtones of  $\text{h}^{13}\text{c}^{13}\text{ch}$  at around  $12200\text{ cm}^{-1}$ . *Chemical Physics Letters*, 424(1-3):7 – 11, 2006.
- [32] F.M. Schmidt, O. Vaittinen, M. Metsala, P. Kraus, and L. Halonen. Direct detection of acetylene in air by continuous wave cavity ring-down spectroscopy. *Applied Physics B*, 101(3):671–682, 2010.
- [33] *HITRAN*. Harvard-Smithsonian Center for Astrophysics (CFA), Cambridge, MA, USA V.E. Zuev Institute of Atmospheric Optics (IAO), Tomsk, Russia, <http://hitran.iao.ru/survey>, 2014.
- [34] J. Vanderauwera, D. Hurtmans, M. Carleer, and M. Herman. The  $\nu_3$  fundamental in  $\{\text{C}_2\text{H}_2\}$ . *Journal of Molecular Spectroscopy*, 157(2):337 – 357, 1993.
- [35] J. F. Barry, D. J. McCarron, E. B. Norrgard, M. H. Steinecker, and D. DeMille. Magneto-optical trapping of a diatomic molecule. *Nature*, 512:286–289, 2014.
- [36] S. Hoekstra. Engineering quantum materials with ultracold polar molecules. In *VIDI Grant proposal*, 2011.
- [37] Stephen L. Davis. Model polarizabilities and multipoles for ionic compounds. alkaline-earth monohalides. *The Journal of Chemical Physics*, 89(3):1656–1663, 1988.
- [38] A. Mosk, S. Jochim, H. Moritz, T. Elsässer, M. Weidemüller, and R. Grimm. Resonator-enhanced optical dipole trap for fermionic lithium atoms. *Optics Letters*, 26:1837–1839, December 2001.
- [39] M. E. Gehm, K. M. O’Hara, T. A. Savard, and J. E. Thomas. Dynamics of noise-induced heating in atom traps. *Phys. Rev. A*, 58:3914–3921, Nov 1998.
- [40] Seung Koo Lee, Hyun Sook Lee, Jang Myun Kim, and D Cho. Optical dipole trap using a fabry-perot interferometer as a power buildup cavity. *Journal of Physics B: Atomic, Molecular and Optical Physics*, 38(8):1381, 2005.
- [41] D. Kruse, M. Ruder, J. Benhelm, C. von Cube, C. Zimmermann, Ph. W. Courteille, Th. Elsässer, B. Nagorny, and A. Hemmerich. Cold atoms in a high-q ring cavity. *Phys. Rev. A*, 67:051802, May 2003.
- [42] P Munstermann, T Fischer, P.W.H Pinkse, and G Rempe. Single slow atoms from an atomic fountain observed in a high-finesse optical cavity. *Optics Communications*, 159(1-3):63 – 67, 1999.
- [43] T.W. Hansch and B. Couillaud. Laser frequency stabilization by polarization spectroscopy of a reflecting reference cavity. *Optics Communications*, 35(3):441 – 444, 1980.
- [44] M. Nickerson. A review of pound-drever-hall laser frequency locking. JILA, University of Colorado and NIST.

- [45] Eric D. Black. An introduction to pound-drever-hall laser frequency stabilization. *American Journal of Physics*, 69(1):79–87, 2001.
- [46] B. Neyenhuis, B. Yan, S. A. Moses, J. P. Covey, A. Chotia, A. Petrov, S. Kotochigova, J. Ye, and D. S. Jin. Anisotropic polarizability of ultracold polar  $^{40}\text{K}^{87}\text{Rb}$  molecules. *Phys. Rev. Lett.*, 109:230403, Dec 2012.
- [47] Howard P. Layer. Acoustooptic modulator intensity servo. *Appl. Opt.*, 18(17):2947–2949, Sep 1979.
- [48] JDSU. Suppression of stimulated brillouin scattering. Technical report, JDS Uniphase Corporation, 2006.
- [49] Christof Weitenberg. *Single-Atom Resolved Imaging and Manipulation in an Atomic Mott Insulator*. PhD thesis, Ludwig-Maximilians-Universitat Munchen, 2011.
- [50] D. Rio Fernandes, F. Sievers, N. Kretzschmar, S. Wu, C. Salomon, and F. Chevy. Sub-doppler laser cooling of fermionic 40 k atoms in three-dimensional gray optical molasses. *EPL (Europhysics Letters)*, 100(6):63001, 2012.
- [51] M. Weidemuller, T. Esslinger, M. A. Ol’shanii, A. Hemmerich, and T. W. Hansch. A novel scheme for efficient cooling below the photon recoil limit. *EPL (Europhysics Letters)*, 27(2):109, 1994.
- [52] M. S. Shahriar, P. R. Hemmer, M. G. Prentiss, P. Marte, J. Mervis, D. P. Katz, N. P. Bigelow, and T. Cai. Continuous polarization-gradient precooling-assisted velocity-selective coherent population trapping. *Phys. Rev. A*, 48:R4035–R4038, Dec 1993.
- [53] D. Boiron, A. Michaud, P. Lemonde, Y. Castin, C. Salomon, S. Weyers, K. Szymaniec, L. Cognet, and A. Clairon. Laser cooling of cesium atoms in gray optical molasses down to 1.1  $\mu\text{k}$ . *Phys. Rev. A*, 53:R3734–R3737, Jun 1996.
- [54] Peter Drolenga. Optical pumping of high-field to low-field seeking states of srf. Master’s thesis, University of Groningen, 2014.
- [55] G. Salomon, L. Fouché, P. Wang, A. Aspect, P. Bouyer, and T. Bourdel. Gray molasses cooling of  $^{39}\text{K}$  to a high phase-space density. *ArXiv e-prints*, October 2013.
- [56] C. Triche, P. Verkerk, and G. Grynberg. Blue-sisyphus cooling in cesium gray molasses and antidot lattices. *The European Physical Journal D - Atomic, Molecular, Optical and Plasma Physics*, 5(2):225–228, 1999.
- [57] Martin Zeppenfeld, Barbara G. U. Englert, Rosa Glockner, Alexander Prehn, Manuel Mielenz, Christian Sommer, Laurens D. van Buuren, Michael Motsch, and Gerhard Rempe. Sisyphus cooling of electrically trapped polyatomic molecules. *Nature*, 491(7425):570–573, November 2012.

- [58] B. G. U. Englert, M. Mielenz, C. Sommer, J. Bayerl, M. Motsch, P. W. H. Pinkse, G. Rempe, and M. Zeppenfeld. Storage and adiabatic cooling of polar molecules in a microstructured trap. *Phys. Rev. Lett.*, 107:263003, Dec 2011.
- [59] J. J. Thorn, E. A. Schoene, T. Li, and D. A. Steck. Experimental Realization of an Optical One-Way Barrier for Neutral Atoms. *Physical Review Letters*, 100(24):240407, June 2008.
- [60] C. Y. Yang, P. Halder, O. Appel, D. Hansen, and A. Hemmerich. Continuous loading of S01 calcium atoms into an optical dipole trap. *Phys. Rev. A*, 76(3):033418, September 2007.
- [61] Mathew S. Hamilton, Anthony R. Gorges, and Jacob L. Roberts. Influence of optical molasses in loading a shallow optical trap. *Phys. Rev. A*, 79:013418, Jan 2009.
- [62] Eric R. Hudson, Nathan B. Gilfoy, S. Kotochigova, Jeremy M. Sage, and D. DeMille. Inelastic collisions of ultracold heteronuclear molecules in an optical trap. *Phys. Rev. Lett.*, 100:203201, May 2008.
- [63] S. Kotochigova and E. Tiesinga. Controlling polar molecules in optical lattices. *Phys. Rev. A*, 73:041405, Apr 2006.
- [64] P F Griffin, K J Weatherill, S G MacLeod, R M Potvliege, and C S Adams. Spatially selective loading of an optical lattice by light-shift engineering using an auxiliary laser field. *New Journal of Physics*, 8(1):11, 2006.
- [65] W.M. Haynes, editor. *CRC Handbook of Chemistry and Physics, 95th Edition*. CRC Press, 2014.
- [66] John H. T. Burke, Ofir Garcia, K. Jeramy Hughes, Brian Livedalen, and Charles A. Sackett. Compact implementation of a scanning transfer cavity lock. *Review of Scientific Instruments*, 76(11):-, 2005.
- [67] J. F. Barry. *Laser cooling and slowing of a diatomic molecule*. Phdthesis, Yale University, 2013.
- [68] Paul Hamilton, Matt Jaffe, Justin Brown, Lothar Maisenbacher, Brian Estey, and Holger Muller. Atom interferometry in an optical cavity. In *CLEO: 2014 Postdeadline Paper Digest*, page FTh5A.1. Optical Society of America, 2014.
- [69] S. Uetake, K. Matsubara, H. Ito, K. Hayasaka, and M. Hosokawa. Frequency stability measurement of a transfer-cavity-stabilized diode laser by using an optical frequency comb. *Applied Physics B*, 97(2):413–419, 2009.
- [70] A. Rossi, V. Biancalana, B. Mai, and L. Tomassetti. Long-term drift laser frequency stabilization using purely optical reference. *Review of Scientific Instruments*, 73(7):2544–2548, 2002.

# Appendices

## Appendix A

# Details of the acetylene experimental setup

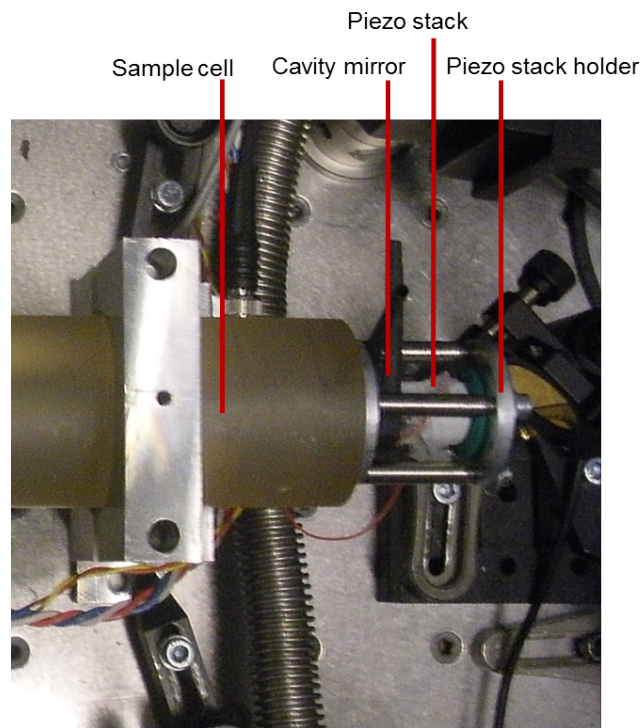


**Figure A.1:** *Picture showing mounting of the back mirror of the optical cavity and the piezo stack on the Zerodur glass cell.*

## Appendix B

# Additional data on acetylene

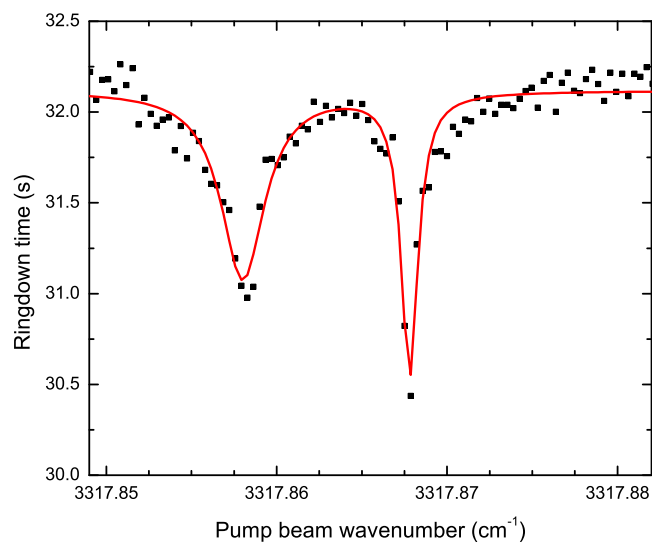


**Figure B.1:** Acetylene spectrum obtained by scanning the pump beam, with probe beam frequency  $6392.394\text{ cm}^{-1}$ . The red curve is the sum of two Lorentzians fitted to the two peaks, centered at  $3317.8580$  and  $3317.8678\text{ cm}^{-1}$ .

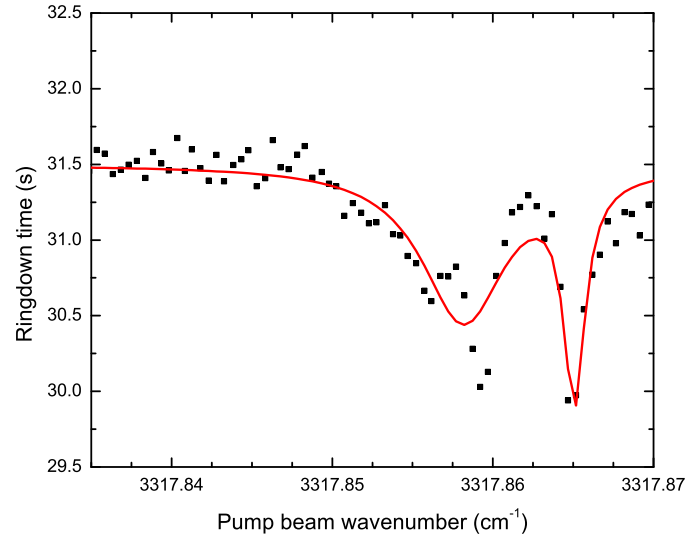


**Figure B.2:** Acetylene spectrum obtained by scanning the pump beam, with probe beam frequency  $6392.397\text{ cm}^{-1}$ . The red curve is the sum of two Lorentzians fitted to the two peaks, centered at  $3317.8582$  and  $3317.8651\text{ cm}^{-1}$

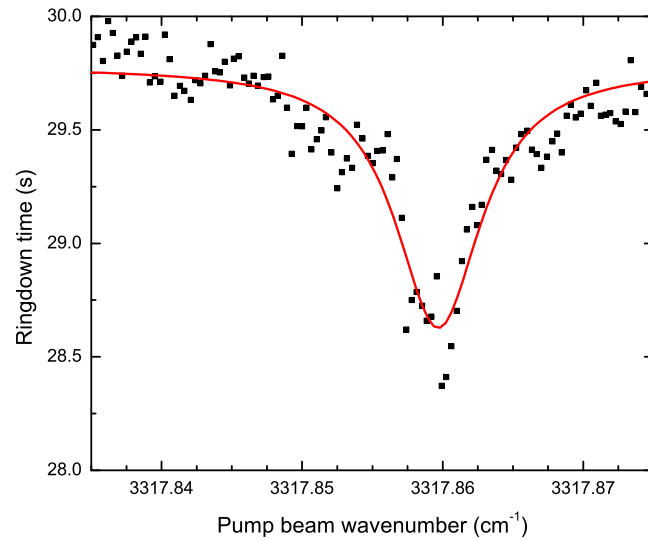


**Figure B.3:** Acetylene spectrum obtained by scanning the pump beam, with probe beam frequency  $6392.400\text{ cm}^{-1}$ . The red curve a Lorentzian fit of the peak, centered at  $3317.8597\text{ cm}^{-1}$ .

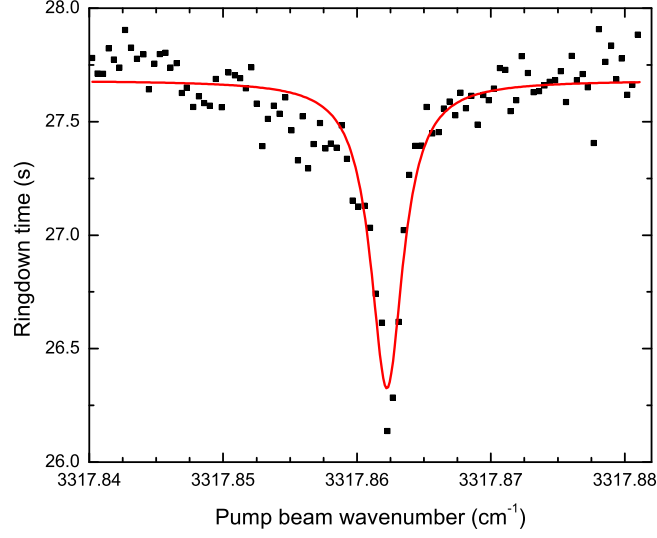


**Figure B.4:** Acetylene spectrum obtained by scanning the pump beam, with probe beam frequency  $6392.403 \text{ cm}^{-1}$ . The red curve a Lorentzian fit of the peak, centered at  $3317.8622 \text{ cm}^{-1}$ .

Figure	3.9	B.1	B.2	B.3	B.4
ECDL wavenumber cm	6392.392	6392.394	6392.397	6392.4	6392.403
ECDL offset	0.011	0.009	0.006	0.003	0
Left peak center	3317.8552	3317.8580	3317.8582	3317.8597	3317.8622
Left peak width	0.00235	0.0031	0.00641	0.00742	0.00294
Right peak center	3317.8666	3317.8678	3317.8651	-	-
Right peak width	0.00128	0.00119	0.00157	-	-
Peak difference	0.01138	0.00979	0.00689	-	-
Center	3317.86088	3317.862905	3317.861625	3317.8597	3317.8622
Averaged center	3317.8615	3317.8615	3317.8615	3317.8615	3317.8615
Offset from averaged center resonance	-0.0006	0.0014	0.0002	-0.0018	0.0008
$0.52\Delta\omega_{probe}$	0.00572	0.00468	0.00312	0.00156	0
Half of peak difference	0.00569	0.004895	0.003445	-	-

**Table B.1:** Parameters extracted from the Lorentzian fits of the absorption spectra of  $C_2H_2$ , all values are in  $\text{cm}^{-1}$ .

## Appendix C

# Details of the transfer cavity lock

### C.1 Gain of laser feedback signal

As explained in section 5.3, the feedback signal fed to the laser controller had to be very weak, otherwise the lock was lost very quickly. However, sending a small signal through a long cable makes the output very sensitive to perturbations from the environment, for instance from other cables. Therefore we used a voltage divider to scale down the voltage divider at the input of the laser controller. The feedback signal is now evolving as follows. The Labview program calculates the feedback signal  $\Omega$  by subtracting  $\delta$  from the set-point  $\Delta_{set}$ :  $\Omega = \Delta_{set} - \delta$ . The resulting  $\Omega$  is multiplied by the gain set on the Labview interface. For the low gain specified in section 5.3 this is 50, and for high gain this is 80. The resulting number is converted into a voltage with a range of 0 – 10 V by the digital output card. The signal is then taken to the laser controller by a  $\sim 10$  m long cable, and just before the laser control box scaled down by the voltage divider by a factor of 650, resulting in a  $\sim$  mV signal entering the laser controller. On the laser controller, the gain and offset of the internal feedback signal can be controlled. The gain is increased to a value just below the point where the laser starts oscillating. The internal error signal has then a magnitude of  $\sim 5$ -10 mV.

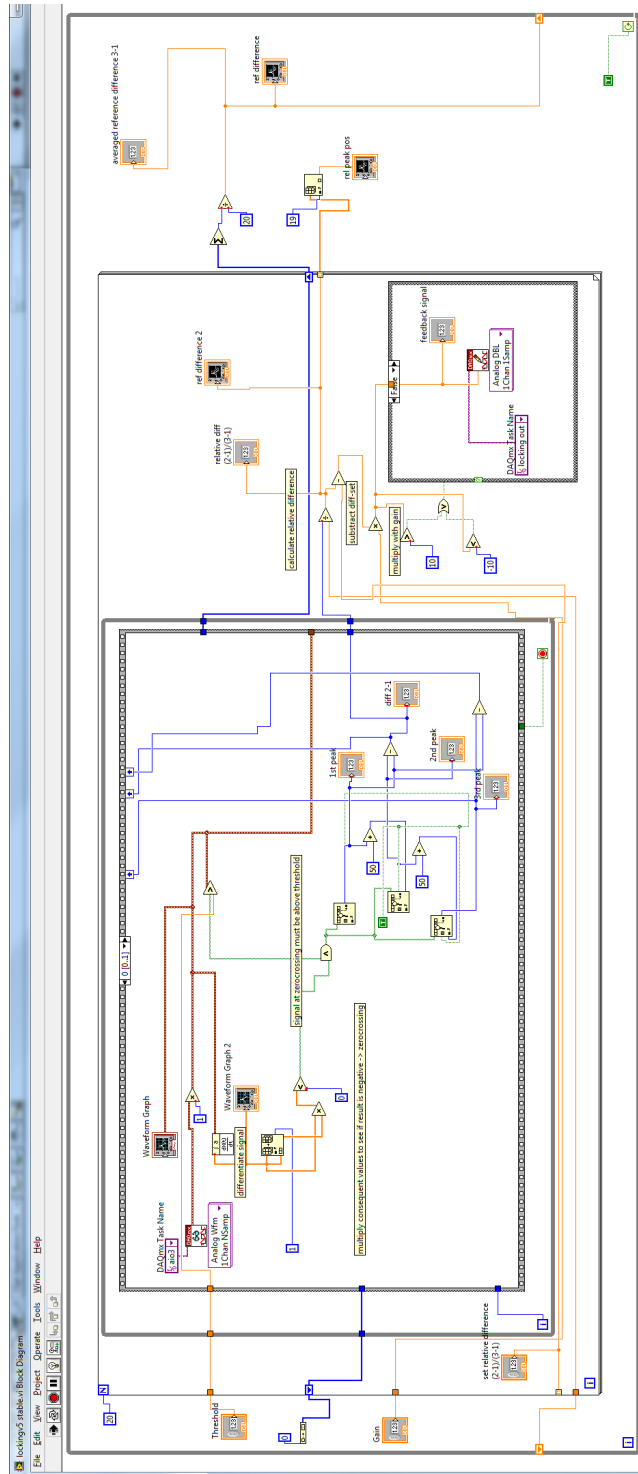


**Figure C.1:** Block diagram of the Labview program used to generate the feedback signal for the transfer cavity lock.